Towards a Quantum Entanglement Enhanced Atom Interferomter

by

Vyacheslav Li

July, 2024

A thesis submitted to the
Graduate School
of the
Institute of Science and Technology Austria
in partial fulfillment of the requirements
for the degree of
Doctor of Philosophy

Committee in charge:

Mattew Kwan, Chair
Onur Hosten
Johannes Fink
Jason Hogan

The thesis of Vyacheslav Li, titled *Towards a Quantum Entanglement Enhanced Atom Interferomter*, is approved by:

Supervisor: Onur Hosten, ISTA, Klosterneuburg, Austria

Signature: _____

Committee Member: Johannes Fink, ISTA, Klosterneuburg, Austria

Signature: _____

Committee Member: Jason Hogan, Stanford University, Stanford, California

Signature: _____

Defense Chair: Mattew Kwan, ISTA, Klosterneuburg, Austria

Signature: _____

Signed page is on file

ISTA Thesis, ISSN: 2663-337X

I hereby declare that this thesis is my own work and that it does not contain other people's work without this being so stated; this thesis does not contain my previous work without this being stated, and the bibliography contains all the literature that I used in writing the dissertation.

I declare that this is a true copy of my thesis, including any final revisions, as approved by my thesis committee, and that this thesis has not been submitted for a higher degree to any other university or institution.

I certify that any republication of materials presented in this thesis has been approved by the relevant publishers and co-authors.

Signature: _____

Vyacheslav Li
July, 2024

Signed page is on file

Abstract

This thesis describes the development of an atom interferometer designed to exploit the advantages of utilizing quantum entanglement for enhanced precision measurements beyond the standard quantum limit. While the project remains ongoing, significant progress has been made.

A key contribution of this work is the development of Quantrol, an experimental control system leveraging the ARTIQ framework. This software enables precise timing and control without requiring prior knowledge of ARTIQ's implementation details or coding experience. The interface offers user friendly visual comprehension of the experimental sequence and extended capabilities, allowing researchers to scan variables with a simple click of a mouse.

The main proposed project is to implement atom interferometric sequence with squeezed input states inside of a dipole trap generated by a high finesse cavity. The presence of the dipole trap allows one dimensional atomic cloud split while maintaining relatively strong confinement in other directions.

We are currently able to trap and cool ^{87}Rb atoms to few micro kelvin temperatures, load them into the dipole trap and state prepare them to be used for squeezing and interferometric sequence.

Acknowledgements

First of all, I want to thank my supervisor, Onur Hosten, for entrusting me to be his first PhD student. I always tried, and I hope that I did meet his expectations. From my side, I am endlessly grateful that I had a privilege of working together with Onur in the lab, even for multiple weeks. The time when we both stayed on campus and couple of times was walking to our apartments after midnight will always be one of the warmest and invaluable memories for me. Throughout nearly six years of working with Onur, I have adopted from him not only professional skills such as creative problem solving, the ability to learn quickly, and explaining complex concepts, but also human values like humbleness, honesty, and kindness.

Thanks to Onur's investment of personal time, especially early in my PhD journey, I developed skills that made me successful not only in the lab, but also highly valued in the job market. Beyond the technical expertise, our weekly group meetings and discussions fostered my communication skills. After multiple interviews with various corporations, I now possess a valuable skill set, thanks to my group mates and Onur.

A huge thank you to our team members, who shouldered the burden of building such a complex experimental setup together. My very first Postdoc, Fritz Diorico, for his experience in working with optical components, especially AOMs and fiber coupling tips and tricks. It was a pity that you have been focused on the squash locking technology, as we might have benefited more from you as a team. However, that allowed for me and my colleague Sebastian Wald to learn on taking the responsibility, and become more independent. Sebastian Wald, for your invaluable dedication in aligning the lasers to optical resonators, your endless motivation to achieve things faster and eagerness to help with anything in the lab and out of it. I am endlessly grateful that you took over the vacuum baking procedures while I was focusing on the Quantrol development. My PhD journey would have been way harder without a buddy like you. Special thanks to Edward Gheorghita for helping out with tedious 3D MOT alignment procedures. It would have been much harder without the second pair of hands and eyes. You helped me to practise my teaching and supervision skills as well. I believe that you also gained a lot from our mutual work. Umang Mishra, for helping me to appreciate the quality and complexity of the Quantrol control system. It was important to hear a positive comments from a person with a computer science background. Finally, Sofia Agafonova and all Hosten group members, thank you for sharing the office space, attending weekly discussions, and interacting here and there. I will miss the lunch breaks with all of you.

I would also like to thank my examination committee, Onur Hosten, Johannes Fink, Jason Hogan, ..., for their time. I am also grateful to Fritz Diorico for proofreading my thesis, and Edward Gheorghita's comments that greatly helped to improve the contents of my thesis.

I would also like to thank my parents for investing everything into me. Being raised in the family of a person who had to become a farmer despite early academic success in Mechanical Engineering, I feel privileged to have the possibility to do this PhD and choose my future career

path. I know that you are proud of me and I want you to know that I owe my very existence to you. I have left the house very early to pursue better knowledge and life conditions, but I always carry you deep in my heart.

I am proud of being able to have two children during this wonderful PhD journey. It would have been impossible without my wife Nazgul's absolute sacrifice. Having a master degree in nuclear physics, and a nice career prospective she decided to leave everything behind, follow me to Austria, and stay at home with children for six years. This PhD would not have been possible without your support and positive attitude.

In the end, I would like to thank the European Research Council under grant agreement no. 101087907 for funding this research.

About the Author

Vyacheslav Li completed a BSc in Physics at the Nazarbayev University, Kazakhstan, where he worked on Brillouin scattering used in remote characterization of elastic properties of materials. He joined ISTA in Sebtember 2018. His main research interests include quantum optics, quantum physics, atom interferometry and precision measurements. In April 2019, he affiliated with Onur Hosten's group as a first PhD student where he was involved in the building components required for experimental setup. During his PhD studies, Vyacheslav implemented various analog feedback control systems, worked on arrangement and alignment of optical elements for light preparation, automated data acquisition and analysis, and developed Quantrol, experimental control system for precise timing and control, that allows desing and implementation of complex experiments with a user friendly interface and without coding experience.

List of Collaborators and Publications

1. Vyacheslav Li, Fritz Diorico, and Onur Hosten. Laser frequency-offset locking at 10-hz-level instability using hybrid electronic filters. *Phys. Rev. Appl.*, 17:054031, May 2022

2. Umang Mishra, Vyacheslav Li, Sebastian Wald, Sofia Agafonova, Fritz Diorico, and Onur Hosten. Monitoring and active stabilization of laser injection locking using beam ellipticity. *Opt. Lett.*, 48(15):3973–3976, Aug 2023

Table of Contents

List of Figures

List of Tables

List of Abbreviations

AOM acousto-optic modulator. 27, 31, 36, 64

ARTIQ Advanced Real-Time Insfrastructure for Quantum physics. vii, xiii, xiv, 55–58, 69

CPU central processing unit. 56, 57, 64

CSS coherent spin state. xiv, 5, 7

DDS direct digital synthesizer. xvi, xviii, xix, 32, 46, 48, 58, 59, 62, 64

DDSs direct digital synthesizers. 56

DFB distributed feedback. 27, 33

ECDLs external cavity diode lasers. 27, 46

EDFA erbium-doped fiber amplifier. 33

EOM electro-optic modulators. 45

FD frequency discriminator. xviii, 46–50

FIFO first-in-first-out. 56, 57

FPGA field-programmable gate array. 56–58, 64

FPGAs field-programmable gate arrays. 55

GUI graphical user interface. 58, 59

LO local oscillator. xiv, xviii, 7, 46–48, 50

MEM micro-electromechanical. 36

MOT magneto optical trap. xiii–xx, 15, 17–19, 21–26, 28, 31, 32, 36–39, 41–43, 51–54, 56, 59, 65–68, 72

OAT one axis twisting. xiv, 6, 7, 13

OPLL optical phase locked loop. 46

PBS Polarizing Beam Splitter. xvii, 36, 38

PCB printed circuit board. 24, 49

PD photodetector. xviii, 29, 33, 36, 48

QED quantum electrodynamics. 5

QND quantum nondemolition. xiv, 6, 7, 13

QPD quadrant photodetector. 35

RF radio frequency. xvi, xix, 4, 19, 32, 50, 65, 66

SDK state dependent kick. 4, 5

SQL standard quantum limit. 1, 2, 5, 7

SSB single sideband modulator. xvi, 33, 35

SSS spin squeezed state. xiv, 5–7

TOF time of flight. xvii, 44

UHV ultra high vacuum. 15

CHAPTER 1

Introduction

The scientific approach of understanding the world and its working principles is based on making valid approximations. We simplify a rather complex world down to a model and come up with a theory that can explain our observations. After that we conduct experiments to either support theory or find instances where it fails. In the latter case we come up with modified theories to cover the phenomenon where it previously failed. This is an iterative way of extending our understanding of the physical world we are living in. The more we progress, the more we converge to the real model of the world. Hence, in order to further improve existing theories one needs to observe phenomena that doesn't fit into the current theory. This is only possible with the advance of technologies and higher measurements precision. In this convergence process we inevitably have reached the point when we need to take into account the quantum nature of the world. Unlike the deterministic classical world, quantum mechanics has inherently probabilistic nature that requires a different measurement treatment.

Measuring an unknown parameter with a quantum system is typically done by preparing the probe, letting it interact with the system of interest, and then measuring the probe. Knowing the physical mechanism that governs the dynamics of the latter interactions, one can infer the information about the parameter of interest. There is additional quantum noise in quantum measurements that arises from the impossibility of simultaneously measuring conjugate physical observables. The product of the uncertainties for conjugate observables is known to have a lower bound that is called the Heisenberg limit. For example, conjugate coordinates of angular momentum projections:

$$\Delta J_z \cdot \Delta J_y \geq \left| \frac{J_x}{2} \right|.$$

The physical description of an atom interferometer can be efficiently mapped onto angular momentum operators. For an atom interferometer operated with N uncorrelated atoms, the uncertainty of two angular momentum projections are equal and hence quantum projection noise that limits phase measurements scales as $\propto \frac{1}{\sqrt{N}}$. This limit is known as the standard quantum limit (SQL) of phase measurements. Making use of quantum correlations in an atom interferometer the noise can be redistributed between two conjugate projections decreasing the uncertainty in one of them at the expense of increasing it in another. In principle, quantum enhanced atom interferometer phase measurement uncertainty can be mitigated down to fundamental limit that scales as $\propto \frac{1}{N}$. Taking into account that the number of atoms in atom interferometers ranges between 10^4 - 10^7 the potential enhancement is significant.

However, in order to make use of quantum entanglement in atom interferometers there are still many challenges that need to be overcome such as effective mapping of correlations from internal degrees of freedom into momentum space, preserving coherence, and squeezing during the spatial interference sequence, preserving large number of atoms and sufficient interrogation times. In fact, the very act of manipulating state introduces additional noises due to imperfections. Some experimental progress towards overcoming these challenges have been reported very recently in reference [AIF+20], where the mapping of internal degrees prepared in non-classical states (twin-fock states) to spatial degrees of freedom is demonstrated.

The primary objective of this Ph.D. thesis is to build the experimental setup that would allow utilizing quantum entanglement in atom interferometry to push the limits of precision metrology. Higher precision in atom interferometers will not only advance the fundamental research such as testing Einstein equivalence principle, [GAS+10] and have applications in geodesy [WPM+19] but also will open new ground to investigate larger quantum superpositions as interfering atomic clouds approach macroscopic scales.

In the following pages, we introduce the basic concepts of atom interferometry, quantum entanglement, and analog feedback control systems. Following this, different parts of the experimental setup will be described in details. Subsequent sections will describe the implementation details that helped make everything work. Then the experimental control will be described with the explanation of Quantrol system that we developed. In the end, the experimental sequence and system characteristics will be described, followed by the summary and future plans.

At the time of writing, there have been two published demonstrations of squeezing enhanced atom interferometry: [GLWea22] and [MWMRK22]. These are very recent developments, and both of these results show approximately 1 dB of enhancement beyond SQL. While these works show the possibility of the endeavor, achieving more useful levels of squeezing is still on the horizon. The work described in this thesis is an engineered attempt to achieve this goal.

CHAPTER 2

Background knowledge

This chapter will cover the basic concepts of atom interferometry, quantum entanglement and analog feedback systems to build a foundation to follow the rest of the thesis.

2.1 Atom interferometry

Advances in quantum mechanics in the beginning of 1920s inspired by Louis de Broglie [dB25] underpinned the possibility of matter to display wave-like properties and hence have the same type of interference phenomena as light. Since then matter-wave interference has been demonstrated for a variety of systems including electrons [Li80], neutrons [DDK$^+$20], atoms, [SgoAD96] and even biomolecules [HUH$^+$03].

The working principle of atom interferometers resembles a Mach-Zechnder interferometer shown in figure 2.1. A matter-wave is coherently split into two paths depending on external (motional) or internal (spin) states of the atoms, and propagated through different paths. During the so called interrogation time T_R two paths acquire relative phase shift ϕ that carries information about the parameter of interest due to induced interactions in one or both interferometer arms. In particular, optical phase measurements in atom interferometers can be used to infer information about distance, acceleration, rotation, and many other physical quantities. After T_R beams are recombined to obtain interference pattern that is usually a population difference as a function of ϕ.

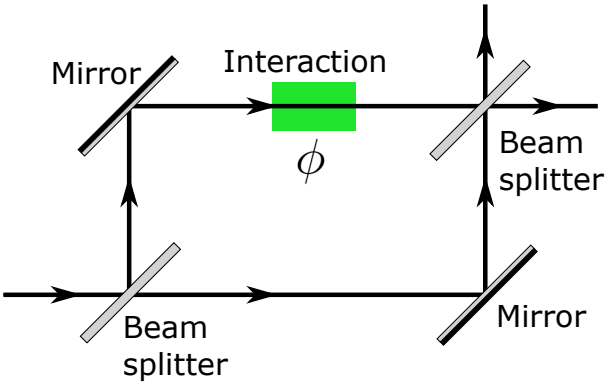

Figure 2.1: Schematic drawing of Mach-Zechnder type interferometer.

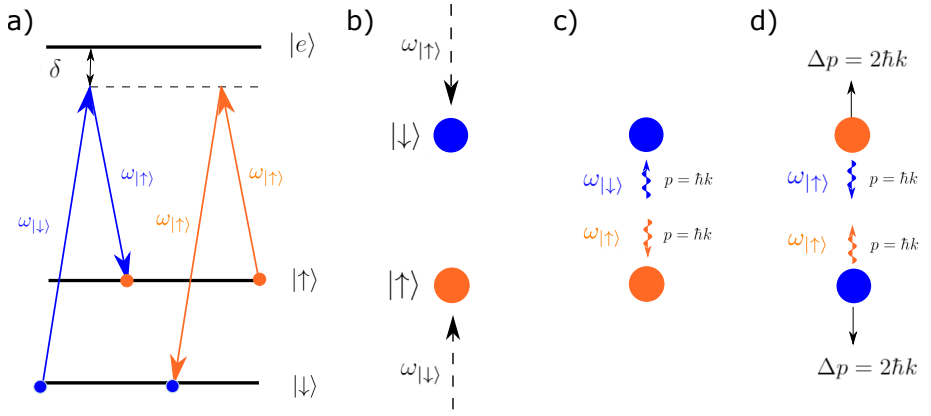

Figure 2.2: (a) Energy level diagram showing the frequencies of counter-propagating laser beams and state evolution of $|\downarrow\rangle$ (blue arrows) and ($|\uparrow\rangle$) (orange arrows). (b) Black dashed lines are two counter-propagating laser beams. Atom in $|\downarrow\rangle$ ($|\uparrow\rangle$) absorbs a photon (c) from laser with frequency $\omega_{|\downarrow\rangle}(\omega_{|\uparrow\rangle})$ acquiring one photon momentum and then instantly emits a photon (d) with frequency $\omega_{|\uparrow\rangle}(\omega_{|\downarrow\rangle})$ in the direction opposite to its momentum due to stimulated emission. In the end of the process atom changes its state to $|\uparrow\rangle(|\downarrow\rangle)$ state and acquires a momentum $\Delta p = 2\hbar k$, where k is an average wave vector of the photon in two beams.

Atom interferometry has proven to be an exceptionally effective tool in precision measurements over the last couple of decades. The variety of applications ranges from inertial sensing with accelerometers [GMS+11] and gyroscopes [GBK97] to measurements of gravitational tides [PCC03], and gravity gradients [SMB+98]. Apart from practical applications it is widely used in fundamental research such as measuring of gravitational constant [RSC+14], and putting bounds on theories of dark matter [HJH+15]. Perhaps one of the well-known applications of atom interferometry, albeit with only internal state interference without physical path separations, is in the field of time keeping, implementing atomic clocks. The method developed by Ramsey, which enabled the precise measurement of atomic transition frequencies with high accuracy, is now used in the very definition of time. Furthermore, the developments of atom interferometers spawned industrial quantum sensing applications that resulted in establishing companies such as Exail, ColdQuanta, VectorAtomics, AOsence, and many others.

2.1.1 State dependent kick

In atom interferometers the beam splitter and mirror reflection of matter-waves is usually done by applying Raman pulses that couple states $|\uparrow\rangle$ and $|\downarrow\rangle$ by a two-photon transition with a detuning δ from excited state $|e\rangle$ [JXH+18]. Coupling is done by applying two counter-propagating laser pulses with frequencies $\omega_{|\uparrow\rangle}$ and $\omega_{|\downarrow\rangle}$. The mechanism is described in figure 2.2. Depending on the state of the atom it absorbs a photon from one laser and due to stimulated emission instantly emits a photon identical to a photon coming from another laser. In this way atoms acquire state dependent kick (SDK) in the opposite directions. Assuming that the momentum of photons from both lasers are same, the resulting change in momentum of each atom is $\Delta p = 2\hbar k$. Direction of the SDK can be either changed by swapping the states by applying RF π pulse or by interchanging the frequencies of the lasers.

In case of the moving atoms one needs to account for the Doppler shift of the frequency seen by different atoms. Since atoms always have some thermal velocity distribution Raman

pulses can be made short to effectively increase frequency bandwidth of the pulse. Also one should compensate the AC-Stark shift induced by Raman pulses. This can be done by tuning intensities of two Raman beams. We are going to implement cavity squeezing of canonical hyperfine clock transition of ^{87}Rb atoms so that the $|\uparrow\rangle$ and $|\downarrow\rangle$ states of pseudo-spin $1/2$ system are $|F = 2, m_F = 0\rangle$ and $|F = 1, m_F = 0\rangle$ respectively. Then, the goal is to map these internal states onto motional degrees of freedom, and then back, by utilizing the SDKs to form a squeezed atom interferometer.

2.2 Quantum entanglement

A defining property of quantum mechanics is the ability of the measurement to project the system into particular state. If an atom in an equal superposition of spin$|\uparrow\rangle$ and $|\downarrow\rangle$ is being measured in the eigen basis, the state of the atom projects to either of states and remains in that state. Thereby, the measurement destroys the superposition state by giving information about the state of the atom. However, measurement performed on an ensemble can project it into entangled state such that the state of each particle depends on the states of all other particles in the ensemble.

Let us now put it in the context of cavity quantum electrodynamics (QED). An ensemble of N two-level atoms can be conveniently described with pseudo-spin $N/2$ language. In this language z component of the spin J represents population difference ($2J_z = \Delta n$) and orientation in J_y-J_x plane represents the phase difference between two states. If the ensemble is prepared in a coherent spin state (CSS) that is oriented along x-axis then $\langle J_z\rangle = \langle J_y\rangle = 0$, and $\langle J_x\rangle = N/2$ [ACGT72]. Since components of angular momentum do not commute, uncertainties in population difference and phase need to satisfy uncertainty relation $\Delta J_z \cdot \Delta J_y \geq N/4$. For an unentangled ensemble $\Delta J_z = \Delta J_y = \sqrt{N}/2$ that is pictorially represented as a circle in figure 2.4(a).

By introducing quantum entanglement between the atoms one can reduce quantum fluctuations below SQL in one of the projections [KU93]. This process is called spin squeezing as the uncertainty is literally getting squeezed in one direction as shown in figure 2.4(b). After generating spin squeezed state (SSS) the axis that is less noisy can be used to perform measurements with enhanced precision. In the following section we will first give a description of the light matter interaction in the cavity, simplified with some assumptions relevant to our experiment, to found the basis for the following sections describing generation of squeezing.

2.2.1 Generating spin-squeezed states

Following paragraphs closely follow the description of the cavity based squeezing described in [SSLVac10]. Consider an ensemble of N identical three level atoms with two ground states $|\uparrow\rangle$, $|\downarrow\rangle$ (e.g. hyperfine states) that are split by an energy $\hbar\omega_a$ and coupled via optical transitions with frequencies $\omega_c \pm \omega_a/2$ to an excited state $|e\rangle$ with population decay rate Γ. We assume that the cavity resonance with linewidth κ is tuned halfway between the ground states and excited state resulting in equal and opposite sign detunings $\Delta_{|\uparrow\rangle} = -\Delta_{|\downarrow\rangle} = \omega_a/2$ (see figure 2.3(a)). Also we assume that both transitions have the same strength and all atoms are equally coupled to resonator with single-photon Rabi frequency $2g$. In case of large detuning $\Delta \gg \kappa, \Gamma, g$ and sufficiently low intra-cavity photon number $\langle a^\dagger a\rangle \ll (\Delta/g)^2$ we can adiabatically eliminate the excited state resulting in an effective Hamiltonian for the dynamics of the two ground states:

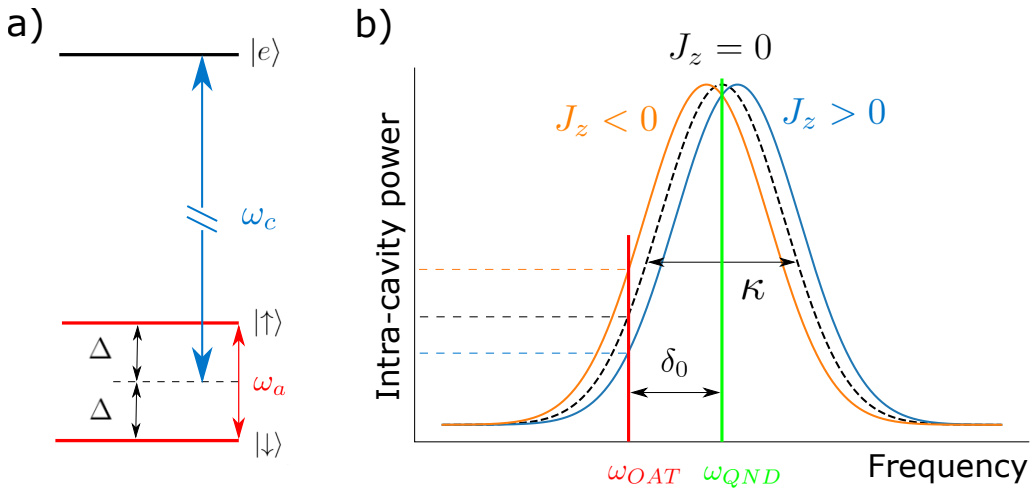

Figure 2.3: (a) The cavity resonance is tuned such that $|\uparrow\rangle$ state is detuned positively by $\omega_a/2$ whereas $|\downarrow\rangle$ state is detuned negatively by $\omega_a/2$. (b) An illustration of the resonator frequency shift due to the change in population difference ($2J_z = \Delta n$)). When the probe light is detuned by δ_0 (red line) as shown in figure, positive change in population difference (blue lines) decreases intra-cavity power whereas negative change in population difference (orange lines) increases it, resulting in OAT interaction. In case of resonant driving (green line) OAT interaction is negligible if the uncertainty of the state in J_z is smaller than cavity linewidth κ.

$$H_{\text{eff}} = \hbar\omega_c a^\dagger a + \hbar\Omega a^\dagger a J_z + \hbar\omega_a J_z,$$

where $\Omega = 2g^2/|\Delta|$. The first term describes the energy of the light in the cavity, while the last term describes the energy of the atoms. The interaction term $\hbar\Omega a^\dagger a J_z$ can be grouped either with the first term to describe the cavity resonance shift:

$$H_{\text{eff}} = \hbar a^\dagger a(\omega_c + \Omega J_z) + \hbar\omega_a J_z,$$

or with the last term to describe the light shifts experienced by the atoms:

$$H_{\text{eff}} = \hbar\omega_c a^\dagger a + \hbar(\Omega a^\dagger a + \omega_a)J_z.$$

To sum up, coupling of the atoms to a resonator has a two-fold effect: first, is a differential light shift (AC Stark shift) that cause precession of each individual spin along z-axis; and second, is a cavity resonance shift due to modified index of refraction. Once the cavity resonance frequency dependence on J_z is set, there are two ways of creating desired SSS either by inducing one axis twisting (OAT) interaction or by performing quantum nondemolition (QND) measurement.

2.2.2 One axis twisting

By driving the cavity with a detuned probe at constant power one can introduce the so called J_z^2 interaction. Since the cavity resonance and hence the detuning depend on J_z (see figure 2.3(b)) the photon number $a^\dagger a$ in the interaction term $\hbar\Omega a^\dagger a J_z$ has a linear term that depends on J_z. This gives rise to the term $H \propto J_z^2$ that rotates the state around z-axis with angular

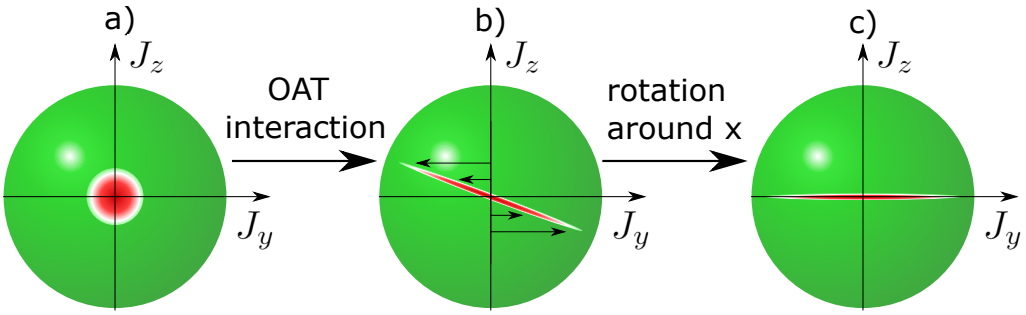

Figure 2.4: The Wigner quasiprobability distribution for CSS state (a) is sheared under the OAT Hamiltonian (b). In order to enhance measurement precision in J_z projection the state should be rotated around x-axis (c).

speed depending on J_z. In other words, parts of the uncertainty region with larger J_z are rotated more and overall uncertainty region is sheared as shown in figure 2.4(b).

Apart from J_z^2 term there are also J_z terms that cause global rotations of the state irrespective of J_z. The amount of shearing and the angle of rotation due to linear term are proportional to the probe pulse area. Due to the latter dependence any power fluctuations increase the uncertainty in the final position of the state on the Bloch sphere. This degrades the precision of further measurement, as state needs to be oriented with the least noisy projection to measurement sensitive axis. The advantage of this method is that it is unconditional, meaning that it does not alternate in different realizations under the same conditions.

2.2.3 Quantum non-demolition measurements

By performing collective measurement of the population difference one can project the system into a state with reduced uncertainty in z projection. The position of the resulting state on the Bloch sphere depends on the measurement outcome (see figure 2.5(a)). Population difference measurement is usually done by measuring the phase acquired by light after resonating in the cavity due to the change in index of refraction induced by atoms. A requirement for a reliable QND measurement based squeezing is $\Delta J_z < \kappa$. As in CSS $\Delta J_z = \sqrt{N}/2$ for large number of atoms it may not always be the case. In order to allow QND measurement based squeezing one can make use of OAT induced pre-squeezing to decrease ΔJ_z. The consecutive application of OAT and QND measurement based squeezing was used to enhance the precision of measurement 100 times beyond SQL [HEKK16].

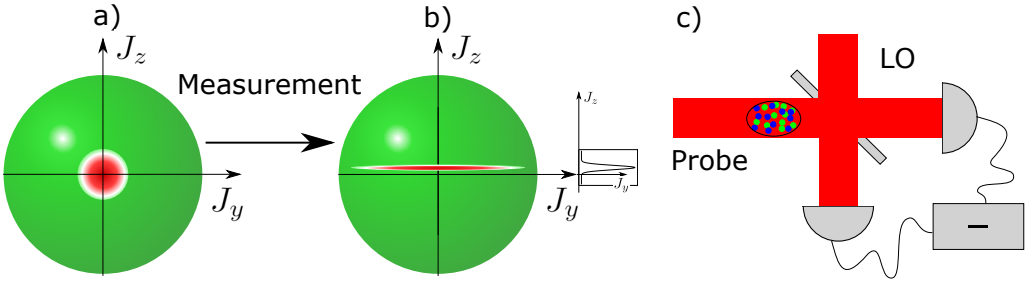

Figure 2.5: QND measurement projects initially CSS (a) into a SSS (b) with reduced uncertainty in J_z projection and shifted depending on the outcome of the measurement. (c) Schematic diagram of possible measurement of the population difference. Atoms are illuminated with a probe light, which is then interfered with local oscillator (LO) for homodyne measurement.

2.3 Analog feedback control systems

The concept of feedback has proven to be a cornerstone in achieving accurate and stable operation across a wide range of applications. From regulating the temperature in the room to guiding spacecraft in deep space, feedback control systems play crucial role in ensuring desired outcomes in the presence of disturbances. There are many sources of instabilities in experimental setups such as temperature fluctuations, mechanical vibrations and drifts, electronic noise, electromagnetic interference and many others. Without proper feedback stabilization the phenomenon of interest might be buried under the noise floor. Therefore, in our lab we implemented feedback control systems to stabilize different parameters like cavity lengths, laser frequencies, laser temperatures, laser intensities, and magnetic fields.

In this section, we explore the foundational components and principles of feedback control systems. We delve into the concept of closed loop control, which involves monitoring the system's state and generating control signals for precise regulation. This closed loop control is described in three core components: the system, the error signal generator, and the feedback.

To give the intuition on this framework, we will consider the scenario of temperature stabilization, where each component's role become evident. Subsequently, a more formal description of instability, the frequency response, stability analysis, and the role of gain and phase margins will be covered. By exploring these concepts, we gain insights into how feedback control systems are designed, and how their stability can be characterized and optimized.

In the last part of the section, we will describe the nuances of analog feedback systems, the role of operational amplifiers (op-amps), and their capabilities in designing effective analog feedback systems. We will also explore how op-amps can be harnessed to construct versatile filters and discuss their applications in analog feedback control systems. By building a solid understanding of these principles and components, we lay the groundwork for understanding the details of the control systems implemented in our lab. The section is written as a practical guide for someone in the lab to be able to get going with building analog feedback systems, and is not meant to be a compehensive overview. While I will lay out some basic principles here, for more detailed information the reader can refere to references [Man02], [AM08].

2.3.1 Components and principles

At the heart of any feedback control system is the concept of a closed loop control. It involves continuous monitoring of the system's current state and generating a control signal that drives the system towards a desired set point. This closed loop can be described by three components: the system, which represents the physical or abstract process being controlled; the error signal generator, responsible for computing the error signal by comparing the desired set point with the system's actual output; and the feedback, which acts on the system as a response to error signal to minimize it and hence bring the system closer to the desired state.

To illustrate this concept, consider the scenario of temperature stabilization. In this case, the system will refer to the object requiring temperature control. The error signal generator will involve performing analog subtraction between the set temperature and the current temperature reading from thermometer. The value of the error signal is proportional to the discrepancy between the current and desired states of the system. Therefore, the system is being steered in the direction of the desired state by minimizing the error signal. Finally, the feedback component will act to dynamically cool the object when the temperature is high and heat it when the temperature is low. Note that the heating and cooling component can be

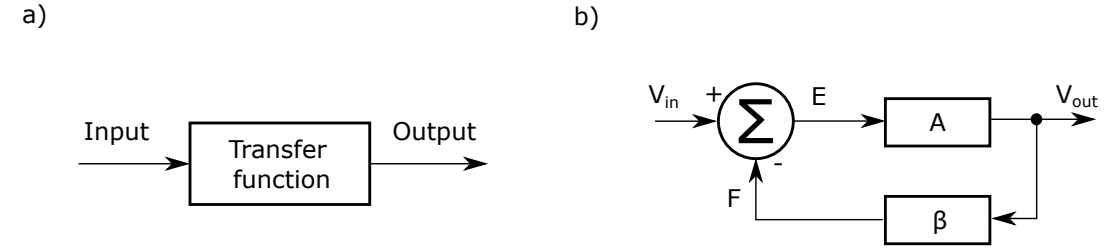

Figure 2.6: a) Illustration of a single block diagram. Input and output are shown as arrows pointing to and from the block respectively b) Block diagram of a simple feedback loop. A and β are transfer functions of the system and feedback respectively.

conceptually either a part of a system or a feedback. It is left to the reader to decide where to include it, since there is no benefit in either of choices.

After acquiring intuition about working principles of feedback control systems let's describe it in a more formal way. Any control system can be represented as a block diagram, that is a graphical representation illustrating the functional components of a system and the relationship between them, using interconnected blocks. Each block has its own transfer function, that is a mathematical representation describing the relationship between the input and output of a block in a form of $V_{out} = V_{in}T$. A simple block diagram of a negative feedback loop β acting on a system with a transfer function A is shown in figure 2.6. Error signal E after passing through the system with transfer function A becomes $V_{out} = EA$. Similarly, the feedback can be written in terms of V_{out} as $F = V_{out}\beta$. The final piece of the block diagram is a summation operation $V_{in} - F = E$. Solving all three equations describing the block diagram together, the error signal can be written as:

$$E = \frac{V_{in}}{1 + \beta A}. \tag{2.1}$$

In the absence of feedback, $E = V_{in}$, which implies that regardless of the source of the disturbance, the feedback compensates for its effect by an amount equal to the closed-loop gain, in this particular example $|1 + \beta$A$|$. Therefore, the larger loop gains are attractive for minimizing the errors and making the lock tighter. However, there is always a competing effect to increasing the closed loop gain that can lead to instabilities. In particular, when the closed loop transfer function approaches zero, the error signal approaches infinity, making the feedback unstable. This leads us to the description of stability analysis of feedback control systems.

2.3.2 Frequency response

Stability analysis of a system in general might be quite complicated. However, in many practical applications the frequency response analysis might be sufficient. For instance, frequency response analysis does not include the in-depth information about the response to the step-like functions. However, it provides sufficient enough information about the general stability criteria that we successfully implemented in our lab.

In many cases, the response of a system depends on the frequency content of its input signal. For instance, the audio speaker might respond differently to low frequency bass notes than it does to high frequency treble notes. The concept of frequency response serves as a powerful

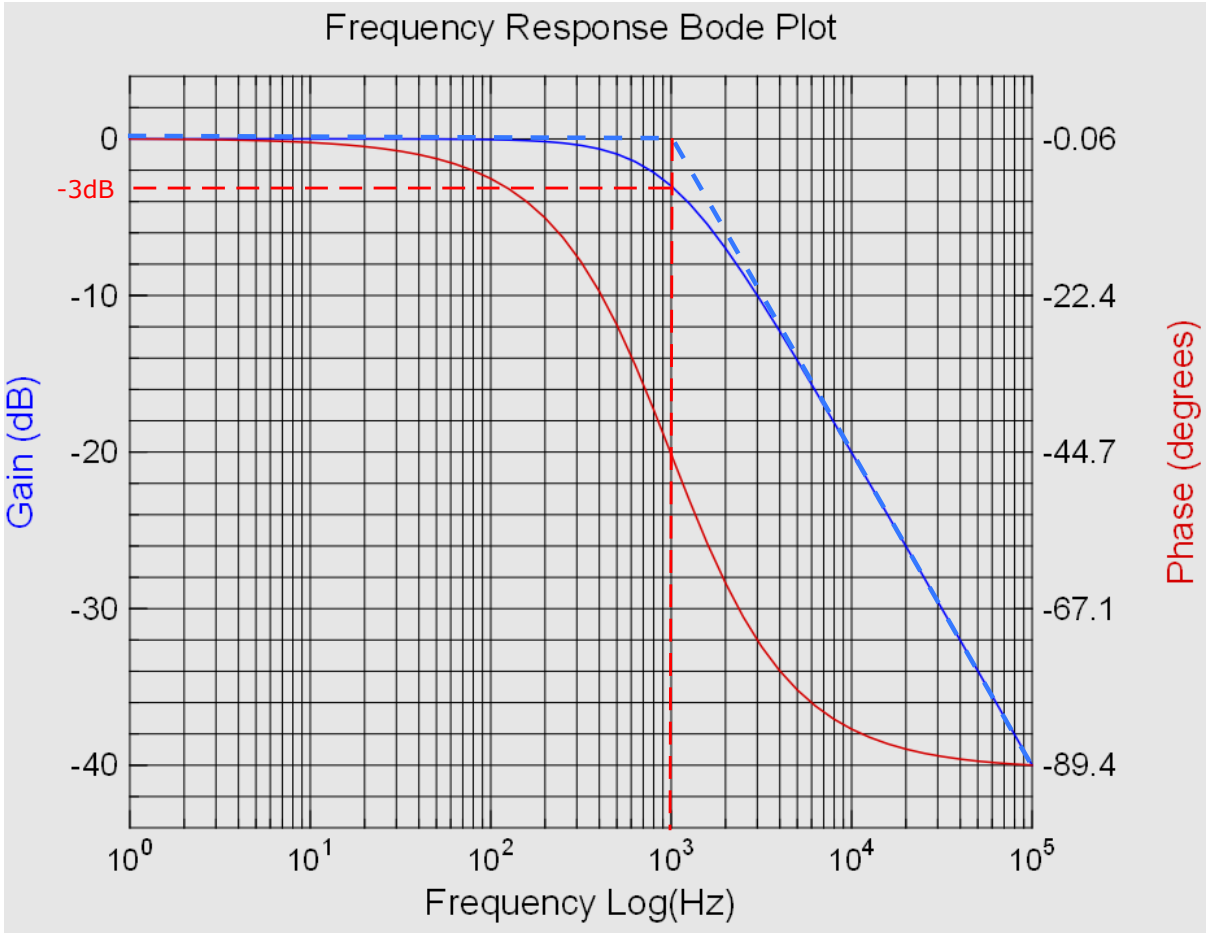

Figure 2.7: Frequency response Bode plot of a low pass filter with a corner frequency of 1 kHz obtained from PiscoScope 5000. Purple line indicates the actual gain, whereas blue dashed line represents its linear approximation. Red line shows the phase of the output signal.

tool for analyzing and understanding the behavior of dynamic systems. It is very similar to the concept of transfer function, but typically represented through the use of Bode plots that do not require closed mathematical form.

Bode plots consist of two separate graphs: one depicting the gain response in decibels and the other one showing the phase shift in degrees, both as a function of logarithmic scale of input signal frequency. Frequency response characterization is done by applying a single frequency tone and measuring the frequency dependency of the gain and relative phase of the output signal. We use PicoScope 5000 with the provided software that sweeps the frequency and generates frequency response plots in a matter of several minutes. A bode plot of a single pole low pass filter with 1 kHz corner frequency is shown in figure 2.7. The blue dashed line is a linear approximation of a frequency response that is typically used for tailoring frequency response of a system. A single pole low pass filter introduces a slope of -20 dB/decade after the corner frequency to the gain response, and a gradual phase accumulation of $-90°$ over the course of 4 decades with $-45°$ at the corner frequency to the phase response. The actual gain frequency response is 3 dB lower than the approximation at corner frequency. Single pole high pass filter has similar characteristics but adds positive slope of 20 dB/decade to the gain and positive $90°$ to the phase shift. The frequency response is typically tuned by introducing low pass and high pass filters at various corner frequencies to achieve the best feedback performance.

2.3.3 Stability analysis

First, let's intuitively understand why feedback can become unstable in the context of temperature stabilization. It is evident that we must avoid abrupt heating of the object whenever the temperature falls below the set point. This precaution is essential due to the finite thermalization time required for the object's temperature to adjust. An overreaction to temperature changes could lead to overshooting and the well known 'ringing' phenomenon. Consequently, instead of gradually stabilizing the temperature around the set value, the system will oscillate, causing fluctuations around the desired temperature. Conversely, in cases of under-reaction to temperature changes, it might be impossible to reach the set point, as disturbances can outweigh the corrections from feedback. These complexities encountered in control algorithms lay the foundation for the concepts of tightness and stability of the feedback loop.

Now let's closely examine the formal description of instability. Typically, feedback is designed to be negative at low frequencies to minimize errors. However, with increasing frequencies, the feedback accumulates a relative phase shift due to the presence of zeros and poles inherent in any system. As observed from equation 2.1, a unity loop gain at 180° phase shift lead to the amplification of the error signal, thereby causing instability. Moreover, when the loop gain exceeds unity at the 180° phase shift the resulting feedback signal drives the system away from the desired state causing the railing of the utilized op-amps. Due to the inherent response limitations of any system the 180° phase shift of the feedback signal is unavoidable. Therefore, the approach to designing a tight and stable feedback control system is to attenuate the signal at the 180° phase shift point below unity gain and extend that point to the highest possible frequency. Recall that the amount of gain corresponds to the noise suppression at given frequency. By placing the unity gain as far as possible in frequency, the noise suppression is maximized. The frequency at which the loop gain becomes unity is known as feedback frequency bandwidth. It is an important parameter of a feedback control system that indicates the maximum responsiveness of the lock. For instance, a feedback loop with 1 MHz bandwidth can suppress noise up to 1 MHz and assumed to be insensitive to higher frequencies. It's possible to extend the feedback frequency bandwidth by compensating zeroes and poles. However, every system has a natural limit of responsiveness that can not be exceeded. For instance, it is impossible to design a feedback system that operates faster than the time scale required for the material to thermally stabilize in the context of temperature stabilization.

The degree of system stability is characterized by the gain and phase margins. They represent the amount by which the closed loop gain and phase can be increased until the system becomes unstable. For instance, when the 180° phase point is at -6 dB it means that the gain margin is 6 dB. Similarly, a unity gain point at 140° indicates a 40° phase margin. Typically, gain and phase margins of 6 dB and 40° respectively, are considered to be stable. However, the exact values may vary for different control systems. In addition, insufficient phase or gain margin may affect the step function response of a system resulting in the transient oscillation or even falling out of lock. More detailed stability analysis can be performed by Nyquist stability criterion. However, for the analysis of linear, time-invariant systems that have single input and output, conventional frequency response analysis using Bode plots is sufficient. Fortunately, all our systems of interest do comply with the aforementioned criterion. Therefore we achieved satisfactory stability results with a sufficient phase and gain margins by analyzing Bode plots.

2.3.4 Analog feedback systems

The choice between digital and analog feedback systems depends on a variety of factors, each with its own set of advantages and considerations. Analog feedback systems can provide real-time responsiveness due to continuous nature of analog signals as opposed to digital feedback systems that have latency depending on the hardware capabilities and signal processing requirements. In addition, analog feedback systems do not suffer from digitization effects or sampling artifacts, which lead to smoother transitions and potentially reduce the risk of issues like noise amplification. However, digital feedback systems are very flexible in terms of frequency response shaping and increasing the bandwidth, that may be challenging to implement with analog components. Also, digital feedback systems are more suitable for seamless integration with other digital devices enabling communication, data logging and analysis. Since the demands of our lab can be easily fulfilled with analog feedback systems, every stabilization mechanism was implemented with analog components.

2.3.5 Operational amplifiers

One of the foundational building blocks in the field of analog electronics are operational amplifiers, commonly known as op-amps. With their versatility, amplification capabilities, and ability to process signals with high precision, op-amps became essential components for engineers and scientists in the design of effective feedback control mechanisms. They can be employed as amplifiers, inverters, filters, summation and subtraction devices, comparators and many more.

Op-amps are very convenient for the design of analog feedback systems due to their buffering capabilities. It is possible to tailor the frequency response by implementing a low-pass filter with RC pairs. However, in order to stack them back to back, one needs to ensure that the resistance of the following RC pair is few orders of magnitude larger than previous one. This puts a strict limitation on the design options due to availability of components. Contrary, with op-amps as filters there is no limit in the number of sequential implementations that can be done even with the same RC pair values. Each op-amp transfer function can be tuned nearly independently and then put together as lego blocks. In addition, it is possible to incorporate several filters with different corner frequencies and amplification in a single op-amp.

It is worth noting that when using op-amps for shaping the frequency response of the closed loop feedback, one also needs to pay attention to the stability of individual op-amps. However, that topic is out of the scope of this thesis but is very crucial for overall stability of the feedback systems.

CHAPTER 3

Experimental setup

In this chapter we will describe the parts of the experimental setup. Each section will be provided with the reasoning behind certain design decisions, parts of implementation details, and characterizations.

3.1 Science cavity

At the core of our experimental setup is the ring cavity that is comprised of two plane and one concave mirror that form a nearly equilateral triangle as shown in figure 3.1. The cavity is mainly used to enhance the light-matter interaction. In particular, light resonating in the cavity interacts with atoms multiple times and acquires phase shift during each round trip. Therefore, the effective interaction is increased by the amount of round trips before escaping the cavity. In addition, the cavity allows the introduction of OAT interactions and perform QND measurements utilized for spin squeezing. Also since cavity acts as a resonator the setup requires less powers for trapping, probing and manipulating the atoms due to the light build up in the resonator. Furthermore, since Raman beams are coupled to the cavity, they are automatically aligned with the intended separation axis.

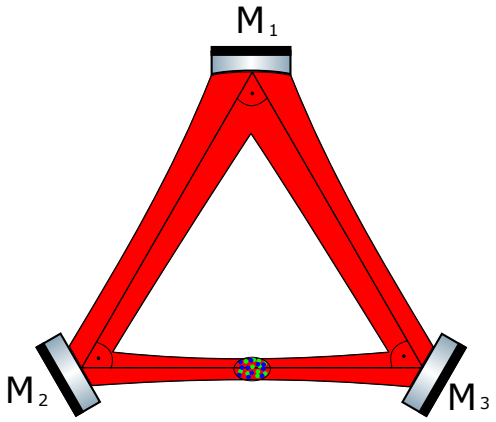

Figure 3.1: Schematic diagram of the ring cavity. M_1 is a concave mirror, whereas M_2 and M_3 are plane mirrors. The atoms are trapped at the single cavity waist between two plane mirrors.

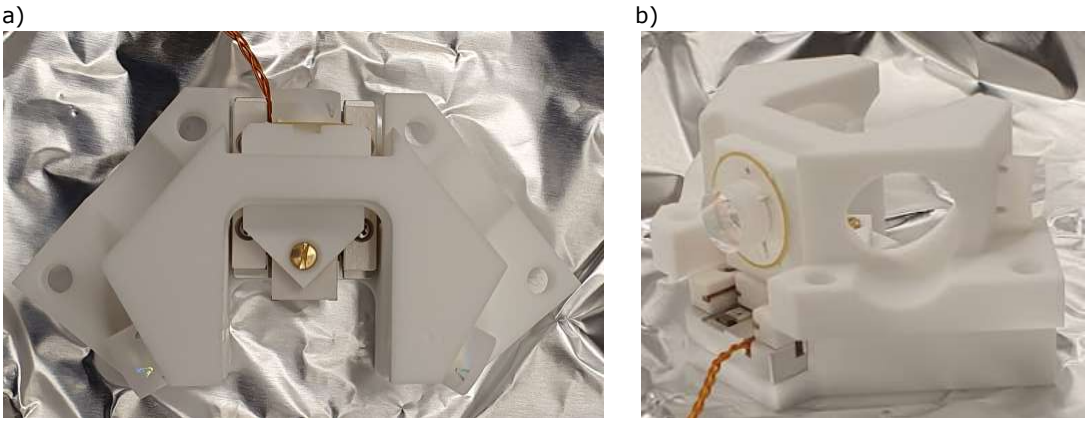

Figure 3.2: Images of a custom made macor piece holding the science cavity. a) Top view showing the ring cavity mirrors arrangement. b) Side view showing the placement of curved mirror on a ring piezo that is glued on the stand of linear translational stage. Image credit: Sebastian Wald.

Another reason for using a ring cavity is that it allows the creation of a travelling wave, as opposed to the standing wave in linear cavities. The trapping laser creates a red detuned propagating dipole trap to attract the atoms to the intensity maxima, that corresponds to the beam waist. Our design allows nearly free motion along the cavity axis while preserving strong confinement in perpendicular directions. The estimated ratio of the trap frequencies in axial directions and along the cavity axis is about 500. The purpose is to simulate a configuration similar to atomic fountains, but with better control, since atoms will remain trapped in axial directions during interrogation times. Furthermore, the ring cavity results in more homogeneous intensity of the probe light seen by different atoms, and hence decrease dephasing compared to inhomogeneous broadening of the clock transition in linear cavities.

However, beside aforementioned advantages of utilizing the cavity there are complications that needs to be taken into account. Since Raman pulses are coupled to the cavity, their beam sizes are limited by the cavity, and might introduce position dependent AC-Stark shift. This needs to be tested and if needed the confinement of the atoms can be made tighter either by increasing the dipole trap depth or by introducing additional trapping potential in vertical direction. We might also compensate for the induced AC Stark shift using a far detuned $1527\,\mathrm{nm}$ laser that minimally affects the rest. The mode overlap between $1560\,\mathrm{nm}$ and $1527\,\mathrm{nm}$ is expected to be sufficient. However, the efficiency of this compensation approach will need to be verified experimentally.

Also, since the presence of the cavity requires both Raman beams to be somewhat resonant to the cavity, it puts a stringent requirement on the mirror reflectivities. Since one of the Raman beams needs to be frequency tuned for effective state dependent separation of the cloud, mirrors were customized to make a high finesse cavity for P polarization and low finesse cavity for S polarization. The manufacturing of the mirrors was outsourced to Layertec.

All cavity mirrors are mounted on a custom made macor piece shown in figure 3.2. The choice of macor was done because it is non-metallic and hence it allows microwaves to pass through and manipulate the atoms. Furthermore, it is a machinable ceramic and can be used to machine complex structure. The curved mirror is glued on a piezo-electric transducer that is glued on a translational stage. This allows fine tuning the cavity free spectral range to make both Raman beams resonant to the cavity. Note that due to complicated demands on the mirror coatings P and S polarizations acquire different phase shifts. Therefore, the resonance

conditions for both was adjusted by tuning the cavity length with linear translational stage.

The free spectral range of the cavity was designed to be 3.4 GHz that is roughly the half of the canonical hyperfine transition of ^{87}Rb atoms. The purpose is to drive Raman transitions using two optical tones simultaneously supported by the cavity and have a reasonable cavity length. These tones will have a detuning of 6.8 GHz, corresponding to the hyperfine transition of ^{87}Rb atoms. More details on the Raman beams will be provided in the chapter 3.6.5.

3.2 Vacuum chamber

To maintain coherence of utilized quantum states, the system should be well isolated from the environment. In particular, collisions from the background gas molecules can cause loss of atoms in atomic clouds. Therefore, cold atoms experiments generally require ultra high vacuum (UHV) to extend the lifetime of the atomic cloud beyond the time required to perform a single experimental sequence. Our vacuum system consists of a custom design manufactured by Kimball shown in figure3.3. An atom source is connected from the back and the atoms are injected through a pinhole in the back of the chamber.

Reaching UHV is a time consuming and tedious process. General procedures involve achieving the required levels of UHV with an empty vacuum chamber and blank flanges. In our case we were targeting 10^{-11} mbar levels. After reaching the intended levels of UHV we could replace components sequentially to be able to troubleshoot in case we would not reach UHV. Each new installation step was followed by pumping the chamber to 10^{-6} mbar levels with a Turbo Pump and then activating a getter and an ion pump. Sometimes we needed to bake the system to drive out gasses and other contaminants trapped in the surface of the chamber. Custom coated view ports put a backing temperature restriction to about $100\,^{\circ}$C that lead for week long backing periods.

Throughout the installation process we found out that some of the custom designed view ports were leaky and limited the vacuum pressure to the 10^{-9} mbar. We used a residual gas analyzer and a nozzle with a helium gas to find the leak. After that we replaced leaky view ports and reached the intended UHV levels. Large top and bottom antireflective-coated view ports were also leaky. Due to the long lead times we decided to keep uncoated view ports at the expense of having additional reflections in order to move forward.

Final pressure of the chamber after replacing side view ports with antireflective-coated ones and installing the cavity we reached the pressure levels of 1×10^{-10} mbar that were below the ambient pressure with activated atom source. Although there is a debate about the precision of the pressure measurements at that low pressures we infer the pressure from the getter current. Such relative measure of the pressure is sufficient for our purposes since we can indirectly evaluate the quality of the UHV by looking at the MOT life time that is on the order of 10 s. More details regarding the life time are in the next chapter3.3.

3.3 Atom source

As rubidium source we employ ColdQuanta photonically integrated cold atom source. It is a commercial, alignment free product that is connected to the back of the main vacuum chamber. It consists of two rubidium filaments, optical distribution system, and permanent magnets that generate quadruple magnetic field. When the current is applied on the filament it evaporates rubidium atoms that are captured in a 2D-plus MOT [Sal11]. Trapped atoms create a cigar

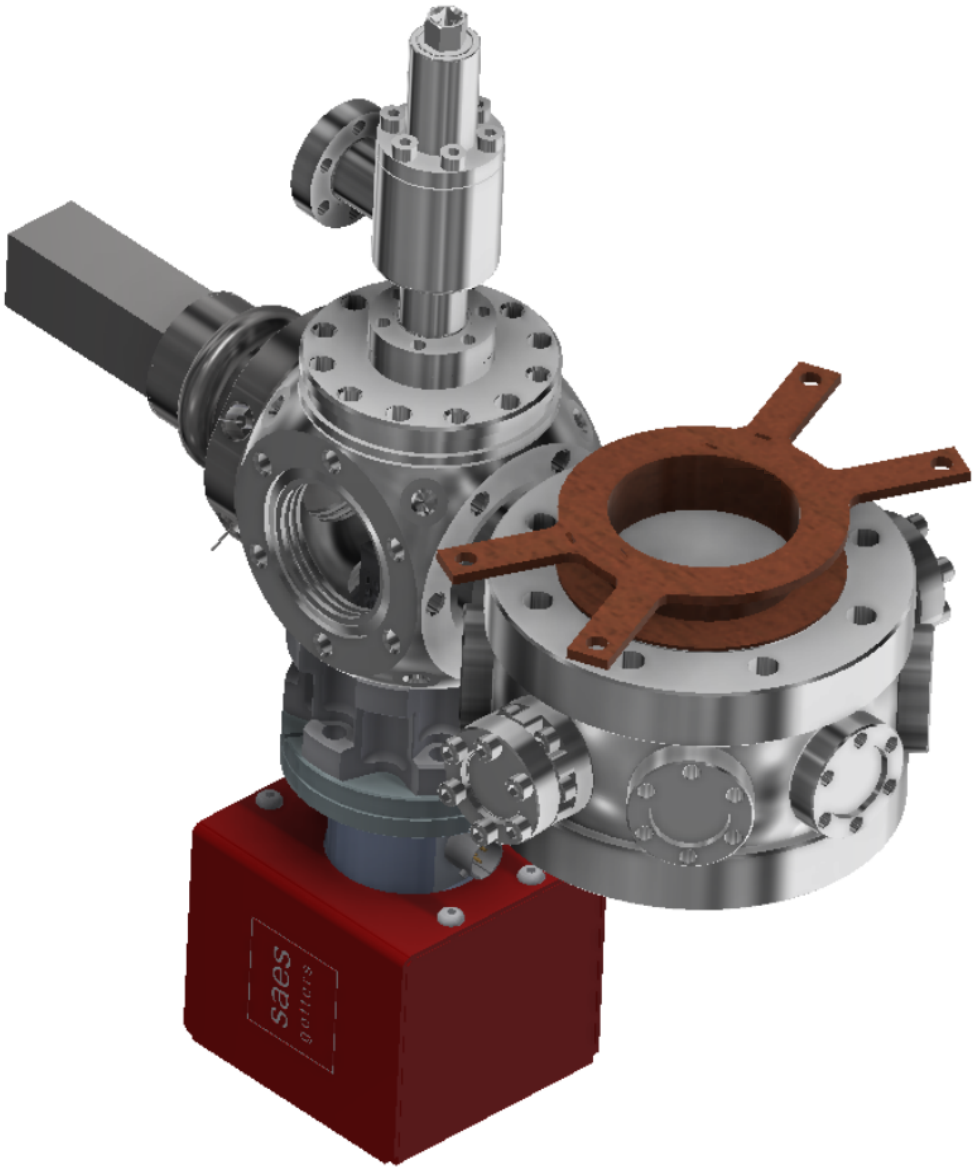

Figure 3.3: CAD drawing of the vacuum chamber. Atom source is connected from the back, shown in dark grey color. Ion getter pump is located at the bottom shown in red color. Cavity is in the front cylindrical chamber.

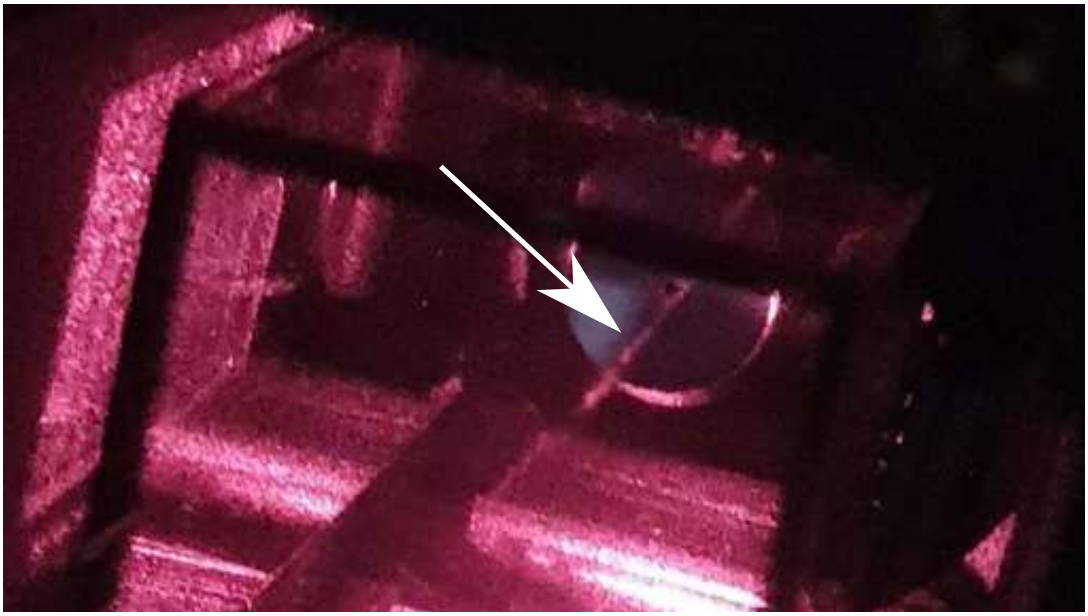

Figure 3.4: Image of the 2D MOT cigar shaped filament. White arrow pointing the cloud.

shaped atomic cloud that injects rubidium atoms into the main chamber through the pinhole. The push beam increases atomic flux and also applies additional confinement. Therefore, the name is 2D-plus MOT. The coarse alignment of the push beam was done by aligning the location of the atomic cloud with the pinhole when observed by a camera from the back of the atom source with the removed back cover. Fine tuning is then done by maximizing the equilibrium atom number of the 3D MOT. The atom source that is currently being employed was custom optimized for our vacuum chamber design. After receiving the atom source, we observed 3D MOT loading rates much lower than the specifications. We assume this might be due poor optimization for out system that resulted in diffusing atomic beam. Our reasoning is that we can increase the current, and hence increase the ambient pressures to the levels, that should correspond to larger 3D MOT loading rates. The increase of the ambient pressure means that many atoms are being transferred into the science chamber. However, the 3D MOT loading rate might be low due to the large directional spread of the atoms.

Cooling and repump beams are combined and fiber coupled to the atom source. The coupling efficiencies were about $50\,\%$ for each beam. We compensated it by increasing the input powers. The total powers of cooling, rempump and push beams fibered into atom source are shown in the table3.2.

2D I		2D II		2D Push	
Cooling	Repump	Cooling	Repump	Cooling	Repump
15.3 mW	1.5 mW	15.3 mW	3.3 mW	4.0 mW	1.0 mW

Table 3.1: Table showing input powers of atom source. 2D I and 2D II are two cooling lasers inputs.

The amount of current applied on the filament controls the evaporation rate and hence the atomic flux into the main chamber. Larger atomic flux can reduce the loading times that usually constitutes the largest portion of the experimental sequence. However, larger atomic flux results in the increase of the ambient atoms density. We characterized the equilibrium pressures, 3D MOT lifetimes, and number of atoms loaded into 3D MOT in $20\,\mathrm{s}$ shown in

the table 3.2. Since the excess of the atomic flux might slowly saturate the getter material we decided to set the current to $2.6\,\mathrm{A}$. Due to the relatively high current driven through the filament it takes about $20\,\mathrm{min}$ to thermalize.

Current (A)	Pressure (mbar)	Life-time (s)	Atom #(mil)
2.5	5.7e-10	20.8	6.5
2.6	6.3e-10	15.8	16.1
2.7	8.2e-10	11.3	20.0

Table 3.2: Table showing different configurations of the current applied on the atom source filament.

The lifetime of the 3D MOT was characterized by fitting the exponential decay $N(t) = N_0(1 - e^{-\frac{t}{T}})$ on the total fluorescence intensity instead of atom number to simplify the calculations. Lifetime is a characteristic time after which the intensity decreases by $1/\mathrm{e}$ with respect to the initial value.

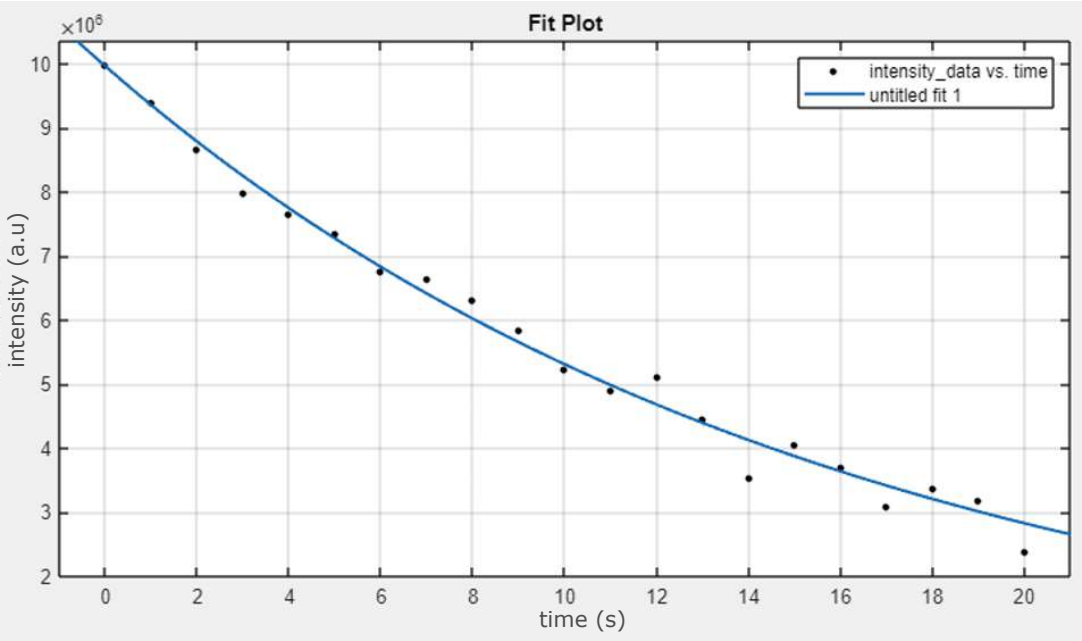

Figure 3.5: An example of the exponential decay fit to calculate the lifetime of the 3D MOT. Life time of the fit is $15.8\,\mathrm{s}$.

3.4 Magnetic field compensation

Precision measurements performed by utilizing cold atomic clouds are relying on the fact that atomic energy splittings remain uniform under the same conditions. One of those conditions is a magnetic field seen by the atoms, as it can give rise to the splitting and shifting of atomic energy levels. This effect, known as Zeeman shift, can contribute to additional systematic noise and even destroy rather fragile quantum correlations that we are interested in employing. In addition, magnetic field defines the position of atomic cloud in magneto-optical traps and hence can vary the amount of atoms loaded into the cavity mode. Furthermore, magnetic field defines quantization axis that acts as a reference for RF pulses used to manipulate internal states of the atoms. Perturbations in the direction of quantization axis imprints noise onto RF pulses and hence degrade manipulation accuracy. Therefore, proper control over the magnetic field is essential in performing cold atoms experiments.

External magnetic fields can arise from multitude of sources, including magnetic field of Earth, environmental factors, electromagnetic interference, and even the experimental apparatus itself. One of the largest contributions to background magnetic field in our lab is approximately 650 milligaus of Earth's magnetic field. In addition, we have measured magnetic field fluctuations of around tens of miligauss due to activities from two labs located in the same building as ours.

Apart from the aforementioned external magnetic fields there are also so called quenching fields that originate from the relaxation of transient fields and Eddy currents within the coil windings and the surrounding materials. This effect is mainly seen when MOT coils are being turned on and off as it induces huge magnetic field changes. Although we can not compensate quenching fields completely, our magnetic field stabilization suppresses some of its lower frequency components.

In order to address aforementioned requirements we built magnetic field compensation bias coils and implemented analog feedback control system with a variable set point to allow high precision control over magnetic field in our experiment.

3.4.1 Bias coils

Since each projection of the magnetic field is independent from each other, in order to gain the full control over magnetic field one needs to be able to introduce bias fields in all three dimensions. A good candidate for generating nearly uniform magnetic field in one direction is a pair of coils in a Helmholz configuration. It consists of two identical coils placed at a distance with their faces parallel to each other and connectorized such that magnetic field components perpendicular to the coils' plane add up while other components are being canceled at the central region between them. A cage formed from three such bias coil pairs is capable of generating magnetic field in all three dimensions.

Our magnetic field compensation cage is 86.5 cm wide, 102.5 cm long, and 65.5 cm high. Each individual coil has 48 turns of 1.6 mm wide copper wire with double enamel coating for better isolation. We used 1.6 mm wide wires to reduce the resistance of coils and subsequently decrease power dissipation. This is because magnetic field depends on the number of turns, current, and coil dimensions, which are almost not affected by wire dimensions. Resistances of each coil are ranging between $1.15\,\Omega$ - $1.45\,\Omega$.

Each coil frame was built from aluminum bars glued to each other with angle brackets. The corners were smoothed and sandpapered to prevent sharp edges that might damage the

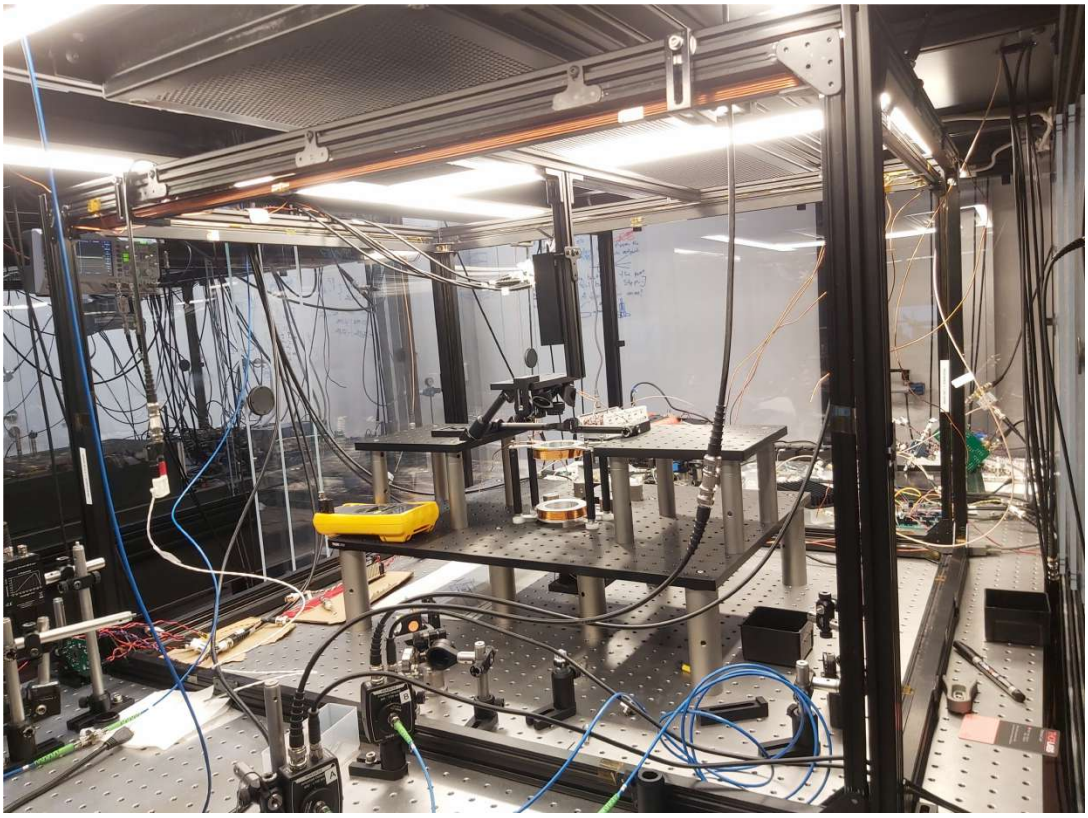

Figure 3.6: Image of the magnetic field compensation cage.

isolation and introduce shorts. The frame of each coil has a rectangular shape with curved angles. The winding of coils was done under the constant tension applied by squeezing the wire between a plastic foam in a vice and rotating the frame on a mechanical construction. The width of the frame was roughly 6.5 times larger that the diameters of wire, allowing to start each next layer in between of two wires of previous one. In the end of the winding it was fixed with glue for better stability.

3.4.2 Magnetic field stabilization

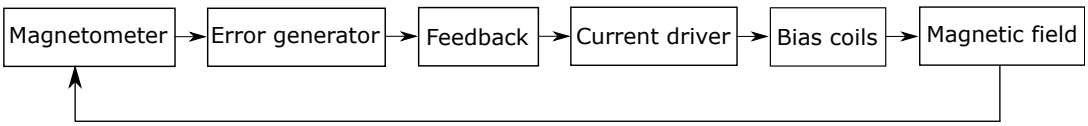

Figure 3.7: Functional block diagram of a closed loop feedback control system for magnetic field compensation.

Having the ability to independently introduce bias fields in three dimensions, we can decompose the problem into three analogous tasks. These tasks involve active monitoring of magnetic fields and the adjustment of bias coils current to maintain stability around a variable set point in each respective dimension. Block diagram describing the magnetic field compensation for a single dimension is shown in figure 3.7. For detailed description of the feedback schematics please refer to Appendix A. The error signal in our analog feedback control system is generated by performing analog difference operation between the observed magnetic field and a set point that can be adjusted by applying analog control voltage. It is then fed to the home built

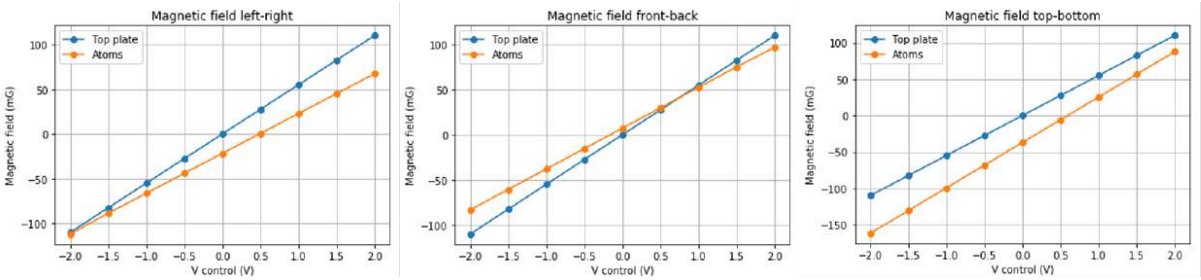

Figure 3.8: Plots showing the difference between the magnetic field measured at the top plate and at the location of the atoms. Plots were obtained by applying magnetic field offsets on the magnetic field compensation feedback and measuring the resulting magnetic field on two magnetometers, one placed at the top plate and another one at the intended location of the atoms.

analog feedback circuit that drivers the bias coils and stabilizes the magnetic field to a fixed value.

Since it is impossible to measure the magnetic field right at the position of atoms, magnetometer should be placed as close as possible to the intended place of stabilization. In our setup the magnetometer is placed on a top plate that is measuring about $17.7\,\text{cm}$ above the position of atoms. Before installing the vacuum chamber we have measured the magnetic field at the position of atoms and on the top plate simultaneously by driving the bias coils with different current settings. The results show that there is a linear dependence between the observed magnetic field and the magnetic field seen by the atoms. Thus, by stabilizing the magnetic field at the top plate to a certain value $\vec{B}_{\text{obs}} = (\vec{B}_x, \vec{B}_y, \vec{B}_z)$ we are stabilizing the magnetic field at the position of the atoms to a value $\vec{B}_{\text{atoms}} = \vec{B}_{\text{obs}} + \vec{B}_{\text{offset}}$. We do not care about the offsets as long as we can stabilize and vary the set point, since we are going to use the best magnetic field sensors – atoms, to calibrate the set values. Recall the aforementioned Zeeman effect that splits the atomic energy level manifold. Zeroing magnetic field is done by performing microwave spectroscopy on the atoms and set by eliminating Zeeman splitting. Since Zeeman splitting depends on the magnitude of the magnetic field, zeroing was performed by varying each projection of the magnetic field and iteratively decrease in Zeeman splitting. An example of the Zeeman splitting is shown in figure 3.9.

Note, that in the current configuration of magnetic field compensation is not capable of applying magnetic field gradients, that can lead to position dependent inhomogeneities. The reason for that is because magnetic field from a simple circular loop calculated by Biot-Savart law at a distant point is $B \propto 1/r^3$ and hence the gradient decays as $1/r^4$. This means that in order to generate significant amount of magnetic field gradient the source needs to be very close to atoms. Before installing the vacuum chamber the magnetic field gradient was measured to be negligible. Therefore, the vacuum chamber material, screws, and everything that is placed close to the location of the atoms was chosen to be non magnetic. In the current setup it was decided that magnetic field compensation would be sufficient.

3.5 MOT Coils

MOT coils are employed to generate magnetic field gradient to trap and cool atoms. They consist of two cylindrical coils with a height of $1.36\,\text{cm}$ and inner and outer diameters measuring $5.1\,\text{cm}$ and $7.7\,\text{cm}$, respectively. MOT coils were winded on an aluminum construction shown

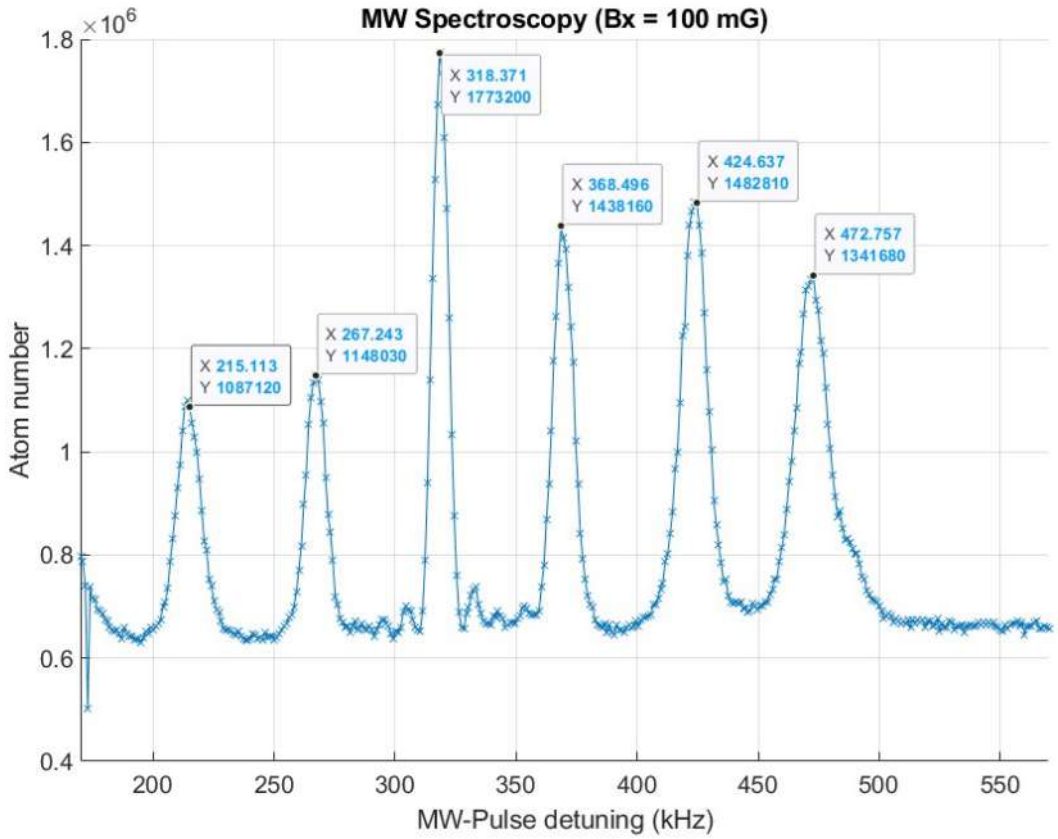

Figure 3.9: Zeeman splitting originating from the residual magnetic field observed by the energy splitting of the magnetically sensitive sublevels. Microwave spectroscopy was performed by applying a π pulse at different microwave pulse detunings and pushing away the rest of the atoms and imaging it to determine the number of atoms that were resonant with the applied π pulse. The background was not subtracted in the plot, resulting in a non zero offset. It did not affect the measurement results as peak separation was not affected by the offset. Plot credit: Edward Gheorghita.

in figure 3.10. Each coil has 144 turns and completely fills the region on aluminum holder dedicated for MOT coil. Two coils are placed co-axially with their closest parts being separated by $7.7\,\text{cm}$ and connected in an Anti-Helmholz configuration that results in large magnetic field gradient in the central region between two coils.

The calculation of the magnetic field gradient generated by a pair of MOT coils, aimed at determining the necessary dimensions and number of turns, is based on the assumption that all 144 turns are concentrated at the midpoint of the cylindrical coil and have the same mean radius. This simplifying assumption results in an analytical solution, which can be expressed as follows:

$$\frac{\partial B_x}{\partial x} = \frac{3\mu_0 I N R^2 d}{2(R^2 + d^2/4)^{(5/2)}} \tag{3.1}$$

where R is a mean radius, I is a current, N is a number of turns, and d is a distance between coils. The result of analytical approximation for $0.3\,\text{A}$ was $1.49\,\text{G/cm}$ that was later confirmed by measuring the magnetic field gradient after construction. The actual magnetic field gradient was measured by moving the magnetometer along the axis of MOT coils. Initially the

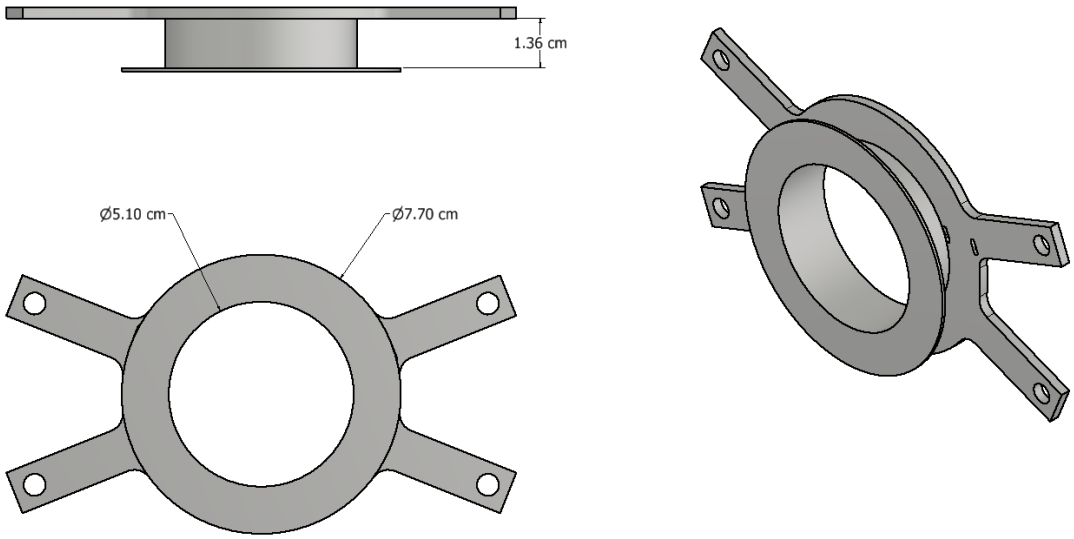

Figure 3.10: CAD drawing of an aluminum MOT coil winding structure.

magnetometer was placed with the sensor right at the center between MOT coils by zeroing the effect of coils' magnetic field. The results are shown in the table 3.3

X (mm)	MOT ON (mV)	MOT OFF (mV)	B (mG)	$\frac{\partial B}{\partial x}$ (G/cm)
4.75	625	625	0	1.44
5.25	769	625	72	1.46
5.75	915	625	145	1.46
6.25	1061	625	218	-

Table 3.3: Magnetic field gradient measurement was carried by observing differential measurement between MOT coils on and off states to calculate the Magnetic field gradient generated by MOT coils. The current in MOT coils was set to $0.3\,\mathrm{A}$

We adopted the current driver design that was developed for magnetic field compensation to build a voltage controlled MOT coils current driver. The schematic is shown in figure 3.11. The design allows for manual current adjustment through the use of a trimpot to set the V offset. It also includes a fine adjustment of the V_{const} that allows zeroing the magnetic field gradient at the MOT coils off state. We found out that due to some voltage offsets, the off state does not result in zero current. The feedback in off state was stabilizing the current to $5\,\mathrm{mA}$ instead of zero. Fine tuning of the constant offset was done by connecting an ammeter in series with the MOT coils and zeroing the current. Digital switch allows fast switching the control voltage from setting the current to zero or to the set values required for trapping the atoms. We implemented same protective diodes design as in magnetic field compensation to prevent damage from flyback voltage.

The response times of the MOT current driver are shown in the figure 3.12. It takes about $6.7\,\mathrm{ms}$ to turn on and $2\,\mathrm{ms}$ to turn off the MOT current. The slight instability during the turning on should not be a problem as we usually load the 3D MOT for several seconds. Obtaining a switching off that is fast and stable is very important as it can increase Eddy currents and hence increase the required waiting times than the current $8\,\mathrm{ms}$. The asymmetry of the feedback response might be due to the existence of protective diodes or the inductance

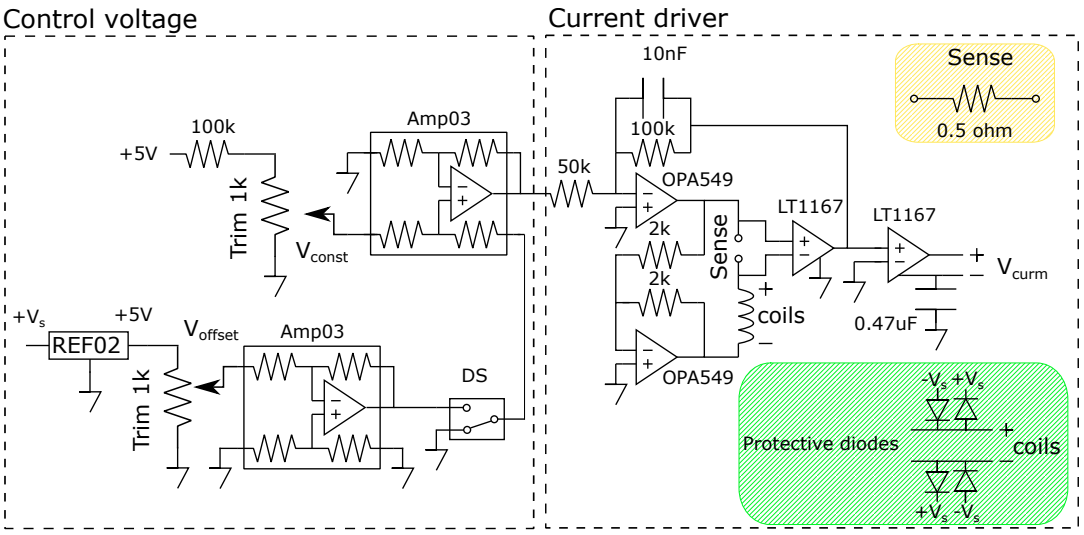

Figure 3.11: Schematic drawing of voltage controlled MOT current driver. Control voltage has an option of setting the V_{offset} with an onboard trimpot that will define the MOT current in the on state as well as V_{const} that is fine tuned to make sure that the off state is stabilized at $0\,\text{A}$. The current driver part is adopted from the magnetic field compensation design. DS is a digital switch that is controlled externally to turn MOT coils current on and off by connecting or grounding the reference pin of the Amp03.

of the MOT coils. In our setup the circuit is in a symmetric pull-push configuration and the power supply is symmetric as well.

The printed circuit board (PCB) was designed with the wider trace width of $2\,\text{mm}$ for every current carrying track in order to prevent them from overhearing. We used DigiKey's online trace width calculator using temperature rise of $8\,^{\circ}\text{C}$, current of $6\,\text{A}$, and thickness of $2\,\text{oz}/\text{ft}^2$, with a track being at the surface of the PCB. Additionally, we placed the MOT current driver box right behind the power supply fan. As a result, the heat sink of the MOT current driver was only slightly warmer than the room temperature.

The operation of the MOT coils usually restricts the placement of the magnetometer in the close vicinity as it interferes with the external magnetic field measurements and in our case saturates the magnetometer. In order to allow two competing feedback systems at the same time without interfering with each other, we implemented a compensation coil that cancels the magnetic field generated by MOT coils. The compensation coil is wired in series with MOT coils to counterbalance the magnetic field seen by magnetometer for any current applied. It is possible due to the linear relationship between magnetic field strength and current. In other words, regardless of the current driven through the MOT coils, the compensation coil completely shields its effects on the magnetometer while not perturbing the magnetic field gradient due to its distance to the location of the atoms.

3.5.1 MOT compensation coil

We have measured that $0.3\,\text{A}$ applied on MOT coils was generating about $90\,\text{mG}$ in vertical direction at the location of magnetometer. The calculation of number of turns and dimensions for the compensation coil, required to counteract the influence of the MOT coils, was performed using the same approximations as those applied in equation 3.1. Analytical result is expressed as follows:

Figure 3.12: Traces of the MOT coil current monitor. The response times are indicated in yellow boxes. Left picture shows the response of turning the MOT current on. It takes about $6.7\,\text{ms}$ to turn on with a little transient instability. Right picture shows the response of turning the MOT current off. It takes about $2\,\text{ms}$ to turn off with no transient instability.

$$B_{\text{comp}} = \frac{\mu_0 I N R^2}{2(R^2 + d^2)^{3/2}}$$

where R is a radius of the compensation coil, I is a current, N is a number of turns, and d is a distance from the compensation coil to the magnetometer sensor. Since we wanted to fix the compensation coil on the magnetometer, the diameter of the coil was chosen to be slightly larger than the diagonal of the magnetometer. The distance was chosen to be maximum allowed by the length of the magnetometer case, to enable more precise positional adjustments, recall the decay of magnetic field gradients from a current loop. The results of calculations given all design constraints was 20 turns with radius of $6\,\text{cm}$ and distance of $6\,\text{cm}$. We designed and installed a plastic compensation coil holder that allowed us to fix the compensation coil on a magnetometer and cancel the effect of MOT coils to below the resolution of magnetometer. In other words, we could not see any effect of turning on and off the MOT coils on the magnetometer output. Compensation coil holder as well as set screw were made of plastic to avoid unnecessary sources of magnetic field in the vicinity of the magnetometer.

The alignment of magnetometer required a lot of attention and care as we needed to position the magnetometer along the symmetry axis of MOT coils and rotate it to align with the direction of the bias fields to reduce the cross talk. In order to orient the magnetometer with the bias field direction we induced large bias field in one direction and oriented the magnetometer until it would not have any contribution to the orthogonal projection by turning that bias field on and off. After that the bias field was turned off and the location of magnetometer was adjusted to reduce the effects of MOT coils by turning them on and off. In addition, the distance of the compensation coil needs to be adjusted and it also alters the previous alignments. After multiple iterations we were able to decouple the orthogonal projections and decrease the effects of the MOT coils in all three directions to below the magnetometer resolution.

Implemented compensation coil design enabled continuous magnetic field compensation close to the location of the atoms by effectively shielding the magnetometer from MOT coils. Continuous active magnetic field compensation helped suppressing the lower frequency components of the Eddy currents when MOT coils are turned off.

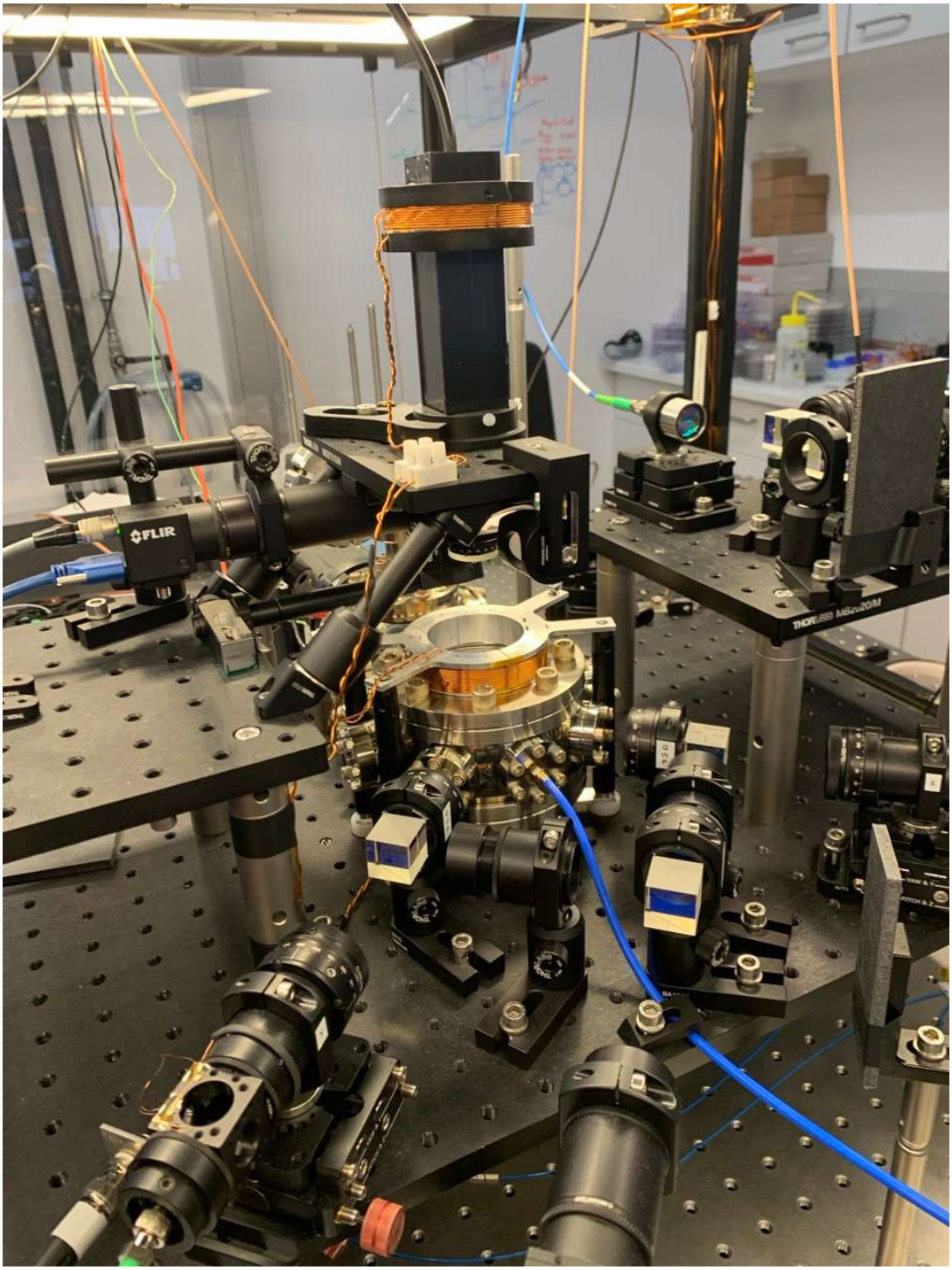

Figure 3.13: Image of the compensation coil installed on the magnetometer winded on a plastic coil and fixed with a plastic screw. It is connected in series with the MOT coils and used to shield the effect of the MOT coils on the magnetometer. Magnetometer is clamped on the plate with a home made plastic clamp.

3.6 Light generation

Multiple lasers with various stability criteria and wavelengths are required to manipulate the atomic cloud in cold atoms experiments. Our laser system consists of multiple $780.2\,\text{nm}$ Sacher external cavity diode lasers (ECDLs) with linewidth of $100\,\text{kHz}$ and maximum output powers of $100\,\text{mW}$ that are used as a reference, cooling, repump and two distributed feedback (DFB) Eagleyard lasers that are injection locked to be used as Raman beams. We also have a Herz-level stability $1560\,\text{nm}$ OEWAVES laser used as a dipole trap and also its frequency doubled fractions are used to injection lock the Raman lasers. Finally, we have the Rock OEM module from NP Phonotics with $1527\,\text{nm}$ wavelength and $700\,\text{Hz}$ linewidth to be used as an AC Stark shift compensation.

In this section I will describe the general arrangement of the optical components and their relation to each other. Then the parameters of each laser source and their application with some implementation details will be presented.

3.6.1 Arrangement

Our lab has two optical tables: one devoted to light generation and the other for delivering light to the atoms. The light generation table includes everything needed to prepare the light for delivery. Some of the larger projects on the light generation table involve frequency offset locking, modulation transfer spectroscopy, injection locking, singe side band modulation, power amplification, distribution and mixing together with AOMs. The motivation was to use everything possible on the light generation table and keep the other table as clean as possible. The reason is that the coupling to the science cavity and reflections from it are very sensitive and time consuming to recouple. The general description of lasers arrangement and their relation to each other is shown in figure 3.14 and figure 3.20.

3.6.2 Reference Laser

One of the Sacher lasers is locked to the ^{85}Rb $|F = 3\rangle \rightarrow |F' = 4\rangle$ transition (see figure 3.15) by modulation transfer spectroscopy [MKC08] is used as a reference laser. All other lasers are frequency offset locked with respect to the reference laser, and hence, are stable with respect to the atomic transition. Frequency offset locking of Sacher and Eagleyard lasers was done by our standardized feedback circuit with a bandwidth of $100\,\text{kHz}$. This frequency offset locking method that we developed will be described in detail in section 4.1. The low noise OEWAVES laser was stabilized only at several Herz level to avoid imprinting the noise of the reference laser and compensate only for slow frequency drifts.

3.6.3 Cooling and repump lasers

Cooling laser addresses $|F = 2\rangle \rightarrow |F' = 3\rangle$ transition of ^{87}Rb. Repump laser addresses the $|F = 1\rangle \rightarrow |F' = 2\rangle$ transition of ^{87}Rb. Energy level scheme is shown in figure 3.16 for reference. Both lasers are frequency offset locked to the reference laser with a method described in details in section 4.1. By design the frequency offset lock introduces additional $22\,\text{MHz}$ frequency offset with a sign that depends on the polarity of the beat at the mixer. Also the AOMs used for power control introduce additional $80\,\text{MHz}$ frequency offset. More complication comes from the fact that the frequency difference can be positive as well as negative. After a long period of being locked the frequency of the beat might drift far away, making it challenging to identify whether the raw beat signal is positive or negative. It would

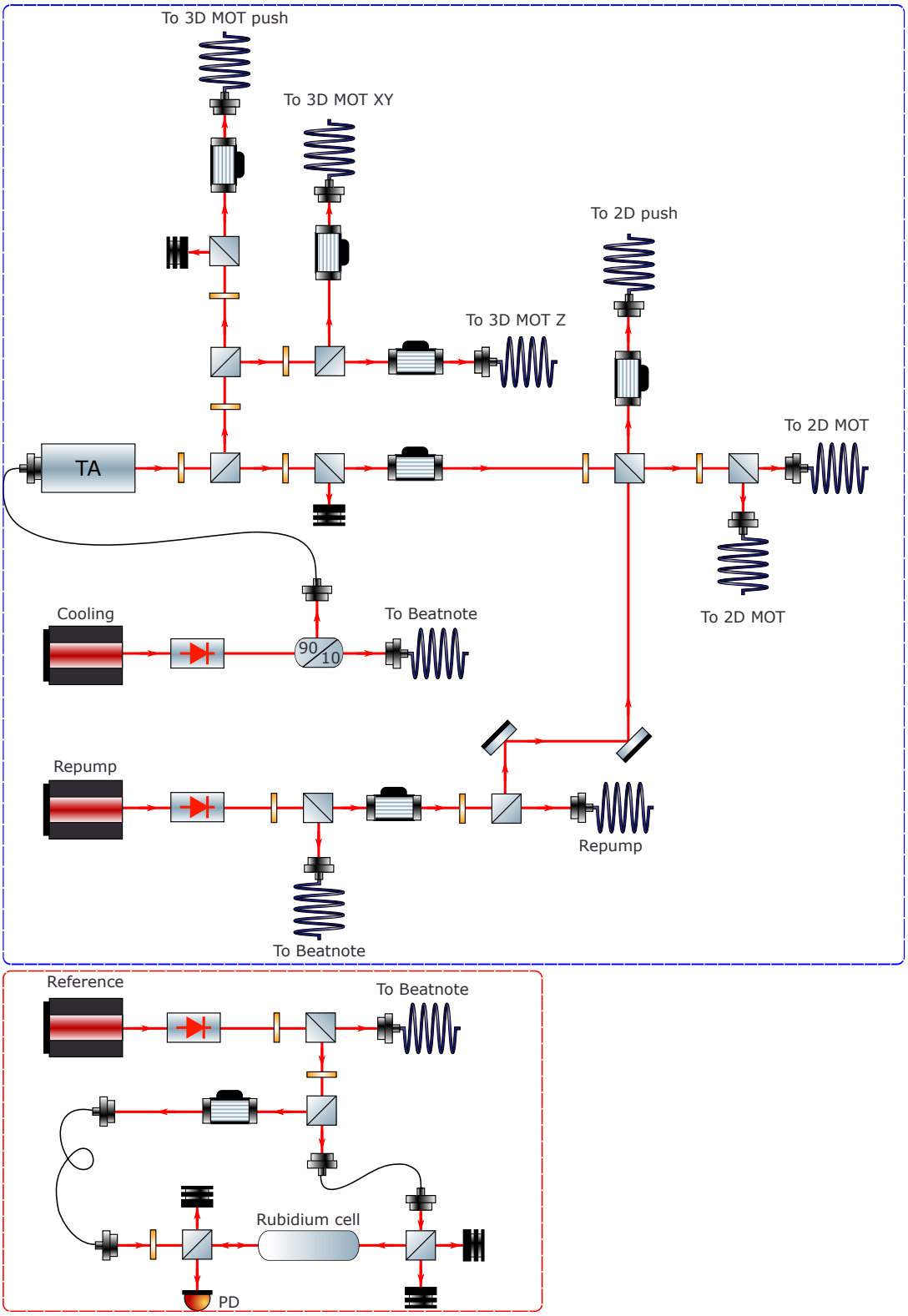

Figure 3.14: The schematic diagram is replicating actual arrangement of the components on the light generation table. Blue dashed line shows the generation of the cooling and repump lasers for 2D MOT and 3D MOT. Red dashed line shows the schematic of reference laser lock. TA is a tapered amplifier, PD is a photodetector.

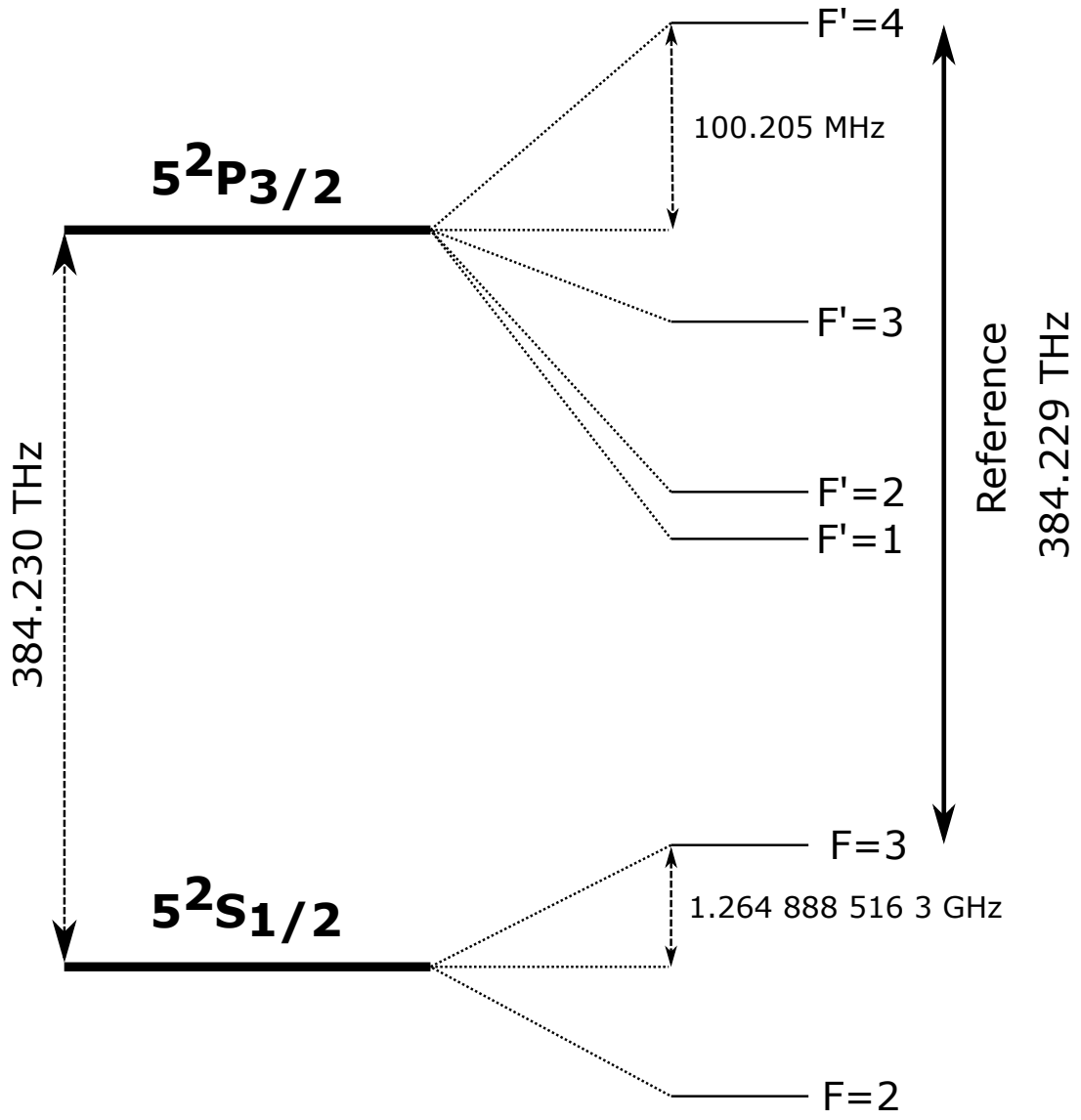

Figure 3.15: Energy level scheme for the D2 line of Rubidium 85

require using the wavemeter to coarsly tune the wavelength and then fine tune the raw beat and down-converted beats.

We realized that we can avoid using wavemeter by analyzing the frequency difference more carefully. Relative frequency offset can be observed at different stages of raw beat conversion. However, it is easier to analyze the down-converted beat that is used for locking. It can be written as follows:

$$\Delta = ||f_{\text{laser}} - f_{\text{reference}}| - f_{\text{LO}}|$$

where Δ is the down-converted beat frequency. The absolue value comes from the beat on the PD and down-convertion on the mixer. There are 4 possibilities that will result in the required Δ that corresponds to the zero of error signal. Let's consider two conditions when $f_{\text{reference}} > f_{\text{laser}}$ and $f_{\text{reference}} < f_{\text{laser}}$. For the first case the formula of down-converted beat frequency is

$$\Delta = |f_{\text{reference}} - (f_{\text{laser}} + f_{\text{LO}})|.$$

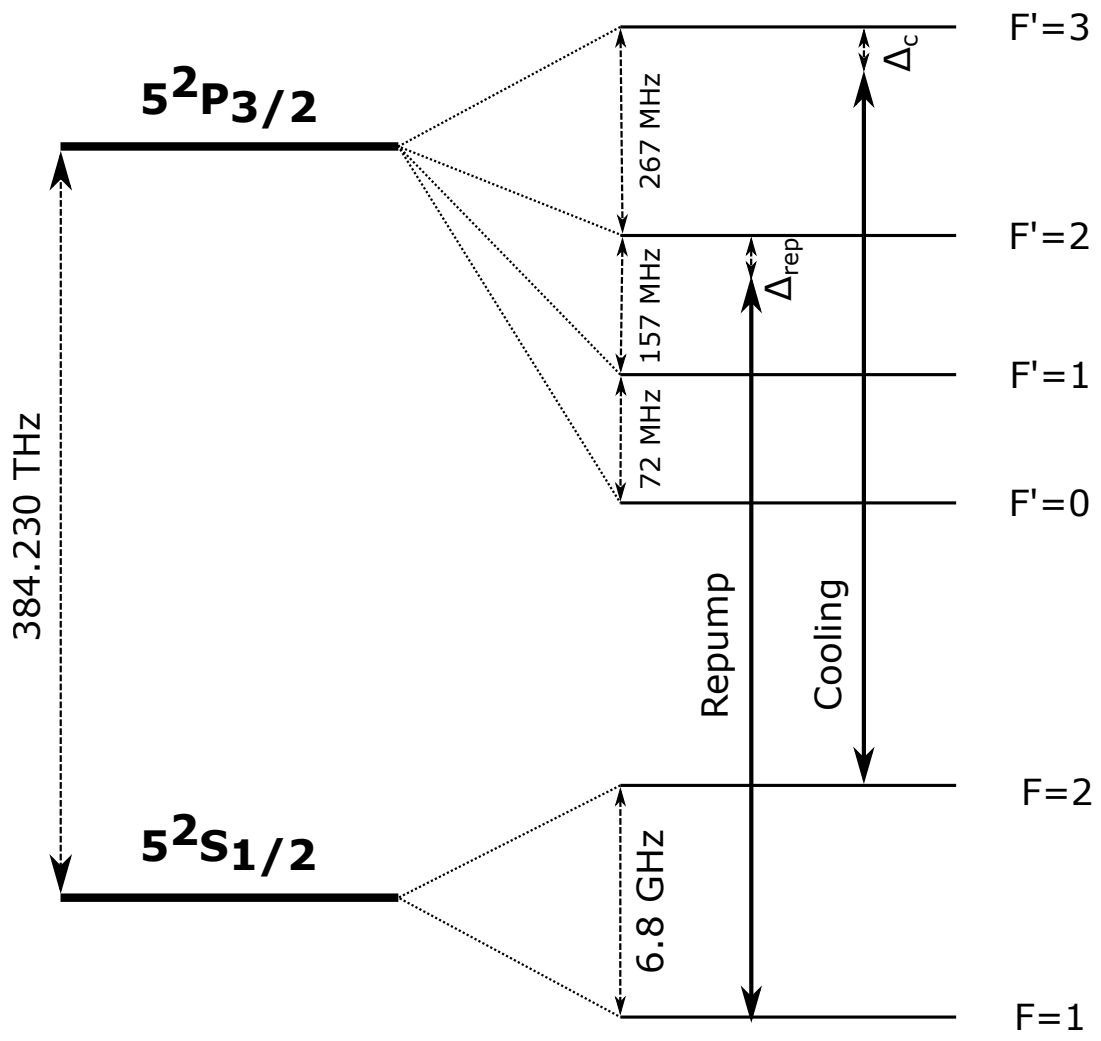

Figure 3.16: Energy level scheme for the D2 line of Rubidium 87

Recall that the feedback can only lock to the positive or negative slope of the error signal. In our case, it is the sign between Δ and f_{laser}. For example, let's assume that our feedback locks on the slope when increase of the laser frequency decreases the Δ. By being at the locking slope of the error signal, that can be checked by engaging the lock, we can lift that degeneracy. The most important point here is that the laser frequency and the local oscillator have the same sign. In other words, the increase of the local oscillator frequency will decrease the Δ. Now let's consider the second case.

$$\Delta = |f_{\text{reference}} + (f_{\text{laser}} - f_{\text{LO}})|$$

In this case the laser frequency and local oscillator have opposite signs. This means that the increase of the local oscillator frequency will increase the down-converted beat. Since the locking slope of the feedback does not change, we can characterize the response of the Δ on the increase of the local oscillator once and use that information later. In practice, we observe the down-converted beat on the spectrum analyzer. In our setup, at the locking side of the down-converted beat, increasing the local oscillator frequency moves the beat leftward for cooling and rightward for repump.

Alternative description of the aforementioned symmetry breaking is shown in figure 3.17. The red curves indicate the slope of the error signal. Let's assume that our feedback locks at

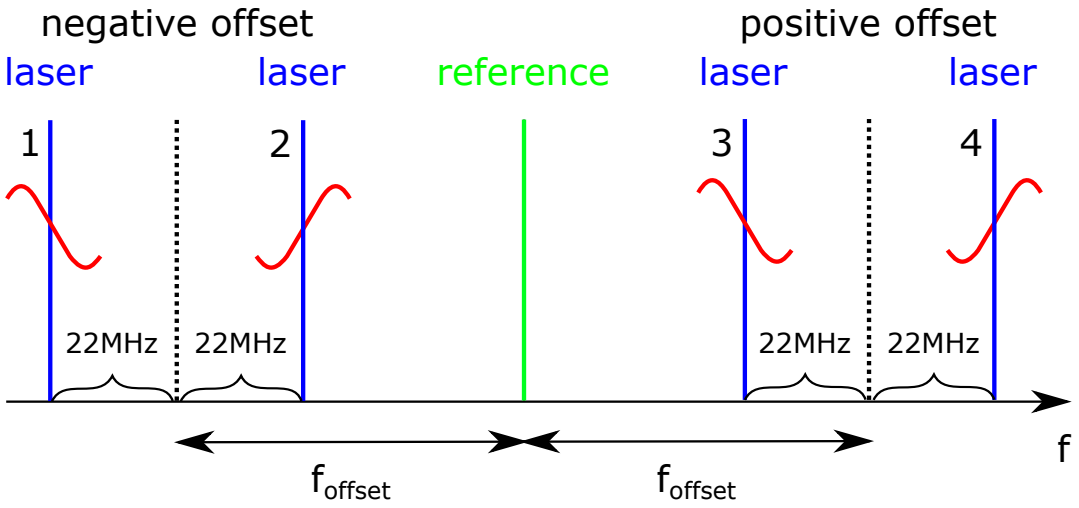

Figure 3.17: Schematic illustration of the locking laser and reference laser frequencies. Green solid line is the frequency of the reference laser. Blue solid lines indicate the locking laser frequencies at the locations of zero error signal. Red solid lines indicate the slope of the error signal at 4 potential locking points. f_{offset} is the frequency of the local oscillator that mainly defines the frequency offset together with the $22\,\text{MHz}$ due to the frequency discriminator. Black dashed line shows the frequency of the laser in case we would be able to lock it without introducing $22\,\text{MHz}$ offset, for illustrative reasons. Negative offset region corresponds to the case when $f_{\text{reference}} > f_{\text{laser}}$ and positive offset to $f_{\text{reference}} < f_{\text{laser}}$.

negative slopes. Then there are two possible locking positions 1 and 3. If the laser frequency is smaller than the reference laser frequency the increase of the frequency offset will move the laser frequency to the left. In case of positive frequency offset it will move to the right.

Using the method described in this section one can lock to the correct frequency offset positive or negative by characterizing the direction of motion of the down-converted beat at the locking slope of the error signal. This saves a lot of time and lifts the need of using the wavemeter after initial characterization.

3.6.4 Frequency offset tuning

As was mentioned in the previous section, the frequency offset calculations might be quite challenging. Especially taking into account that the frequency multiplications and absolute value due to beating and mixing the signals complicate the calculations. In this section I will provide the practical guide on how we first fine tuned the frequency offsets and then optimized them for larger atom number loading in 3D MOT.

Initially we used a wavemeter to adjust wavelengths of each laser and then further tuned the frequency offset by observing the raw beat of reference and corresponding lasers at GHz level. Finer adjustment of the frequencies was done by observing their down-converted beat frequencies at MHz level. The wavelengths calculated from the energy level diagrams neglecting AOM and feedback lock induced offsets are shown below.

λ_{ref} (nm)	λ_{cool} (nm)	λ_{rep} (nm)
780.243	780.245	780.232

Table 3.4: Calculated wavelengths of reference, cooling and repump lasers.

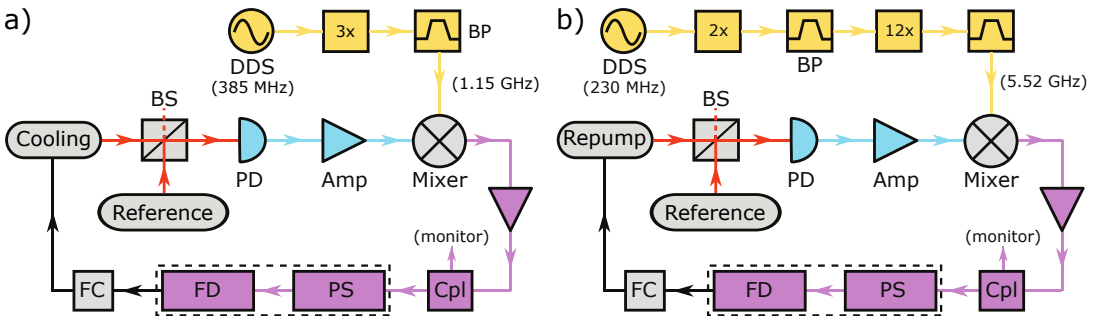

Figure 3.18: Schematics of cooling and repump lasers frequency offset locks are a) and b) respectively. The blue paths are showing the GHz raw beats. Yellow parts are RF generations of local oscillators used to down-convert the beat to MHz range. Purple paths indicate feedback paths that are used to frequency stabilize cooling and repump lasers with respect to the reference laser by modulating the corresponding lasers currents. Note that the DDS frequency values are approximate values that we used at the beginning.

The locking schematics for both cooling and repump lasers are shown in figure 3.18. Note that the frequency offsets applied from our experimental control system are frequency multiplied by 3 and 24 for cooling and repump lasers respectively. The values of $385\,\mathrm{MHz}$ and $230\,\mathrm{MHz}$ are some starting points approximately derived from the expected frequency offsets between the reference laser and corresponding transitions. The actual values were first coarsely optimized by observing the fluorescence of the 2D MOT filament. After that we were able to observe the atoms in the 3D MOT. We optimized the frequency offset at the input of the local oscillator of the cooling beam to increase the atom number at fixed $5\,\mathrm{s}$ loading times. The results are shown partially in figure 3.19. More precise measurements of 10 times averaged frequency scan for cooling, repump as well as for maximizing the fluorescence resulted in the following optimal values shown in the table 3.5.

The optimal detunings of cooling and repump for 2D MOT and 3D MOT are different. Ideally one needs to optimize them separately. However, the current state of the laser distribution does not allow independent tunability of the frequencies for 2D MOT and 3D MOT. There is a room for optimization of laser frequency offsets. However, in the spirit of producing

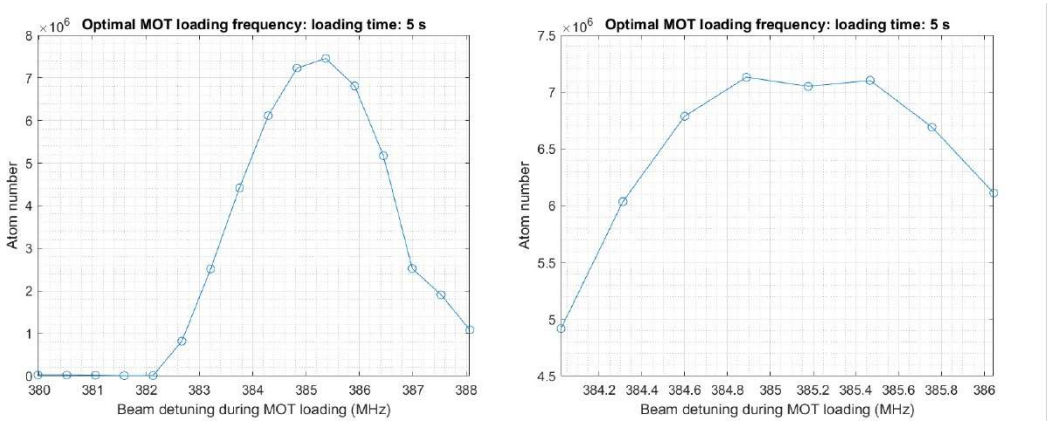

Figure 3.19: Optimization of the cooling beam frequency offset. Left plot shows the broader scan. Right plot shows more precise scan. Both plots were made by taking a single measurement for each frequency. This image is shown for illustrative purpose. More precise measurement of 10 data points per frequency gave optimal frequency offset of $385.25\,\mathrm{MHz}$

Cooling (MHz)	Repump (MHz)	Fluorescence (MHz)
385.25	226.05	382.0

Table 3.5: Impirically optimized cooling, repump and fluorescence frequency offsets from experimental control system. Cooling laser was tuned near the resonance fluorescence frequency to perform imaging.

experimental results, the current optimization was more that sufficient to proceed with the next steps.

3.6.5 Raman beams and dipole trap lasers

This section will describe the optical arrangement to generate the dipole trap laser and Raman beams. The 1560 nm OEWAVES laser is used as a dipole trap. Some portions of the same laser are frequency shifted by an single sideband modulator (SSB) and frequency doubled to injection lock two DFB 780 nm Eagleyard lasers that are used as Raman beams.

Initially the output of the OEWAVES laser is split into two paths. First path is amplified and split into two again. One part is frequency shifted by 'SSB2' to frequency match the dipole trap laser and Raman beam 1, making them both resonant with the cavity. Then it is transferred to another table and used as a dipole trap. Another path is frequency doubled at '2xf' and used to injection lock the Sacher 780 nm laser that is used as Raman 1. Raman 1 is then split into two. One part goes to the light delivery table and then to the science cavity. Another part is being used to frequency offset lock 1560 nm OEWAVES laser very slowly to the reference laser, by beating its frequency doubled portion and applying the feedback on the modulation port of the OEWAVES laser. This slow lock ensures that the 1560 nm laser is stable with respect to the atomic transition. Second path is frequency shifted via 'SSB1' by 6.8 GHz with respect to the Raman 1. It is then split again with a 90/10 fiber splitter with 90% going into the Fabry Perot spectrometer and photodetector (PD) that is used for troubleshooting and 'SSB1' locking. 10% is then amplified and frequency doubled to be used for injection locking of Raman 2 laser.

Note that it was important to amplify the laser signal before implementing the SSB2 as erbium-doped fiber amplifier (EDFA) efficiency is input power dependent. SSB2 serves the purpose of the frequency offset as well as the dipole trap power control. Dipole trap laser power at the input of the cavity as a function of the control voltage is shown in figure3.21. We need to be able to turn on and off the dipole trap on demand by using SSB2 dipole trap laser power control while preserving the laser to cavity lock. It requires the feedback stability for low and high input powers. In other words, low and high gain. Having non-linear control voltage to output power response might add complications for the feedback stability as its slope defines the overall gain.

3.6.6 Injection lock for Raman beams

The optimal current and temperature setting for the injection locked laser for proper injection depends on the injection laser frequency. Tuning the injection laser's frequency may disrupt injection locking. Even with a static injection locking frequency, the frequency of the injected laser may drift over time, ultimately leading to failure of injection locking. In both cases it can result in degradation of the injection and hence unexpected output of several spurious

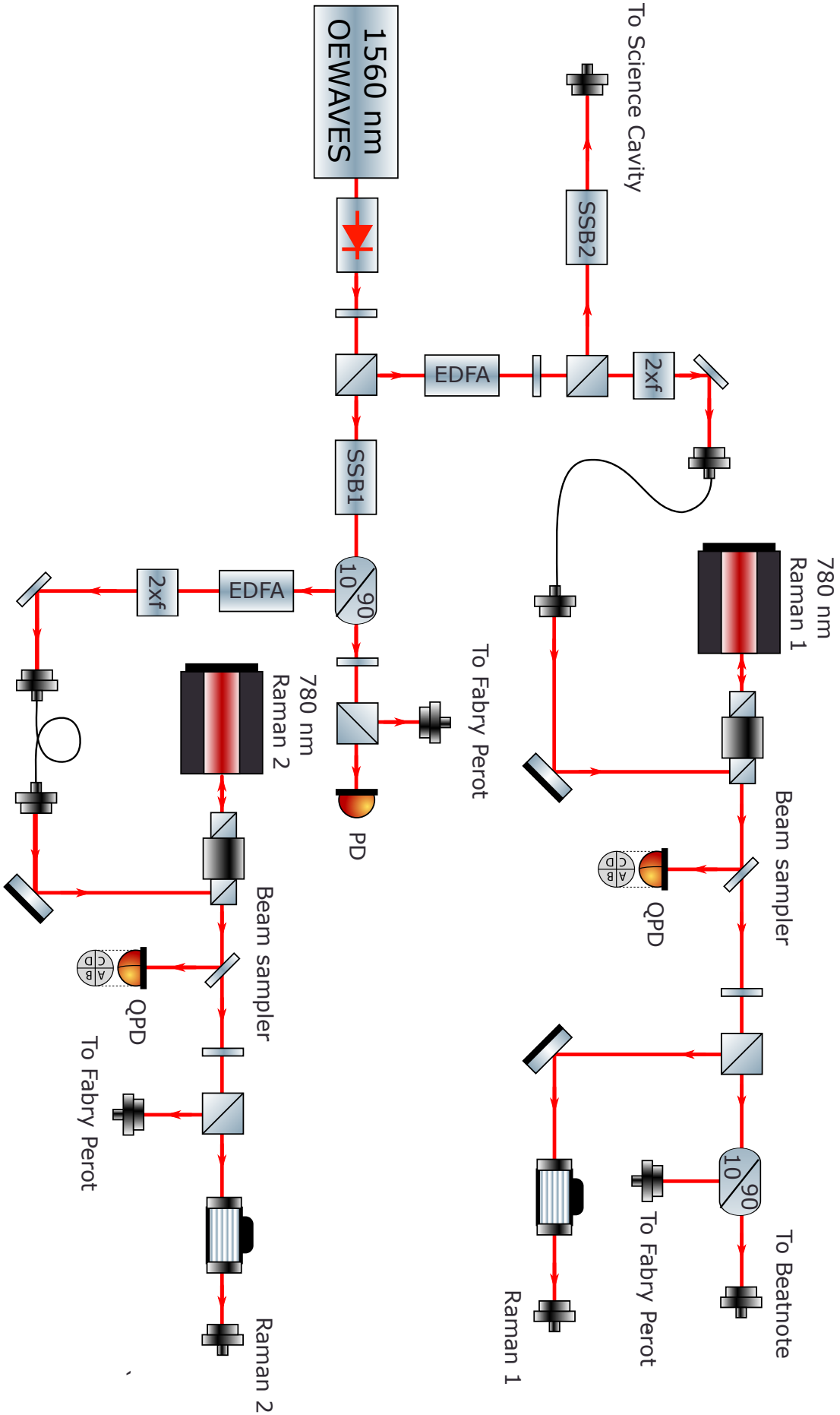

Figure 3.20: Optical arrangement of the Raman beams and dipole trap lasers generation. Schematic diagram does not represent the real components arrangement on the light generation table. It is shown here to represent the conceptual relation of lasers. Low noise 1560 nm laser is used as a dipole trap. Its frequency doubled and frequency shifted portions are used to injection lock 780 nm Sacher lasers that are used as Raman beams. Raman 1 is used in the frequency offset locking scheme to slowly lock the OEWAVES laser to the reference laser and hence keep it stable from drifts with respect to the atomic transition. 'SSB' refers to single sideband modulator. '2xf' is a frequency doubler. 'PD' is a photodetector. 'QPD' is a quadrant photodetector. 'EDFA' is erbium-doped fiber amplifier.

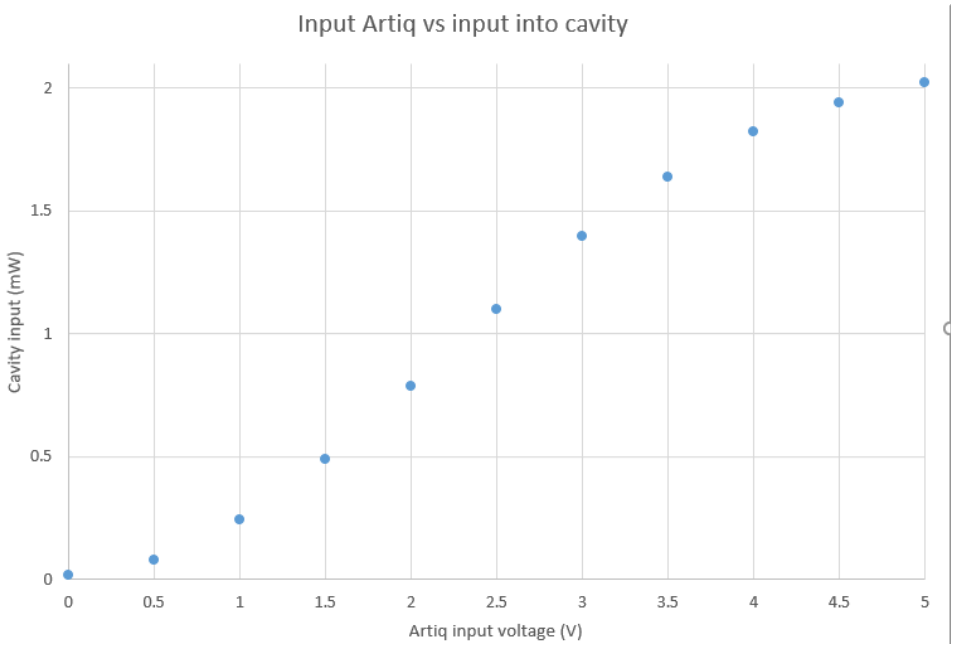

Figure 3.21: Dipole trap laser input power to the science cavity as a function of the voltage control applied to the SSB2. Note that the actual power might drift due to the coupling efficiency drifts. Current operation point is around 1 mW.

tones. To avoid such problems we developed a method for laser injection locking stabilization based on the variation of the beam ellipticity of an optically seeded laser. We found that the range of proper injection locking corresponds to specific beam ellipticity. By modulating the seeded laser's current, we can keep it withing the proper injection region. The error signal is observed on the quadrant photodetector (QPD) has a zero crossing, which is used to feedback on the injected laser current. Stabilizing the injection lock allows tunability of the injection laser frequency over 10 GHz range that is far beyond the requirements of our setup. For more details on injection locking please refer to our paper[MLW+23]

3.6.7 Stark shift compensation with 1527

Since the dipole trap itself introduces position dependent AC Stark shift, it is impossible to perform cooling inside of the dipole trap. We want to implement the compensation with 1527 nm laser as they have a good mode overlap with 1560 nm dipole trap laser. If AC Stark shift is efficiently eliminated, it will allow us to loose less atoms by cooling them inside of the dipole trap. In addition, this would lift the requirement of the cavity lock to remain stable at low dipole trap intensity and we could keep the dipole trap running in on state. However, this is an on-going work that is beyond the scope of this thesis.

3.7 Light delivery to the atoms

This section will describe the general arrangement of the optical components used to deliver light to the atoms. Following that, detailed description of the 3D MOT launchers and 3D MOT beam parameters will be presented.

3.7.1 Arrangement

An overview of the optical arrangement of the light delivery to the atoms is shown in figure 3.22. The schematic does not show the polarization adjustment of the 3D MOT beams. 3D MOT Z_{top}, 3D MOT Z_{bot}, repumper and 3D MOT push beams are also not shown to not complicate the description. Power distribution before connecting to the 3D MOT beams launchers is done on the light delivery to the atoms table by use of multiple 50/50 fiber beam splitters. Since there is only one AOM to control all 3D MOT X and Y beams there is an output power monitoring PD only on Y_{qwp}. Another power control option is available for 3D MOT Z beams with a power monitor on Z_{top} launcher.

3.7.2 3D MOT Launchers

The fiber docks for 3D MOT lasers are equipped with polarization cleaning PBS, $\lambda/4$ wave plates to generate required circular polarization, and iris diaphragms that allow decreasing the outcoupling beam size for better alignment. For X and Y launchers we distinguish between launchers with the PBS + waveplate on the launcher as X_{qwp} and Y_{qwp}, and placed separately from the launcher to allow XY imaging as described in section3.8. In addition, we have installed the micro-electromechanical (MEM) shutters right at the output of the fiber holder that can be used to physically block the light. It proved handy when aligning the 3D MOT, as we could turn on and off each launcher independently. Additionally, it offers slower but better isolation compared to faster AOM power control, which can suffer from residual light leakage when AOMs are in the off state.

3.7.3 3D MOT beams parameters

The beam sizes were expanded by using the telescopes integrated into the launchers to about a $1\,$mm size when observed by eye on the fluorescence card. The actual $1/e^2$ beam size was measured to be $3.98\,$mm using the edge knife technique by sliding the razor blade with a micrometer and measuring the transmitted power. We used this information to calculate the required beam intensities.

Efficient 3D MOT trapping and cooling requires specific orientation of the magnetic fields and polarizations of the 3D MOT beams. Schematic diagram outlining the working mechanism of the 3D MOT and the direction of the circular polarizations is shown in figure 3.24. Details about operating principles of a MOT can be found in [MvdS99] or [AR97].

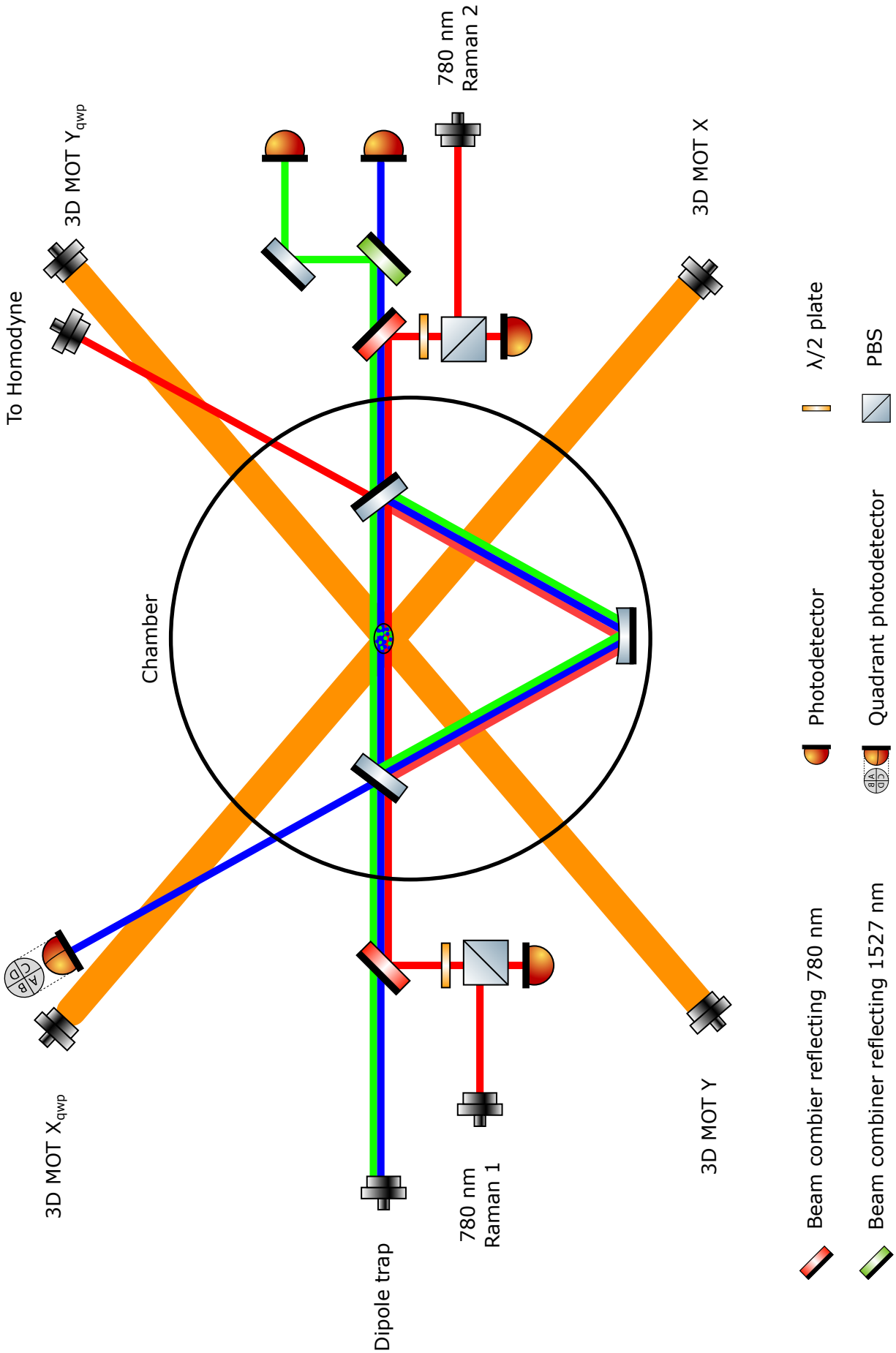

Figure 3.22: Schematic drawing of the light delivery to the atoms. Blue solid lines indicate the propagation of $1560\,\text{nm}$ laser. Red solid lines indicate the propagation of $780\,\text{nm}$ laser. Green solid lines indicate the intended propagation of $1527\,\text{nm}$ laser. Orange solid lines indicate the propagation of 3D MOT cooling lasers.

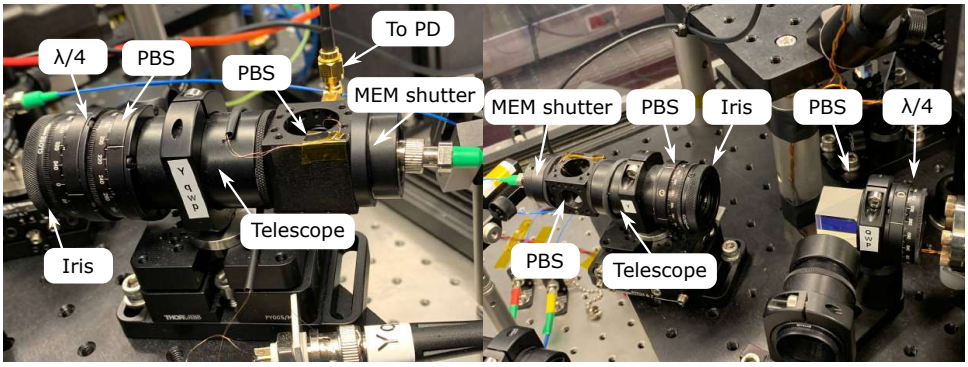

Figure 3.23: Images of 3D MOT launchers. Left image is the Y_{qwp} launcher with the quarter wave plate attached to the launcher. Right image is the Y launcher with the PBS and wave plate not connected to the launcher. Telescope is used to increase the beam size.

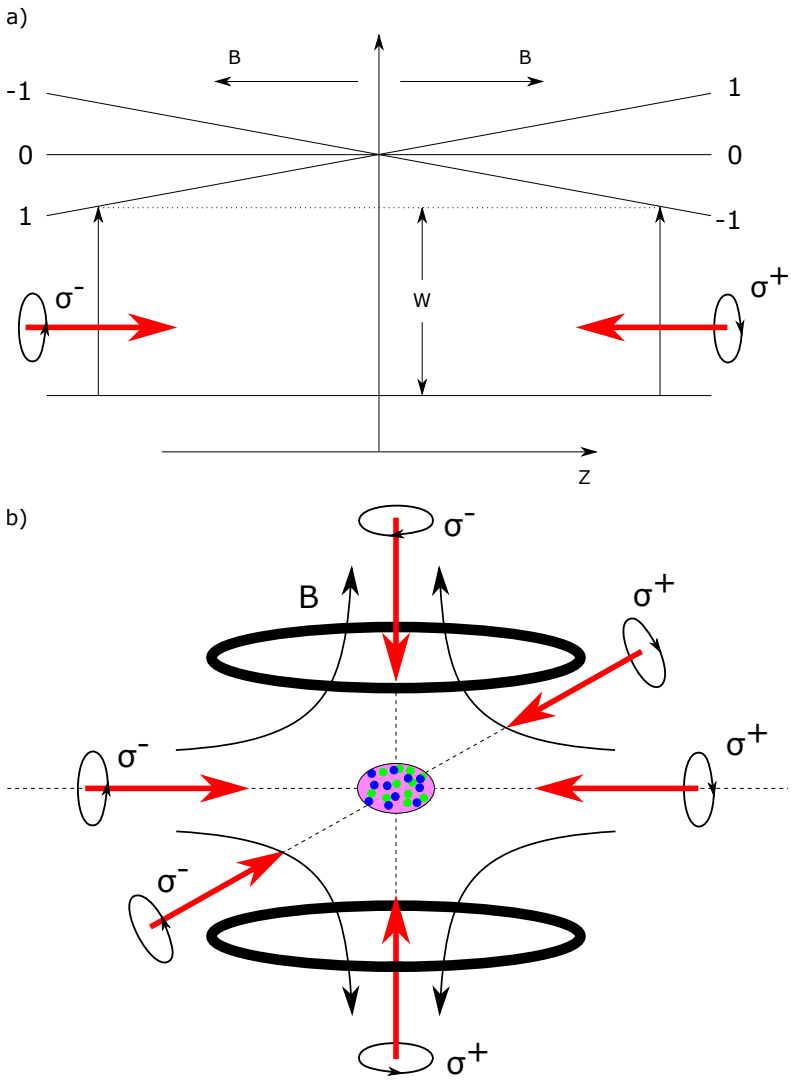

Figure 3.24: a) Illustration of the 3D MOT working principle. Depending on the atom location the light becomes resonant and applies force towards the center of magnetic field zero. b) Schematic diagram showing the polarization of the 3D MOT beams for trapping the atoms. Solid red lines indicate the direction of MOT beams propagation. Solid black lines indicate the direction of magnetic field.

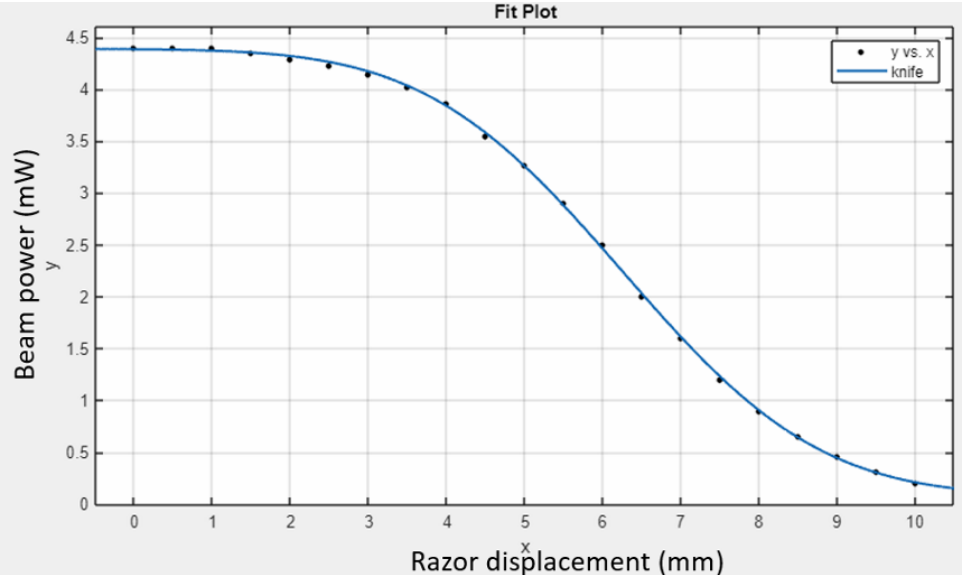

Figure 3.25: The results of the knife edge technique for beam profile measurement.

3.8 Imaging system

In our experiment we use the fluorescence imaging to align the 3D MOT by inspecting the quality of the 3D MOT, measure the temperature using time of flight expansion, and count the number of atoms. For all aforementioned applications we use the 3D MOT cooling beams tuned near the resonance and 3D MOT repump. The light scattered from the atoms is captured on the CMOS Flir Blackfly BFS-U3-32S4M cameras. Camera characteristics from the data sheet is shown in the table below.

Pixel size	$3.45\,\mu$m
Quantum efficiency at $780\,$nm	35%
Gain	0.18 e^-/ADU
Trigger latency	$6\,\mu$s

Table 3.6: Characteristics of the Flir Blackfly BFS-U3-32S4M camera used for imaging in our setup.

However, the camera trigger delay was measured to be $20\,\mu$s instead of the expected $6\,\mu$s. We chose not to investigate the source of the discrepancy as it did not affect the final results. We only needed to account for the actual delay. To ensure proper exposure, we used our control system to precisely control the duration the repump and cooling beams were turned on. To duarantee the shutter is fully open when the lights turn on and remains open for the entrire illumination period, the trigger signal needs to be sent slightly earlier. Consequently, the camera exposure time must be set slightly longer than the intended exposure time to compensate for these delays.

Due to the absence of anti-reflective coating on the top and bottom view ports we decided to take the background image to subtract the light scattered from them. We also decreased the scattering by taping the gap between the first lens and the telescope tube. The camera telescope has a $10\,$nm notch filter with the central frequency of $780\,$nm. As a result, the system was insensitive to the largest ambient light source from the table rack.

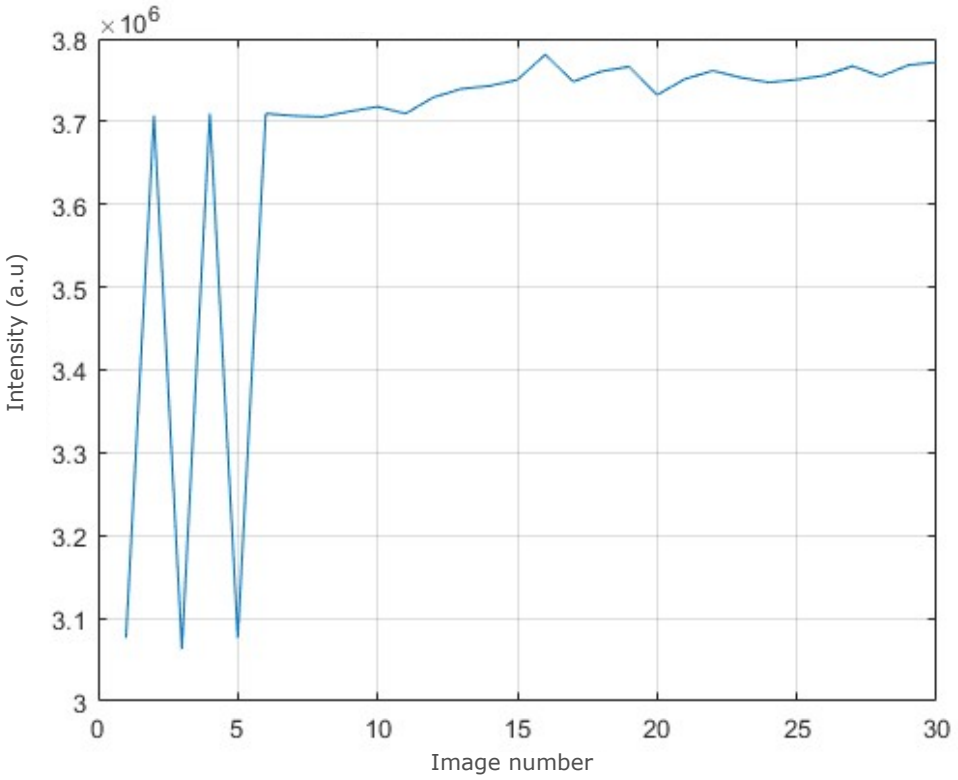

Figure 3.26: Observed unexpected atom number drops in the beginning of the experimental sequence. After taking 10 images at the beginning of each experiment and then discarding them no more atom drops were observed.

We observed that the cameras occasionally fail to capture all light from the atoms. There were unexpected dips in the atom number as shown in figure 3.26. After changing the initial states and varying the timing between images, we concluded that the effect is independent of the initial configurations and experimental procedures. However, it only appears at the beginning of the acquisition program. If we start the acquisition program and then run several experiments, only the first several images show unexpected behavior. The problem was resolved by triggering the camera 10 times at the beginning of a new acquisition and then discarding those images from analysis.

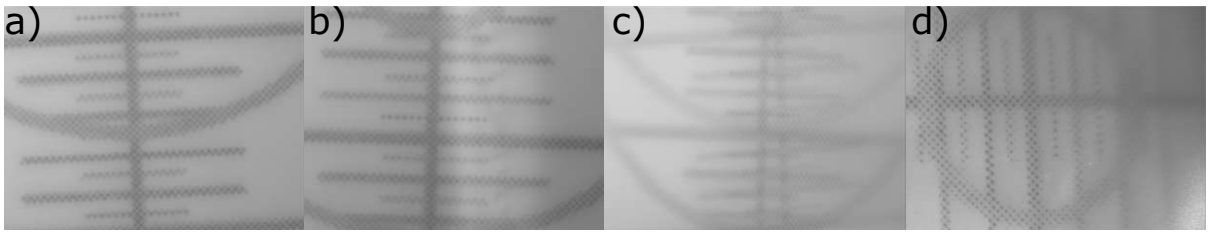

Figure 3.27: Demonstration of target images used to adjust the alignment and focus of Z and XY imaging systems. a) is X image when Y is blocked. b) is Y image when X is blocked. c) is XY image when nothing is blocked. d) is Z image. X and Y images were put close to each other in order to be able to observe longer time of flight expansion from X and Y by blocking Y and X respectively.

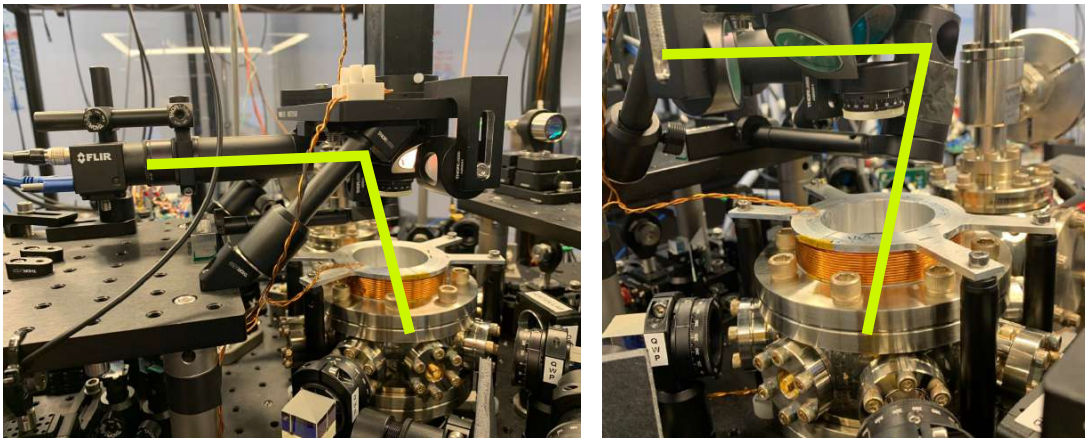

Figure 3.28: Z imaging system. Two views are shown for better understanding of the components arrangements. Light green line indicates the trajectory of the fluorescence being captured on the camera. The line indicates only direction. The divergence of the actual light is not taken into account.

We did not calibrate our imaging system. Its purpose was to inspect the shape of the cloud and infer the atom number. The latter is usually a significant approximation as it is challenging to measure solid angle and take into account all parameters for precise atom number calculation. Therefore, atom number calibration will be done later by calibrating the cavity resonance frequency shift due to the internal state of the atoms, as this method has better precision.

In our setup we have two cameras: top view that we call Z imaging and a side view that we call XY imaging. For XY imaging we combine views from both X and Y directions using optical elements to a single camera. Both views have a light collecting lens as close to the atoms as possible to collect as much light as possible. The telescope magnification is 1 and was designed to avoid any light loss by taking the lenses sizes and their mutual distances into account. Alignment of the imaging system and fine-tuning of the focusing was done in the absence of the vacuum chamber with a use of paper targets shown in figure 3.27. For XY view we decided to put both X and Y almost on top of each other since larger spacial separation would limit the time of flight expansion measurement. In most XY images, the two clouds are slightly separated. However, if they overlap, we block the beam path for one of them. This allows us to still observe the time of flight expansion of the X or Y view by blocking Y and X, respectively. XY imaging is then used for optimizing alignment and troubleshooting.

3.8.1 Z imaging

Z imaging is the top view on the atomic cloud as shown in the figure 3.28. The placement at an angle allows observation of the 3D MOT live. Imaging is done with all 3D MOT beams on and cooling laser frequency tuned near the resonance. Due to the imperfections of the alignment the expansion of the cloud during the exposure time can change the shape of the cloud as it is an expansion in molasses. Therefore, for applications that require less intrusive imaging, like time of flight, we decrease the exposure times to 0.1 ms and detune the 3D MOT beams from the resonance by 6 MHz. This allows less distortion of the cloud shape at the expense of lower signal to noise ratio. However, this did not affect the Gaussian fits quality.

When working with 3D MOT it is important to know the relative projections of the magnetic field and cooling lasers when observed from the Z camera. For reference, they are shown in the figure 3.29.

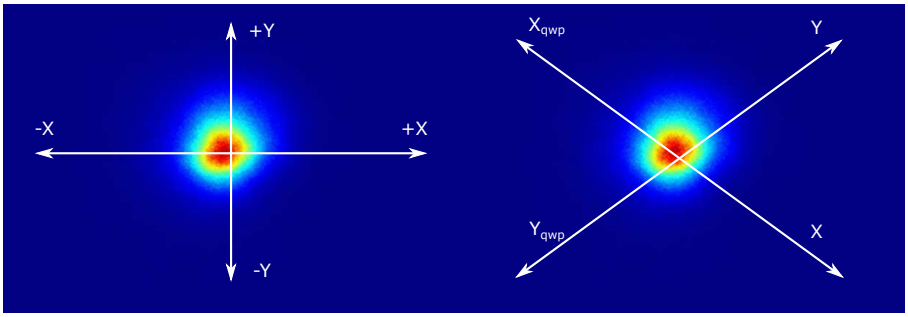

Figure 3.29: Left image shows the projections of the magnetic field on the Z camera view. Right image shows the location of corresponding 3D MOT launchers when observed from Z camera.

3.8.2 XY imaging

XY imaging is the side view on the atomic cloud as shown in figure 3.30. It is a combined view of the cloud from two perpendicular projections X and Y. Due to the finite sizes of the view ports the placement of the XY camera was not possible without 3D MOT beams also hitting it. Therefore, the XY imaging was done with only 3D MOT Z beams ON. It is mainly used for alignment purpose. Vertical misalignments lead to the cloud being stretched along Z direction that was not visible when observed from the top. An example of such misalignment viewed from X is shown in figure3.31. The presence of distortion that can be seen only from X or Y helped improving alignment and balancing 3D MOT beams power seen by the atoms. Better alignment and power balance decreases the atom loss during the cooling procedure and also helps decreasing distortions from 3D MOT beams during fluorescence imaging. Ideally the expansion of the cloud inside of molasses should be just slowed down version of free expansion. However, we could not align the 3D MOT to the state when the cloud does expand symmetrically in the full power molasses. We assume that it was due to slightly different locations of the cloud when it is rather small and most probably coincides with the location of the zero magnetic field and the alignment of the 3D MOT beams.

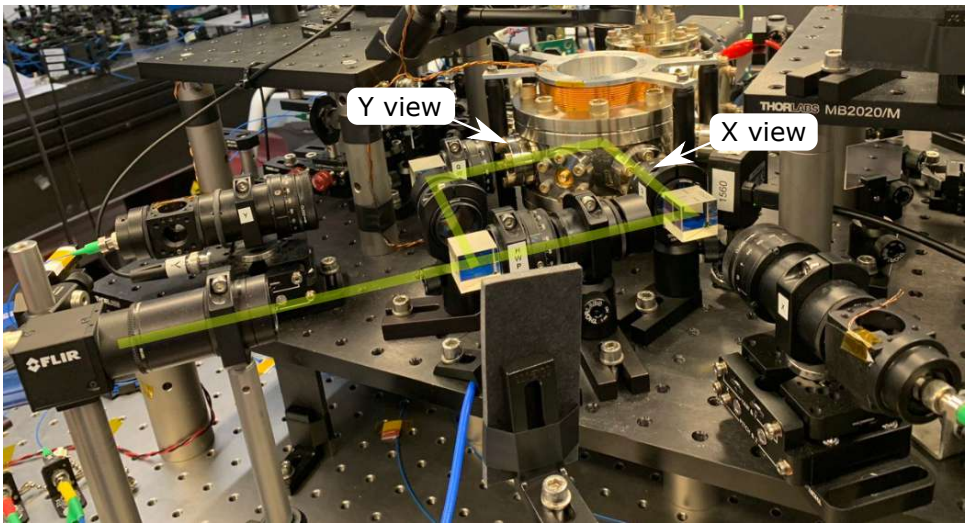

Figure 3.30: XY imaging system arrangement. Light green line indicates the trajectory of the fluorescence being captured on the camera. The line indicates only direction. The divergence of the actual light is not taken into account. XY view includes both X and Y images on the same camera.

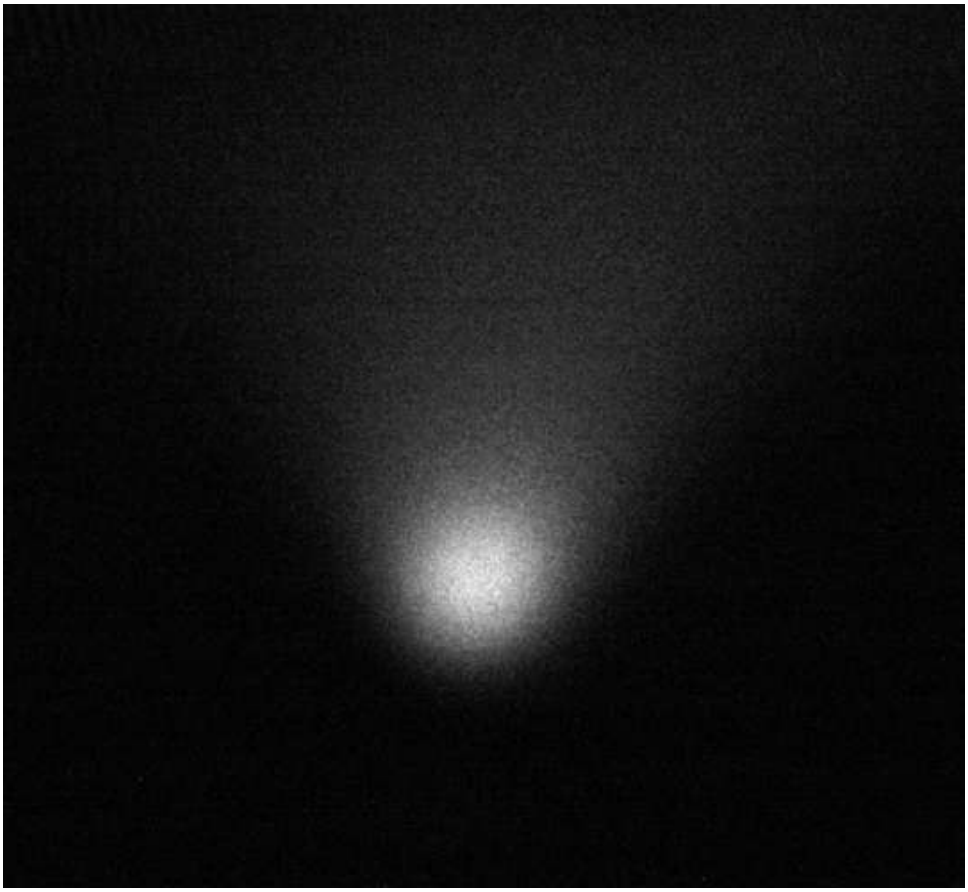

Figure 3.31: Image of the cloud from X view. Vertical streaks indicate that there is either a power imbalance or misalignment of the 3D MOT beams. Using X view helped eliminating the streaks and hence improving the alignment and effective power balance of 3D MOT beams seen by the atoms.

3.8.3 Atom number calculation

Atom number calculations were performed on the images from Z camera since it had only one cloud and had better signal to noise ratio. It was calculated using the scattering rate from [Ste03] given by

$$N_{\text{atoms}} = \frac{8\pi[1 + 4(\Delta/\Gamma) + (6I_0/I_{\text{sat}})]}{\Gamma(6I_0/I_{\text{sat}})t_{\text{exp}}\eta_{\text{count}}d\Omega} N_{\text{counts}}$$

where I_0 is the intensity of one of the 3D MOT beams, I_{sat} is the saturation intensity, N_{counts} is the total number of counts integrated over all pixels, t_{exp} is the exposure time of the camera, η_{count} is the quantum efficiency of the camera, and $d\Omega$ is the solid angle of the light collected by the camera. Solid angle was calculated from the expression given by

$$d\Omega = \frac{\pi}{4}\left(\frac{f}{(f/\#)d_0}\right)^2$$

where f is the focal length of the collecting lens, d_0 is the distance from the source to the lens, and $f/\#$ is the f-number of the imaging system.

Parameters used for atom number calculation are shown in the table below.

Γ (MHz)	$2\pi \cdot 6.065$
Δ (Γ)	1
I_0 (mW/cm^2)	5.47
I_{sat} (mW/cm^2)	1.67
t_{exp} (µs)	100
f (mm)	60
d_0 (mm)	75
# (mm)	25
η_{count}	0.35

Table 3.7: Parameters used for atom number calculation. Z imaging was used for the atom number calculations.

3.8.4 Time of flight

The temperature of the cold atomic clouds can be inferred from the rate of its free expansion. Assuming isotropic velocity distribution, the standard deviation of the spatial distribution [Hru18] can be defined as following:

$$\sigma_i^2(t) = \sigma_i^2(0) + \frac{k_B T_i}{m} t^2$$

where i corresponds to either vertically or horizontally integrated projection of Gaussian, k_B is a Bolzmann's constant, m is the mass of rubidium atom, T_i is a temperature inferred from the i-th projection of the fit, and t is the time of expansion. The formula provided above ignores the effects of the gravitational fields. Therefore we used the Z view to perform the temperature measurements as it has less gravitational effect and larger signal to noise ratio due to stronger fluorescence signal. Example of the cloud expansion after far detuned cooling is shown in figure 3.32.

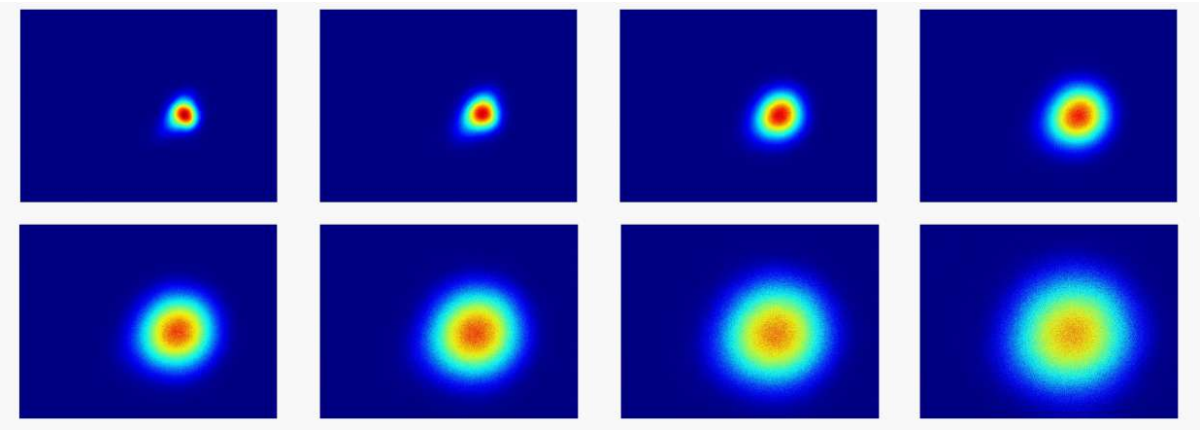

Figure 3.32: Example of the time of flight images after far detuned cooling. Each image is 1 ms apart from left to right and continues consequently on the bottom row with the last bottom right image corresponding to 8 ms TOF.

CHAPTER 4

Making it all work

4.1 Frequency offset locking

Following section will describe the frequency offset locking technique that we developed and are employing for locking the lasers at a variable frequency offset with respect to the reference laser. The section is heavily based on our paper[LDH22].

4.1.1 Introduction

The ability to generate laser beams with well controlled and stable relative frequencies enables applications in many scientific and technological areas. Precision optical metrology using optical frequency combs [UHH02], laser cooling and trapping of atoms [MvdS99], coherent manipulation of their internal [FIM05] as well as their motional degrees of freedom [KC91, HUV$^+$17], and coherent manipulation of solid-state quantum systems [STN$^+$06, BSD$^+$19] are examples relying on good relative frequency control. The capability of controlling such systems makes possible precision applications like atomic clocks [LBY$^+$15] and atom interferometers [TK14] for geodesy, inertial navigation and tests of fundamental physics [SHH21], and makes possible many quantum information processing applications.

A number of general techniques exist for generating laser tones with fixed relative frequencies. These include splitting a single laser beam and shifting its frequency with acousto-optic [BDB$^+$00] or electro-optic modulators (EOM) [JHCK10] – reaching offsets from tens of MHz to tens of GHz; locking separate lasers to different resonances of optical cavities [DGB92] or atomic systems [NHOW06, BHW$^+$07] – reaching from GHz to hundreds of THz; and directly stabilizing the frequency offset between lasers by utilizing the interference beat note between the optical tones on a photodetector – offering the largest range of applicability while keeping lasers spectrally pure. This last technique will form the basis of the method developed in the present work.

A direct beat note between two lasers can be detected up to tens of GHz on fast photodiodes, and offsets up to a couple of hundred GHz is achievable by beating one of the lasers with a high-order sideband of another laser resulting from its phase modulation with an EOM [**?**]. All the way up to octave-spanning THz offset frequencies can be achieved by utilizing the beat notes of two lasers with different spectral lines of an optical frequency comb [NAZ$^+$14], enabling optical clock frequency comparison.

Phase locking of two lasers with the aid of an optical beat note [SCLT94, CdAF+05] in principle produces the tightest frequency lock, reaching below sub-mHz instability levels. This optical phase locked loop (OPLL) method however places the most stringent demands on feedback stabilization bandwidths, requiring it to be appreciably larger than the linewidth of the lasers. This makes OPLLs especially challenging with semiconductor diode laser systems which possess linewidths from several hundred kHz to several tens of MHz. Nevertheless, many applications do not require phase locking, in which case laser frequencies can more easily be steered and locked using purely beat frequency discrimination – instead of phase discrimination.

Among typically utilized discriminators, simple delay-line based architectures [SEG+99, HIS+18] have been demonstrated to reach 1 kHz frequency difference instability, but they suffer from the technical complications brought by periodically repeating locking points. Digital counting architectures [HF08] have been demonstrated to reach 300 Hz instability, but suffer from implementation complexity and spurious digital noise (which could disturb laser power spectral density and negatively affect short-term stability). Architectures relying on integrated frequency-to-voltage conversion circuits have reached instabilities in the 30-100 Hz range, but they also suffer from implementation complexities that come about overcoming the limited frequency range ($\sim$1 MHz) of such chips. Similarly, side-of-filter type architectures [RCGW04, Pue12, SES+07] have also been demonstrated to reach down to the 100 Hz instability regime. Basic implementations of these architectures typically trade-off locking stability with the initial capture range of the lock, posing a general additional limitation.

Here we develop a frequency discrimination method based on hybrid LC filters for laser offset locking. The method is developed for the goals of obtaining a single lockable point with simultaneous wide-tunability, high locking stability, and a broad capture range. The implemented frequency discriminator (FD) generates an error signal with a 1.8-MHz-wide steep region and broad tails that extend out to hundreds of MHz for ensuring a large capture range. The all-analog design of the offset locking circuitry ensures low-noise operation. An offset frequency tunability of 1 GHz is incorporated by heterodyning the beat signal with a tunable microwave local oscillator (LO) generated from a direct digital synthesizer (DDS).

We demonstrate the developed method on two 780-nm miniature external cavity diode lasers (ECDLs) with $\sim$500 kHz observed free-running linewidths. We stabilize the frequency offset between the two lasers at around 5.5 GHz, and reach a frequency locking instability of 12 Hz at 10 s averaging time. This value corresponds to a fractional instability of 3×10^{-14} when scaled to the laser frequency. The long term instability remains below 55 Hz for more than 1000 s. To our knowledge, these results constitute the lowest beat-note-based offset locking instability published in absence of optical phase locking. Beyond its exceptional stability, the laser frequency offset is tunable at rates exceeding 200 kHz/μs by frequency ramping the DDS generating the LO. We note that the use of a simple LC circuit for laser offset locking was reported recently also in Ref. [CCL+17], but the operation was limited to $\sim$2 kHz instability levels. Below, we first detail our scheme and then describe the experimental characterization of its performance.

4.1.2 The scheme

Figure 4.2 shows a block diagram of the laser offset frequency locking scheme. Small portions of two lasers are superimposed on a 12-GHz-bandwidth photodetector, and the resulting beat note is amplified and heterodyned with a microwave LO. The frequency down-converted signal

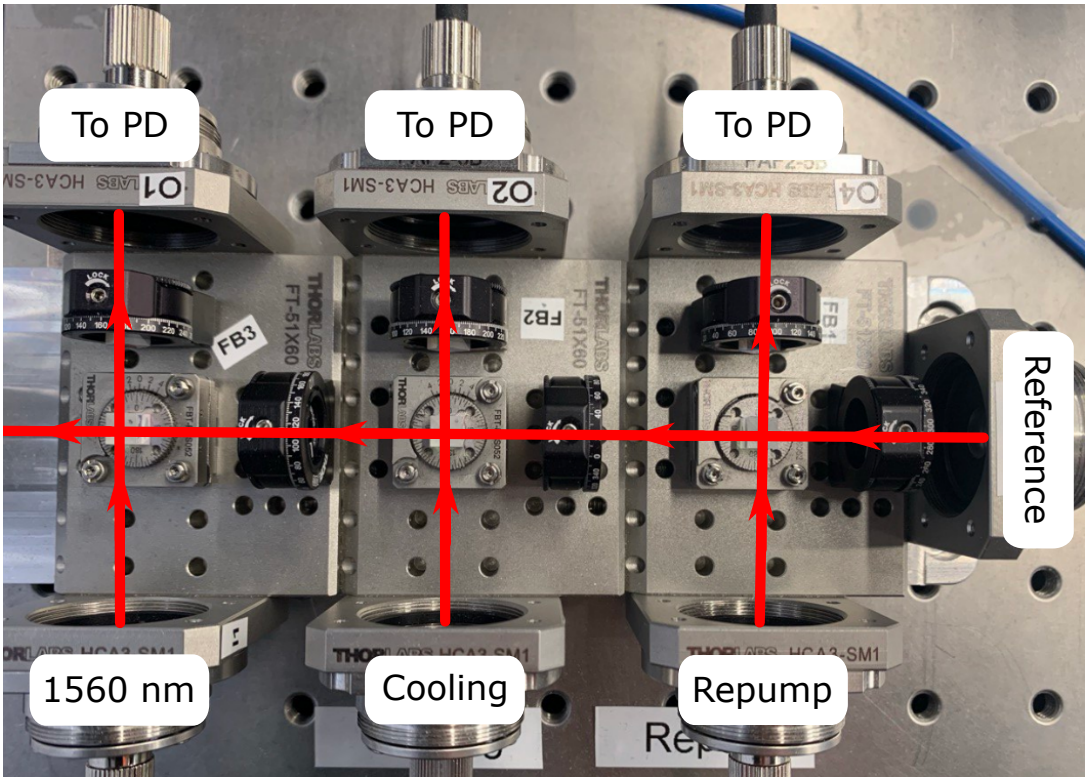

Figure 4.1: Image of the beatnote setup used to frequency offset lock OEWAVES, cooling, and repump lasers.

is further amplified, and its power is actively stabilized. This signal is then fed into the hybrid electronic FD to generate a baseband error signal that has opposite polarities on opposite sides of the desired frequency offset point. A home-built feedback controller is then used to stabilize the frequency of one of the lasers at this controllable offset point with respect to the other laser. The down-conversion process that brings the beat signal from the GHz regime to the MHz regime eases further electronic processing of the signal. At the same time, it enables the wide-range tunability of the frequency offset through induced changes in the LO frequency.

The FD (Fig. 4.3a) is the key component that generates the error signal with a tight resonance and a wide capture range. It is a self-mixing circuit with a specially designed hybrid filter in one of the two split arms. The input signal $\sim sin(\omega t + \phi_0)$ is distributed into the arms with a 2-way $90°$-power-splitter. Here ω is the angular frequency and ϕ_0 is an arbitrary phase. The arm with the hybrid filter contains the waveform $sin(\omega t + \phi_0) \equiv Re[i\, e^{-i(\omega t+\phi_0)}]$ while the other arm contains the $cos(\omega t + \phi_0)$ waveform. The filter transforms the incoming waveform with its transfer function $H(\omega) = H_{re}(\omega) + iH_{im}(\omega)$, resulting into the transmitted signal $Re[H(\omega)\, i\, e^{-i(\omega t+\phi_0)}] = H_{re}(\omega)\, sin(\omega t + \phi_0) - H_{im}(\omega)\, cos(\omega t + \phi_0)$. This is then combined on a frequency mixer with the $cos(\omega t + \phi_0)$ waveform coming from the other arm to result into the baseband signal proportional to $H_{im}(\omega)$ at the mixer output, which is used as the error signal (Fig. 4.3b).

The hybrid LC filter design eliminates the usual trade-off between lock tightness and capture range. The LC circuit contained in the upper branch of the hybrid filter (Fig. 4.3a) possesses a narrow resonance for tighter locking, and the one in the lower branch possesses a broad resonance for obtaining a wide capture range. The resulting hybrid filter thus inherits both properties. The resonance frequencies of the two filter branches must match to ensure the symmetry of the error signal in the vicinity of its zero-crossing. The location of the zero-crossing

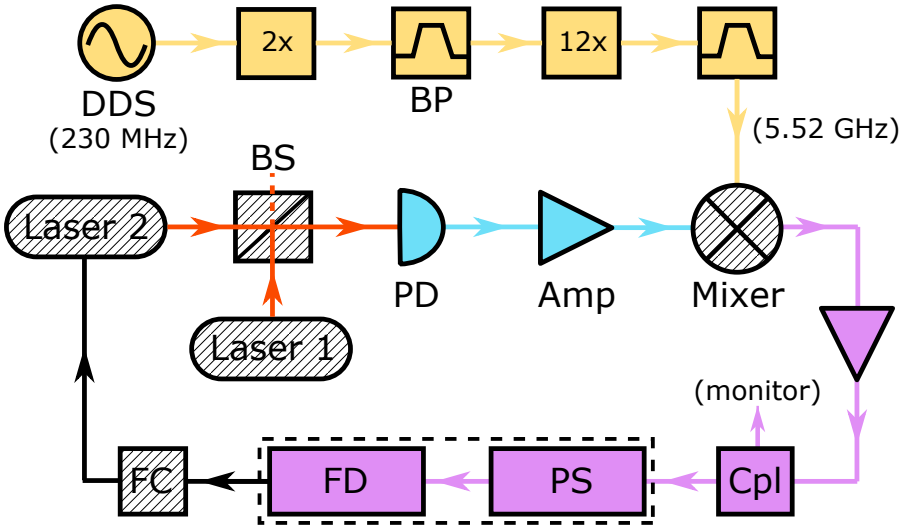

Figure 4.2: Block diagram of the frequency offset locking setup. The two lasers form a beat note on a fast photodetector (PD). The signal at ~ 5.5 GHz frequency difference (blue) is amplified and mixed down with a local oscillator (LO) chain (yellow) that starts with a direct digital synthesizer (DDS). The down-converted output (purple) of the mixer is in the MHz range, and is amplified to the saturation point. A directional coupler (Cpl) is used to monitor the beat note. The signal goes through an active power stabilization (PS) unit to stabilize the power at the input of the frequency discriminator (FD). The feedback controller (FC) then manipulates the current of Laser 2 to stabilize its frequency at a well defined offset from that of Laser 1. BP: bandpass filter, BS: beam splitter. Additional amplifiers in the LO chain are omitted from the diagram. Part list; PD: Thorlabs DX12CF, Amp: Mini-circuits ZX60-83LN-s+ and ZX60-43-s+, Mixer: ZX05-83-s+, Cpl: ZFDC-10-1-s+, 2x: ZX90-2-13-s+, 12x: ZX90-12-63-s+, DDS: Artiq Urukul, Lasers 1&2: Sacher Micron.

determines the exact frequency offset between the lasers, since the feedback loop stabilizes the error signal at the zero value. In our design, a resonance frequency of 22.6 MHz was chosen such that it is high enough to obtain a sufficiently large capture range, but low enough to facilitate an easy circuit implementation. Note that although the feedback loop always locks the signal seen by FD at 22.6 MHz, the actual laser offset frequency is given by the sum of this value and the frequency of the tunable LO.

The frequency of the laser that is to be stabilized is controlled through its injection current. A home-built analog feedback loop utilizing the error signal generated by the FD controls this current with a unity-gain bandwidth of ~ 100 kHz. The loop contains two intergrators with the second one kicking in for frequencies below 20kHz, giving rise to a $1/\omega^2$ feedback strength down to DC. The implementation of the feedback controller was carried out with particular attention to ground loops, which is typically a major source of stability degradation in many applications. The circuit board was designed such that all inputs and outputs are carried out differentially (interchangeably using AMP03 and LT1167 ICs), cutting ground connections between various devices, hence eliminating ground voltage shifts across the circuit board. In the implemented frequency feedback, the FD output was directly connected to the feedback controller after 50 Ω termination and some attenuation for loop gain tuning. No lowpass filtering was utilized to eliminate the harmonics of the beat note that the FD additionally generated. Such filtering was observed to shift the locking point – presumably due to back-reflections into the FD – but did not seem to noticeably affect the locking stability.

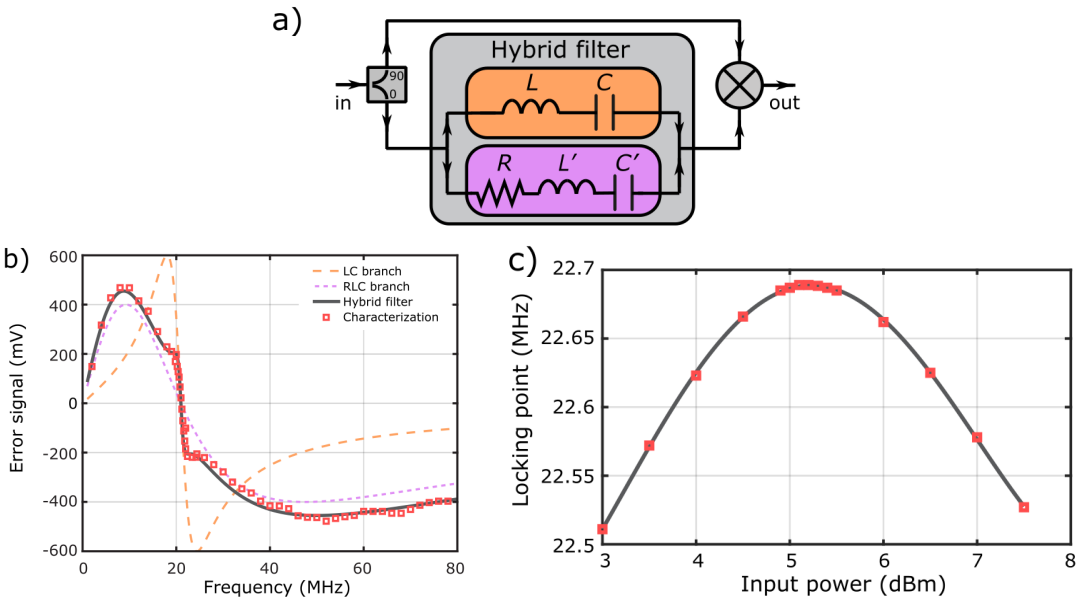

Figure 4.3: (a) Schematic drawing of the FD. The hybrid filter (gray box) is composed of two branches: one LC filter (orange box) and one RLC filter (purple box). It is part of a self-mixing circuit composed of a splitter (Mini-circuits PSCQ-2-51W+1) and a mixer (RPD-1+1 phase detector). The surface-mount component values are $L = 2.2\ \mu\mathrm{H}$, $C = 20\ \mathrm{pF}$ and $R = 50\ \Omega$, $L' = 470\ \mathrm{nH}$, $C' = 91\ \mathrm{pF}$. (b) Expected and observed frequency $(\omega/2\pi)$ responses of the FD given by the imaginary part of the transfer function $H_{im}(\omega)$, corresponding to the error signal. The theoretical response curves are scaled in magnitude to fit the experimentally characterized response (red squares). Contributions of individual branches are also explicitly indicated. (c) Zero-crossing frequency of the generated error signal as a function of input signal power at the FD (red squares), and a polynomial fit (solid line). All characterizations were carried out with a frequency stepped tone from a function generator.

Real-world analog mixers can develop an input-power dependent residual DC-offset in their outputs, even when no mixing to DC is expected in the ideal case [Rub06]. Thus, power fluctuations at the FD – containing a mixer – have the potential to turn into small additive fluctuations in the generated error signal. Since the feedback controller would mistake these for frequency offset fluctuations, power drifts and fluctuations could lead to degradation of the actual frequency offset stability. In order to suppress such effects, we first reduce power fluctuations by saturating the amplifiers leading to the FD (Fig. 4.2), and further utilize additional active feedback stabilization to fix the beat note power seen by the FD. This feedback circuitry (not shown) splits (Mini-circuits PSC-2-1+) the signal into two paths, and self-mixes (SRA-1-1+) the sample branch to effectively measure the power, and sends the other branch to the FD. A voltage variable attenuator (PAS-3+1) situated before the splitter then stabilizes the power by means of a low-bandwidth feedback loop utilizing the power measurement. Note, that the self mixing is carried out with power levels at least 10 dB below the mixer input-saturation point. The PCB circuit housing the FD and the power control circuitry (dashed box in Fig. 4.2) is operated with a nominal input power of 17 dBm, and remains identically functional down to 11 dBm. The amplifier saturation and the active RF power control provides a buffer for potential beat note power degradations over time (up to 10 dB) without compromising operational performance.

4.1.3 Experimental characterization

The error signal generated by the FD was characterized by applying a single tone from a function generator while stepping its frequency to map the response (Fig. 4.3b). The sharp region of the error signal was measured to have a width of 1.8 MHz in agreement with the design parameters. The lock capture range was empirically found to be around 190 MHz, ranging from 45 MHz below the unique locking point to 145 MHz above. The error signal tails extend further than this (Fig. 4.3b), but the noise on the error signal – originating from finite laser linewidths – hinders lock acquisition for initial conditions too far from the locking point. In free-running operation, the employed laser systems do not drift more than ∼50 MHz, justifying the choice of the design parameters leading to the observed capture range.

The effect of the non-ideal behavior of the FD mixer was characterized by measuring the error signal zero-crossing frequency as a function of the RF input power to the FD unit. Empirically, a 'turning point' was identified around 5.2 dBm (Fig. 4.3c) where the zero-crossing frequency was insensitive to the input power. These measurements were carried out with a single tone from a function generator. The exact power corresponding to the 'turning point' however appears to be linewidth dependent, and needs to be fine tuned in locked operation by observing the resulting mean frequency offset between the lasers. With saturated amplifiers and additional active power stabilization at the 'turning point', the stability was no longer limited by power fluctuations.

The evaluation of the achieved offset locking stability was carried out by recording the beat note frequency through the 22.6 MHz monitor output (Fig. 4.2) using a frequency counter (SRS FS470). Sample time traces with and without power stabilization are shown in Figure 4.4a, displaying the utility of power stabilization. For the power stabilized case, the mean frequency remains within a 200 Hz window over the course of a day. The characterized frequency offset instabilities at different time scales for this case are obtained by calculating the Allan deviation (Fig. 4.4b) of the recorded beat note data. The instability remains below 55 Hz for more than 1000 s and has a minimum value of 12 Hz at 10 s timescale. The measured lock tightness inferred from the closed loop error signal, and the limitations induced by detection noise measured in open loop with the lasers blocked (Fig. 4.4b), both contribute at least an order of magnitude lower than the observed frequency offset instability. The origin of the dominant contribution to the instability is currently unclear.

The agility of user inducible laser frequency offset changes is related to the bandwidth of the feedback loop controlling the stabilized laser's frequency. In the current setup, continuous ramp rates of 200 kHz/µs were achievable robustly. The range of instantaneous frequency jumps on the other hand were limited by the capture range of 190 MHz. Such step jumps settle towards the setpoint with a time constant of order 10 μs, determined by the inverse of the lock bandwidth. The frequency offset can be tuned within a range of 1 GHz, limited by the bandpass filters utilized in the microwave LO generation chain. In principle, given a widely tunable LO source, the only limitation to the tuning range is brought by the 12-GHz bandwidth of the photodetector (Fig. 4.2).

4.1.4 Summary

Described frequency offset locking technique is used to lock OEWAVES, cooling and repump lasers at a variable frequency offset with respect to the reference laser, that is in turn locked to the atomic transition. We find this method to be robust, flexible in terms of local oscillator offset, and simpler compared to the golden standard of using the digital frequency counters.

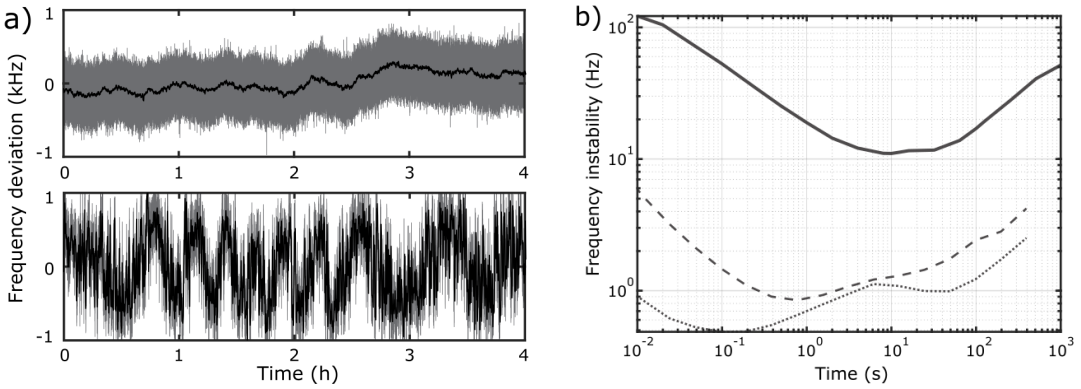

Figure 4.4: (a) Deviation of the monitored beat frequency with (upper) and without (lower) power stabilization. Gray: 0.01 s frequency counter gate time, black: 1 s gate time. (b) Allan deviation of the observed beat frequency (solid line) for the power stabilized case. A minimum of 12 Hz at 10 s averaging is reached, and the instability remains below 55 Hz for timescales exceeding 1000 s. The dashed line is the instability that would be naively inferred from the recorded residual error signal while the lock is engaged. The dotted line indicates the electronic noise floor inferred by blocking the laser light.

4.2 3D MOT alignment

Alignment of the 3D MOT requires aligning six perpendicular beams intersecting at the intended location of the atoms. In the absence of the vacuum chamber we first made alignment of the 3D MOT beams at the intended location of the cavity waist. After that the fine adjustment of the location of the 3D MOT was done by maximizing the equilibrium number of atoms in the 3D MOT and decreasing the atom loss during the cooling procedure.

We observed that the quality of the 3D MOT alignment can be judged on the atom loss during the far detuned cooling procedure. Bad alignments were correlated with larger initial cloud sizes, irregular shapes, and about $90\,\%$ of atom loss during the far detuned cooling. Good alignment was associated with smaller cloud sizes of about 0.3 mm, circular shape, and atom loss of about $30\,\%$ during the far detuned cooling to about 30 µK temperature.

We have established a procedure to make 3D MOT alignment easier and reproducible. We first installed the vacuum chamber without the cavity to start working on the cooling protocol and to be able to compare results with the cavity to check if the presence of cavity introduce any changes. Later we fine tuned the alignment once more without the vacuum chamber while we were working on installation of the cavity. Note that since there are many degrees of freedom, it is advised to fix the heights of the X and Y launchers and never touch them. This implies that we rely on the flatness of the bread board. It greatly helps in the further alignment procedures by minimizing the search space of the configuration resulting in better quality of the 3D MOT. The following sections will describe the detailed alignment procedures that we developed in the presence and absence of vacuum chamber.

4.2.1 3D MOT alignment without the vacuum chamber

It helps to coarsely align the beams to intersect in the absence of the chamber close to the location of the cavity waist. Firstly, the procedure starts with the alignment of three counter-propagating beams to each other, making them co-linear. It was done by overlapping two beams at distant points.Decreasing the beam size to the lowest size allowed by iris

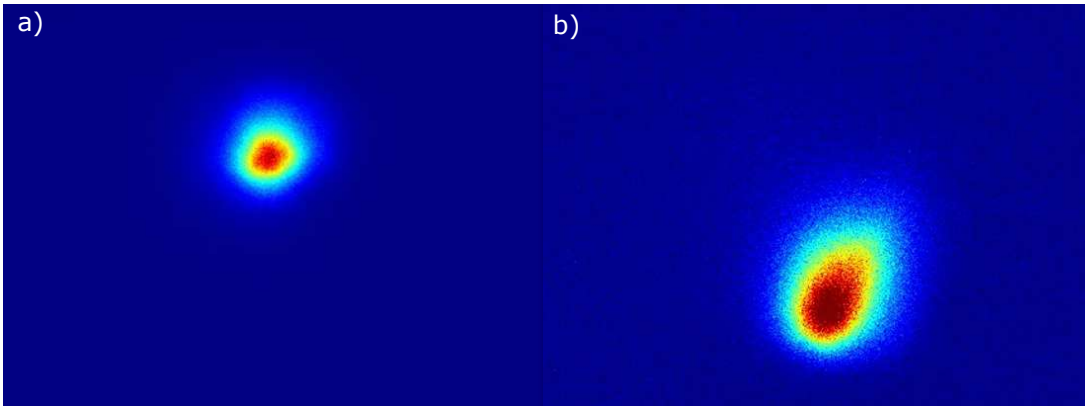

Figure 4.5: Image comparison of the atomic clouds observed from the top. The gain settings for two images were different. Presented for shape and size comparison . a) shows good alignment. It resulted in $15\,\%$ atom loss after the far detuned cooling to the temperature of $30\,\mu$K. It is more confined and dynamically stable when observed live. b) shows bad alignment. It resulted in $90\,\%$ atom loss after the far detuned cooling to the temperature of $30\,\mu$K. It is less confined and more dynamically unstable when observed live. It can wobble and change shapes.

diaphragms significantly enhanced the precision of their overlap. After that, sizes of the beams are adjusted to about 0.3 mm and aligned to intersect on a 0.5 mm white alignment cube made of paper that was placed at the intended location of the atoms (see figure 4.6). By moving the cube along one of the 3D MOT axis, we made sure that the other two perpendicular beams are properly overlapped. It was done by observing the two beams merge on the cube edge during the translation of the cube. The coarse alignment of the beams was done by iterative making each pair co-linear and then intersecting at the alignment cube multiple times until they remained co-linear and intersecting at the alignment cube. Finally, the fine alignment is done by minimizing the beam sizes to about 0.1 mm and overlapping them while observing their intersections at the optical lens cleaning tissue. By moving the cleaning tissue across the intersection point at various angles it is possible to identify the correct direction of adjustment. We found it very convenient to translate the beams in pairs by rotating the tuning knobs of linear stages to about 90° at a time. This was possible due to the similar distances of the launchers from the intersection point and allowed nearly co-linear translations of the beams. After few iterations of intersecting at the tissue and making them co-linear the beams were well aligned.

4.2.2 3D MOT alignment with the vacuum chamber

Once the vacuum chamber was installed, the previous method of alignment was not available. Therefore, we used the view port caps to help aligning the horizontal launchers in case we lost the configuration when we can observe atoms in 3D MOT. The alignment of the Z beams was partially constrained by the mirror size that is only slightly larger than the beam size. We used the top and bottom mirrors as a coarse vertical axis alignment to observe some atoms in the 3D MOT. After finding the alignment that resulted in an observable 3D MOT we fine tuned it by iteratively decreasing the beam sizes. We decrease the beam sizes to the point until it almost disappears. Then the direction of the translation is identified by blocking the beam from sides to see which side makes 3D MOT disappear. The blocking was performed in a knife edge technique with the orientation of the knife edge corresponding to the potential

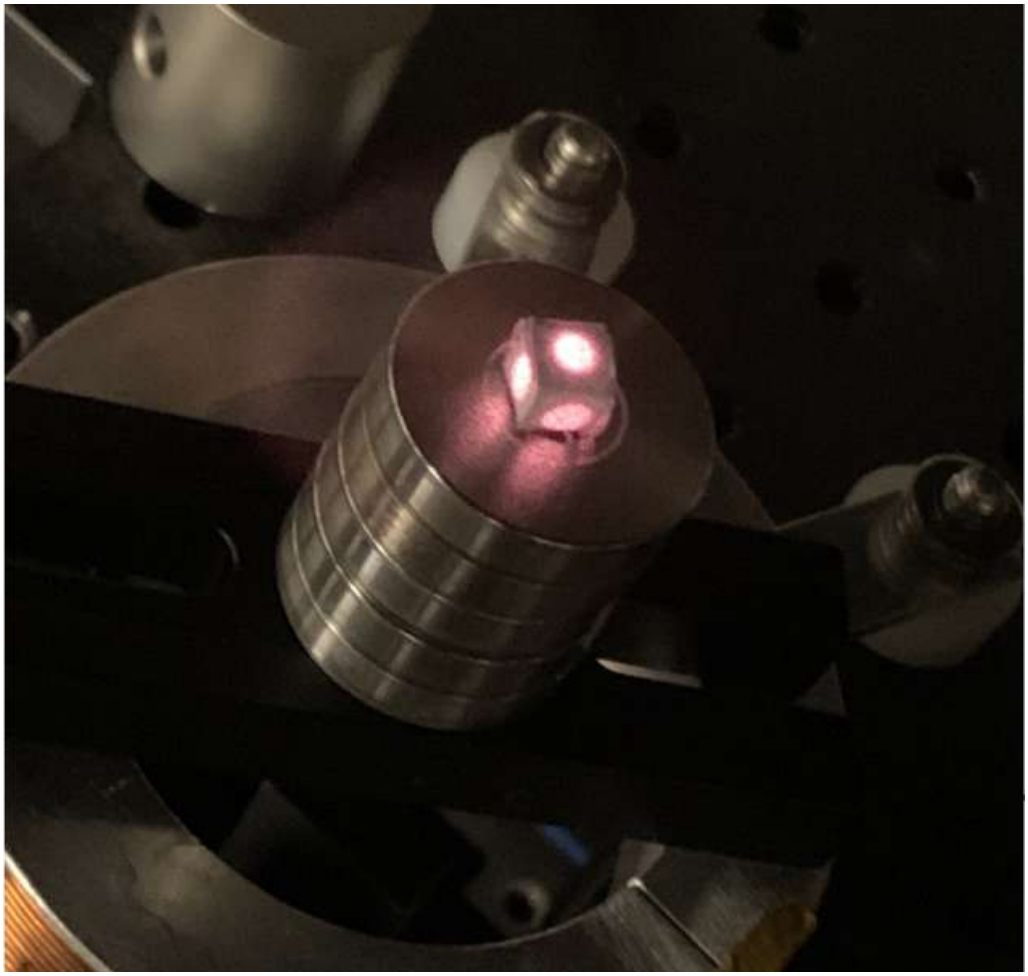

Figure 4.6: Coarse alignment of 3D MOT beams in the absence of vacuum chamber using the alignment cube. The hand made cube made alignment procedure easier and faster.

beam overlap. For horizontal launchers it was vertical, whereas for vertical beams it was at $\pm 45°$. After aligning the beams to each other by minimizing the beam size while preserving the atoms in 3D MOT, the 3D MOT was fine tuned for optimal alignment. This was achieved by opening the irises and carefully adjusting each knob of the 3D MOT to create a tighter and visually more dynamically stable cloud. We assume that the location of such 3D MOT might be associated with the zero location of the magnetic field. Our justification is that the 3D MOT is more confined there, that might be due to more efficient trapping of the atoms. Finding such position is a blind search. Therefore, once such location is identified the camera is fixed at the location centering the atomic cloud. It will help bringing the cloud to the specific location instead of blind search.

Ideal alignment of the 3D MOT would have corresponded to the nice confined cloud and expansion around the stationary center of mass inside of the full power and resonance molasses when the MOT coils are turned off. Due to the finite tolerance of the 3D MOT holes in the cavity body we could not achieve the alignment that would result in symmetric expansion without the motion of the center of mass. We tried to avoid light scattering from the cavity body while preserving sufficiently small distortion during the free expansion. Smaller distortion decreases the atom loss during the cooling procedure. In the end, we managed to find a good compromise between the amount of light scattering from the cavity body and atom loss during the cooling procedure.

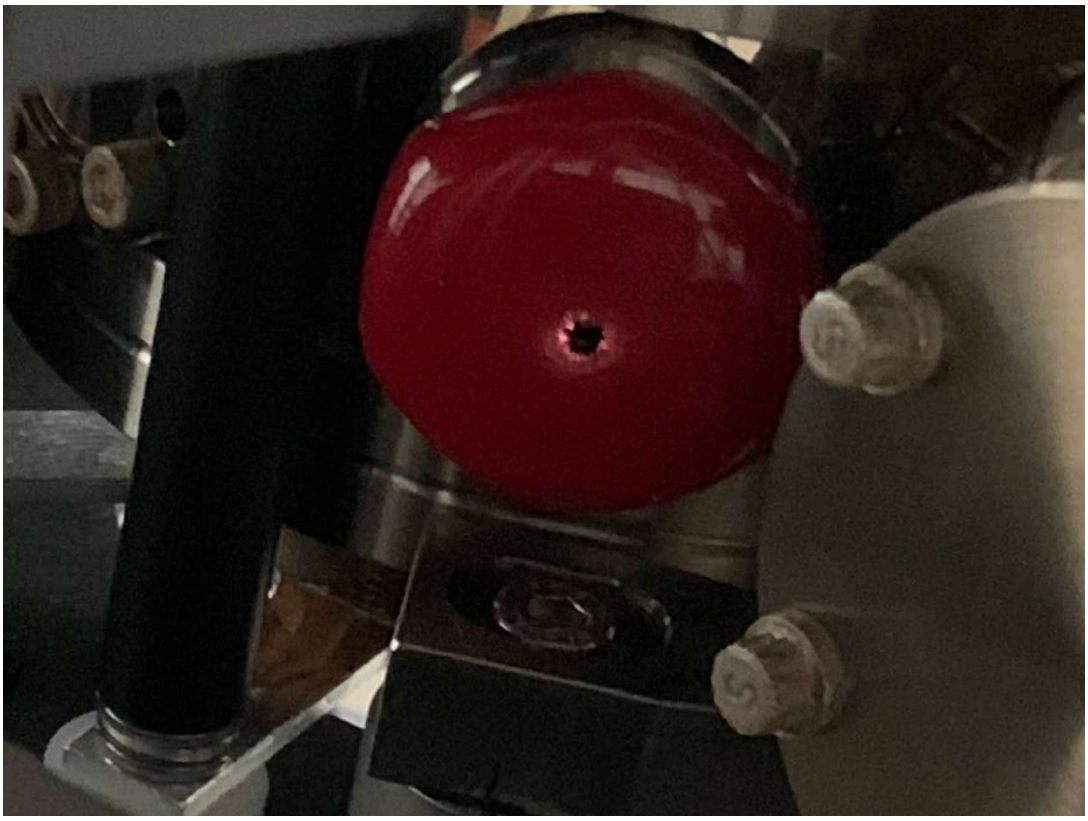

Figure 4.7: Coarse alignment of 3D MOT beams using the rubber caps on the view ports. Since we can not use other alignment procedure this helped us recover the 3D MOT after completely loosing it.

CHAPTER 5

Experimental control

5.1 Introduction

Due to the inherent probabilistic nature of quantum phenomena, measuring a quantum observable requires acquisition of sufficient data to deduce its mean and variance. Furthermore, since the very act of the measurement has a back action on the system, single measurement of the quantum observable requires re-initialization of the quantum state and performing multiple measurements. However, achieving identical conditions for each experimental run is impossible, leading to systematic errors that must be mitigated to obtain reliable results. Among the most notable sources of such systematic errors is the imprecision in timing during the experimental sequence. This imprecision significantly impacts all stages of the experiment, introducing systematic noise into atom numbers, manipulation quality, and readout outcomes. Consequently, precise timing control is essential for quantum observable measurements.

Nowadays, most experiments are triggered and controlled by computers. However, execution times of computers and communication latency with devices are on the order of tens of microseconds. This microsecond-level delay disrupts experiments running on atomic timescales, interfering with the precise timing required for the experimental sequence. Moreover, the latency has a probabilistic nature that depends on the availability of computational resources during the execution of the experiment. For instance, if a background Windows update is being downloaded at the time of execution it can cause nondeterministic jitters in the timing precision. Even without apparent distortions or heavy computational loads it is impossible to use conventional computers to ensure deterministic timing for experimental sequences because of the way computers store and access data in memory. Relying on the computer's "mood" for timing is inconvenient and may necessitate frequent recalibrations of relative timings. Fortunately, commercial products utilizing field-programmable gate arrays (FPGAs) and smart buffering features are available to ensure deterministic latencies at nanosecond time resolution.

In this chapter I will introduce precise timing and control system called ARTIQ. Then I will give a concise introduction to the important concepts, that allow deterministic timing control with nanosecond resolution. The description was partially based on the ARTIQ manual [ML24]. In conclusion, I will describe our solution implemented on top of the commercial product. This solution empowers users with ultimate control over their experiments without requiring any coding. Additionally, convenient and user-friendly extensions are available, eliminating the need for coding knowledge or an understanding of the underlying timing and control system. I will

particularly illustrate the experimental control software "Quantrol" that I developed over the course of my PhD, which is a graphical user interface based control program that interfaces with ARTIQ.

5.2 Precise timing and control system ARTIQ

ARTIQ stands for Advanced Real-Time Insfrastructure for Quantum physics. It is a next-generation timing and control system maintained and developed by M-Labs. ARTIQ was designed for control and automation of quantum experiments that require precise timing within experimental sequence. It provides tools and libraries that allow researchers to program, schedule, and control experiments with nanosecond timing resolution and sub microsecond deterministic latency. M-Labs offers a commercially available integration of the ARTIQ software with Sinara's modular hardware architecture, that allows users to assemble and configure hardware components tailored to their research needs. In particular, Sinara hardware encompasses FPGA based processing, input/output ports for digital and analog signals, as well as direct digital synthesizers (DDSs). Furthermore, ARTIQ infrastructure allows seamless synchronization of control signals that can be clocked with up to $1\,\mathrm{GHz}$.

One of the ARTIQ's remarkable features is the possibility to describe experimental sequence with a high-level programming language. This allows rapid prototyping and deploying complex experiments without delving into low-level details required to program FPGA. However, each description requires to be hard coded in order to be scheduled. Imagine searching through hundreds of lines of code to find the parameter to change. It is a very tedious, error prone and inconvenient procedure. Also, in order to operate the experimental control system one needs to be familiar with programming with all details that put apart ARTIQ code from the standard python, as well as the nuances arising from the complicated management of ARTIQ.

The inclusion of a graphical user interface in ARTIQ enhances experimental management, enabling parametrization, scheduling, and visualization of experimental outcomes. With ARTIQ's management system multiple experiments can be scheduled in sequence, enabling the execution of larger and more comprehensive experiments. These experiments are often constructed by assembling distinct experimental modules, such as "MOT loading", "State preparation" etc. These modules are designed to be reusable and can be combined flexibly to complete experiments.

5.3 Real-time input/output concepts

The key idea that enables precise timing and execution of the signals is to plan an event in advance. A typical ARTIQ code describing an experiment is composed of two types of "programs": regular Python code that is executed on the host and ARTIQ kernels that are executed on a core device. The central processing unit (CPU) that executes ARTIQ kernels has a direct access to specialized programmable input/output timing logic that is a part of the gateware[1]. If ARTIQ kernels were to directly interface with real-time gateware, it could introduce issues of imprecise, indeterminate, and unpredictable timing. Instead CPU operates at one end of a first-in-first-out (FIFO) buffers while the gateware on the other end guarantees all or nothing level of timing precision. A FIFO for an output channels hold timestamps and

[1]Gateware is responsible for controlling the data flow, signal processing, and overall behavior of the digital circuitry within the hardware device, in particular FPGAs.

parameters of signals that need to be executed, whereas FIFO for an input channel contains timestamps and data for the events being recorded by the real-time gateware and waiting to be read by the CPU.

The set of all input and output events in all channels constitutes the timeline. The output event in executed when the timestamp matches the reference clock cycle, whereas input event being recorded and stamped with the current clock value. In essence, the timeline is a digital representation of time, functioning as a scheduler for operations that need to occur during an experiment. The kernel timeline cursor can be moved forward or backward relative to the current value. It is important to keep the timeline cursor ahead of the real time reference clock throughout the execution of the program. This is required to ensure enough preparation time for events to be executed. The difference between the timeline cursor and real time is called a slack. In case of negative slack during the execution of the program, it quits with Underflow exception.

An example of ARTIQ code for experiment description is shown below:

```
from artiq.experiment import *

class DummyExperiment(EnvExperiment):
    def build(self):
        self.setattr_device("core")
        self.setattr_device("ttl0")

    @kernel
    def run(self):
        #initialization
        self.core.reset()
        self.core.break_realtime()

        #description
        self.ttl0.on()
        delay(2*us)
        self.ttl0.off()
        delay(2*us)
```

The DummyExperiment is declared as an object that inherits from EnvExperiment. The description is done by overwriting its build and run methods. Build method is used to specify the devices that are going to be used in this particular experiment. In the example above we use core and ttl0 that correspond to FPGA based processor Kasli and first digital channel respectively. Note that indexation of channels and devices starts from 0 instead of 1 due to the conventions of low-level programming language used for implementation. Run method describes the sequence of control signals. The self.core.reset() function flushes all input and output FIFO buffers to avoid previous settings from interfering with the current experiment execution. The self.core.breakrealtime() function puts the kernel timeline cursor 125000 machine units forward, where one machine unit equals to a period of the reference clock. In our setup it corresponds to 1 ns. In essence, the description of experiment consists of the information about whatever changes in the channels' state that need to be implemented at a particular time. In the example above the description is to turn on the channel ttl0 then move the timeline cursor by 2 µs and then turn ttl0 off and wait another 2 µs. The output of the example would be a ttl pulse that is 2 µs on and 2 µs off.

Note that the run method is decorated with @kernel to indicate that the following part of code will be executed on the core device and hence should be time critical. Other parts of code that are not decorated are executed on the host that is a lab PC in our case. Part of the code executed on the core device have some constraints compared to python since low-level language is used to program FPGAs. For instance, integer lengths should be specified as 32-bit or 64-bit, and lengths of lists should be defined before hand. For more detailed restrictions of kernel code please refer to the manual of the ARTIQ.

5.4 Management system of ARTIQ

Management system is a high-level part of the ARTIQ that is responsible to schedule the experiments, distribute and store the results, and manage the devices and their parameters. Without diving into details, let's consider only the high-level explanation as we would not need to know anything with the control system that we have developed.

ARTIQ system utilizes a server-client workflow for instrumental control. Server can be understood as a collection of objects and methods that can be used to control the hardware. By connecting to the server, a client can ask the server to schedule the experiment by providing the corresponding description similar to the one explained in the previous chapter. ARTIQ's management system allows the smart use of various stages of experiments. Each experiment has preparation, running and analysis stages. In principle, while the previous experiment is running and there is a dead time for the processor it can start preparation of the following experiment. Recall, that the running of the experiment is scheduled in future.

This feature of utilizing the dead times in a smart way might allow some input dependent action during the experimental sequence. However, it requires careful design to ensure the analysis completes before the dead time is over.

5.5 Quantrol

The workflow of servers and clients, python like programming language with its implied constraints, bulky experimental sequences that can easily span multiple hundreds lines of code. Sounds like a very complicated system that requires extensive training and is not very convenient to work with even after proper training.

Those are some of the reasons why we spent about two years to develop the Quantrol. It is a custom GUI that generates experimental descriptions through an intuitive interface by filling tables. Notably, it supports variable definition, mathematical expressions for parameter setting, variables scanning, experimental sequence saving and loading, and even standalone program execution. Furthermore, due to its convenient tabular structure it helps visualizing the sequence much better than hundreds lines of code and also makes sure that user does not accidentally enter the values out of the range allowed by the Sinara hardware. It is our extension over ARTIQ infrastructure that offers flexible hardware control without requiring expertise in coding, allowing additional features, and broadening the accessibility of precise timing and control system. The only limitation is the ignorance of different experimental stages. However, Quantrol can be used to generate the experimental description that would require additional hard coding of the analysis on top of that.

Quantrol is a standalone application that consists of five tabs: Sequence, Digital, Analog, DDS, and Variables (see figure 5.1). Sequence tab is the main tab that is used to describe

the timing sequence, introduce parameters of a scan, and perform overall control of the experiment and the GUI. A timing sequence is presented in the form of a table, which includes the following description of the edge: number, descriptive name, unique ID that can be used as a default variable, mathematical expression representing time, and corresponding time value in milliseconds. Time is defined in milliseconds for user convenience as millisecond is the most relevant time scale for cold atoms experiments. Edges in timing sequence are automatically arranged in ascending order.

The Digital, Analog, and DDS tabs share a similar layout featuring a timing sequence on the left side of the table with columns for edge number, edge name, and a corresponding timestamp value. Following this, the table provides a description of channels' states. They also share a common background coloring pattern for cells: green indicates that the channel should be turned on with a specified value, red indicates that the channel should be turned off, and white indicates that the channel requires no action at this time edge and shows the current state of the channel just for user convenience. Each channel title name can be modified for better description. Digital channels accept only values 0 and 1 that correspond to off and on states respectively. Analog channels accept values from -10 to 10 (exclusive). DDS channel description consists of frequency, amplitude, attenuation, phase and state indicating whether the output should be turned on or off by 1 or 0 respectively. The GUI automatically throws an error and prevents the user from assigning the values outside of the allowed range for all of the parameters. Even when the value of the variable that is used in the expression of a parameter is attempted to be changed.

Variables tab is used to define variables by specifying the variable name and its value. These variables, along with the default variables that are IDs of time edges, can be used in the description of times in timing sequence table, analog channel values, and DDS channel parameters. For instance, in the figure 5.1 the edge 'Flush end' is defined at a 1000 ms delay with respect to edge id1.

When the program is initialized it only consists of one default edge that corresponds to the state of the system in the beginning of the sequence. The time counts relative to that edge and hence its time equals to 0. Further description of an experimental sequence is done by inserting additional edges, defining their times and modifying the relevant channel states.

The default state consists of the initial values of all channels as well as the tab names for channels for better readability. For instance, if the first digital channel is used for turning on and off the magnetic field of the MOT coils we call it "D0 MOT B field". In case one needs to use this channel for other purpose, the user can change the tab name by clicking on it and then overwrite the default state by clicking "save default".

For the comparison the same experimental sequence implemented with the bare code is shown in figure 5.4. It consists of 292 lines of code. Note that this is just the far detuned cooling portion of the entire experiment. Complete experimental sequence can easily span over a thousand lines of code.

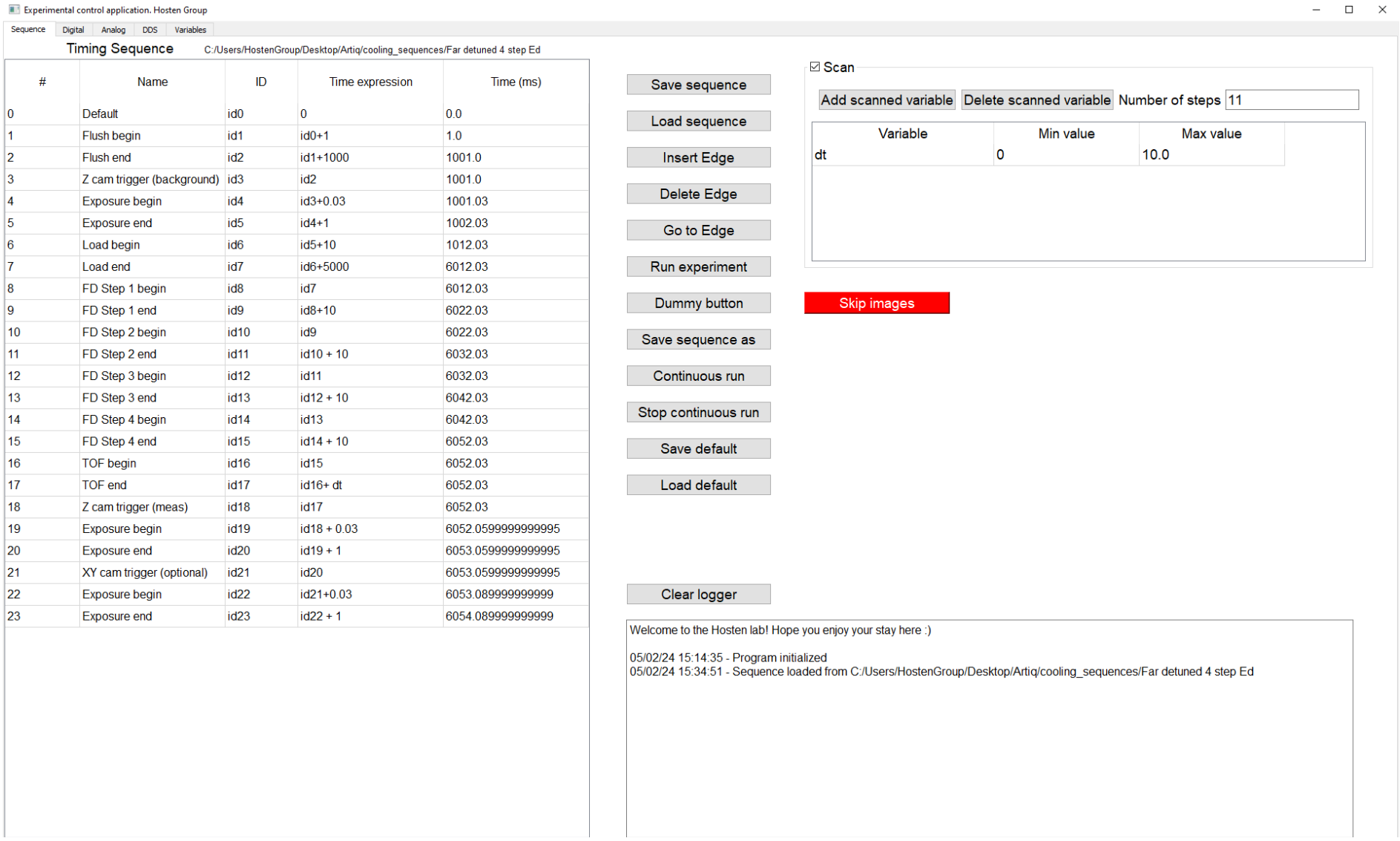

Figure 5.1: Snapshot of the sequence tab for time of flight measurements after far detuned cooling.

Experimental control application. Hosten Group

Sequence | Digital | Analog | DDS | Variables

Digital channels

#	Name	Time (ms)	D0 X shutter	D1 Xqwp shutter	D2 Y shutter	D3 Yqwp shutter	D4 Ztop shutter	D5 Zbot shutter	D6 Repump shutter	D7 MOT B-fld switch	D8 Z camera trig	D9 X-Y camera trig	D10	D11
0	Default	0.0	0	0	0	0	0	0	0	0	0	0	0	0
1	Flush begin	1.0	0	0	0	0	0	0	0	0	0	0	0	0
2	Flush end	1001.0	0	0	0	0	0	0	0	0	0	0	0	0
3	Z cam trigger …	1001.0	0	0	0	0	0	0	0	0	1	0	0	0
4	Exposure begin	1001.03	0	0	0	0	0	0	0	0	0	0	0	0
5	Exposure end	1002.03	0	0	0	0	0	0	0	0	0	0	0	0
6	Load begin	1012.03	0	0	0	0	0	0	0	1	0	0	0	0
7	Load end	6012.03	0	0	0	0	0	0	0	1	0	0	0	0
8	FD Step 1 begin	6012.03	0	0	0	0	0	0	0	1	0	0	0	0
9	FD Step 1 end	6022.03	0	0	0	0	0	0	0	1	0	0	0	0
10	FD Step 2 begin	6022.03	0	0	0	0	0	0	0	1	0	0	0	0
11	FD Step 2 end	6032.03	0	0	0	0	0	0	0	1	0	0	0	0
12	FD Step 3 begin	6032.03	0	0	0	0	0	0	0	1	0	0	0	0
13	FD Step 3 end	6042.03	0	0	0	0	0	0	0	1	0	0	0	0
14	FD Step 4 begin	6042.03	0	0	0	0	0	0	0	1	0	0	0	0
15	FD Step 4 end	6052.03	0	0	0	0	0	0	0	1	0	0	0	0
16	TOF begin	6052.03	0	0	0	0	0	0	0	0	0	0	0	0
17	TOF end	6052.03	0	0	0	0	0	0	0	0	0	0	0	0
18	Z cam trigger (meas)	6052.03	0	0	0	0	0	0	0	0	1	0	0	0
19	Exposure begin	6052.0599…	0	0	0	0	0	0	0	0	0	0	0	0
20	Exposure end	6053.0599…	0	0	0	0	0	0	0	0	0	0	0	0
21	XY cam trigger (optional)	6053.0599…	0	0	0	0	0	0	0	0	0	1	0	0
22	Exposure begin	6053.0899…	0	0	0	0	0	0	0	0	0	0	0	0
23	Exposure end	6054.0899…	0	0	0	0	0	0	0	0	0	0	0	0

Figure 5.2: Snapshot of the digital tab for time of flight measurements after far detuned cooling.

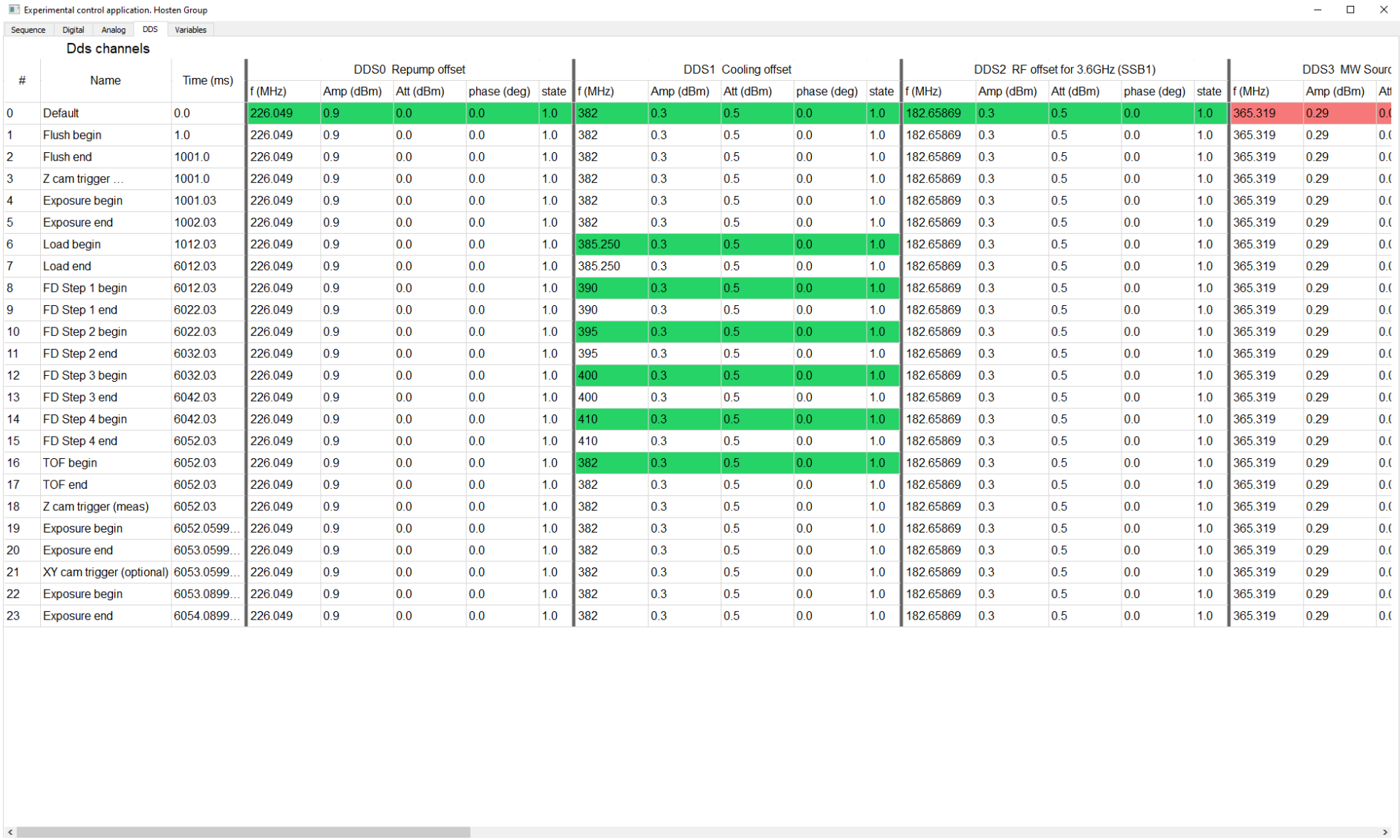

#	Name	Time (ms)	DDS0 Repump offset					DDS1 Cooling offset					DDS2 RF offset for 3.6GHz (SSB1)					DDS3 MW Sourc		
			f (MHz)	Amp (dBm)	Att (dBm)	phase (deg)	state	f (MHz)	Amp (dBm)	Att (dBm)	phase (deg)	state	f (MHz)	Amp (dBm)	Att (dBm)	phase (deg)	state	f (MHz)	Amp (dBm)	Att
0	Default	0.0	226.049	0.9	0.0	0.0	1.0	382	0.3	0.5	0.0	1.0	182.65869	0.3	0.5	0.0	1.0	365.319	0.29	0.(
1	Flush begin	1.0	226.049	0.9	0.0	0.0	1.0	382	0.3	0.5	0.0	1.0	182.65869	0.3	0.5	0.0	1.0	365.319	0.29	0.(
2	Flush end	1001.0	226.049	0.9	0.0	0.0	1.0	382	0.3	0.5	0.0	1.0	182.65869	0.3	0.5	0.0	1.0	365.319	0.29	0.(
3	Z cam trigger ...	1001.0	226.049	0.9	0.0	0.0	1.0	382	0.3	0.5	0.0	1.0	182.65869	0.3	0.5	0.0	1.0	365.319	0.29	0.(
4	Exposure begin	1001.03	226.049	0.9	0.0	0.0	1.0	382	0.3	0.5	0.0	1.0	182.65869	0.3	0.5	0.0	1.0	365.319	0.29	0.(
5	Exposure end	1002.03	226.049	0.9	0.0	0.0	1.0	382	0.3	0.5	0.0	1.0	182.65869	0.3	0.5	0.0	1.0	365.319	0.29	0.(
6	Load begin	1012.03	226.049	0.9	0.0	0.0	1.0	385.250	0.3	0.5	0.0	1.0	182.65869	0.3	0.5	0.0	1.0	365.319	0.29	0.(
7	Load end	6012.03	226.049	0.9	0.0	0.0	1.0	385.250	0.3	0.5	0.0	1.0	182.65869	0.3	0.5	0.0	1.0	365.319	0.29	0.(
8	FD Step 1 begin	6012.03	226.049	0.9	0.0	0.0	1.0	390	0.3	0.5	0.0	1.0	182.65869	0.3	0.5	0.0	1.0	365.319	0.29	0.(
9	FD Step 1 end	6022.03	226.049	0.9	0.0	0.0	1.0	390	0.3	0.5	0.0	1.0	182.65869	0.3	0.5	0.0	1.0	365.319	0.29	0.(
10	FD Step 2 begin	6022.03	226.049	0.9	0.0	0.0	1.0	395	0.3	0.5	0.0	1.0	182.65869	0.3	0.5	0.0	1.0	365.319	0.29	0.(
11	FD Step 2 end	6032.03	226.049	0.9	0.0	0.0	1.0	395	0.3	0.5	0.0	1.0	182.65869	0.3	0.5	0.0	1.0	365.319	0.29	0.(
12	FD Step 3 begin	6032.03	226.049	0.9	0.0	0.0	1.0	400	0.3	0.5	0.0	1.0	182.65869	0.3	0.5	0.0	1.0	365.319	0.29	0.(
13	FD Step 3 end	6042.03	226.049	0.9	0.0	0.0	1.0	400	0.3	0.5	0.0	1.0	182.65869	0.3	0.5	0.0	1.0	365.319	0.29	0.(
14	FD Step 4 begin	6042.03	226.049	0.9	0.0	0.0	1.0	410	0.3	0.5	0.0	1.0	182.65869	0.3	0.5	0.0	1.0	365.319	0.29	0.(
15	FD Step 4 end	6052.03	226.049	0.9	0.0	0.0	1.0	410	0.3	0.5	0.0	1.0	182.65869	0.3	0.5	0.0	1.0	365.319	0.29	0.(
16	TOF begin	6052.03	226.049	0.9	0.0	0.0	1.0	382	0.3	0.5	0.0	1.0	182.65869	0.3	0.5	0.0	1.0	365.319	0.29	0.(
17	TOF end	6052.03	226.049	0.9	0.0	0.0	1.0	382	0.3	0.5	0.0	1.0	182.65869	0.3	0.5	0.0	1.0	365.319	0.29	0.(
18	Z cam trigger (meas)	6052.03	226.049	0.9	0.0	0.0	1.0	382	0.3	0.5	0.0	1.0	182.65869	0.3	0.5	0.0	1.0	365.319	0.29	0.(
19	Exposure begin	6052.0599...	226.049	0.9	0.0	0.0	1.0	382	0.3	0.5	0.0	1.0	182.65869	0.3	0.5	0.0	1.0	365.319	0.29	0.(
20	Exposure end	6053.0599...	226.049	0.9	0.0	0.0	1.0	382	0.3	0.5	0.0	1.0	182.65869	0.3	0.5	0.0	1.0	365.319	0.29	0.(
21	XY cam trigger (optional)	6053.0599...	226.049	0.9	0.0	0.0	1.0	382	0.3	0.5	0.0	1.0	182.65869	0.3	0.5	0.0	1.0	365.319	0.29	0.(
22	Exposure begin	6053.0899...	226.049	0.9	0.0	0.0	1.0	382	0.3	0.5	0.0	1.0	182.65869	0.3	0.5	0.0	1.0	365.319	0.29	0.(
23	Exposure end	6054.0899...	226.049	0.9	0.0	0.0	1.0	382	0.3	0.5	0.0	1.0	182.65869	0.3	0.5	0.0	1.0	365.319	0.29	0.(

Figure 5.3: Snapshot of the DDS tab for time of flight measurements after far detuned cooling.

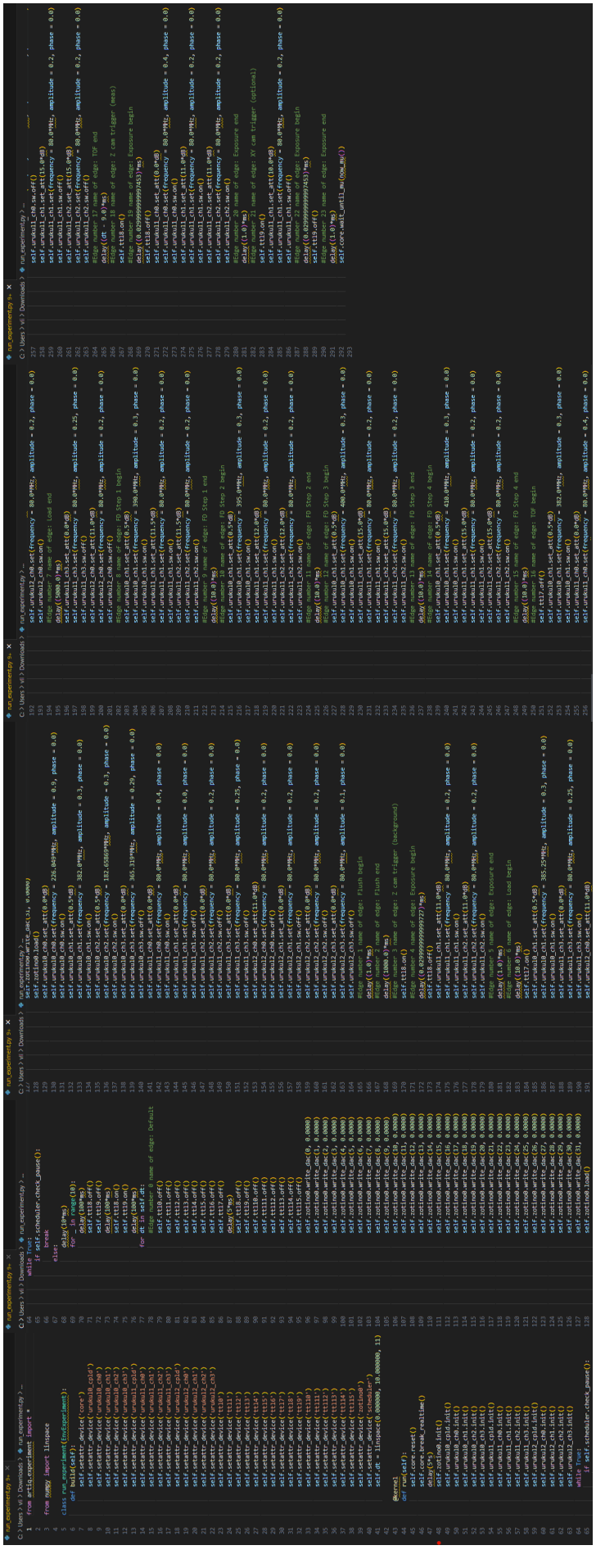

Figure 5.4: Code used to describe time of flight measurements after far detuned cooling. Total length of the code is 292 lines.

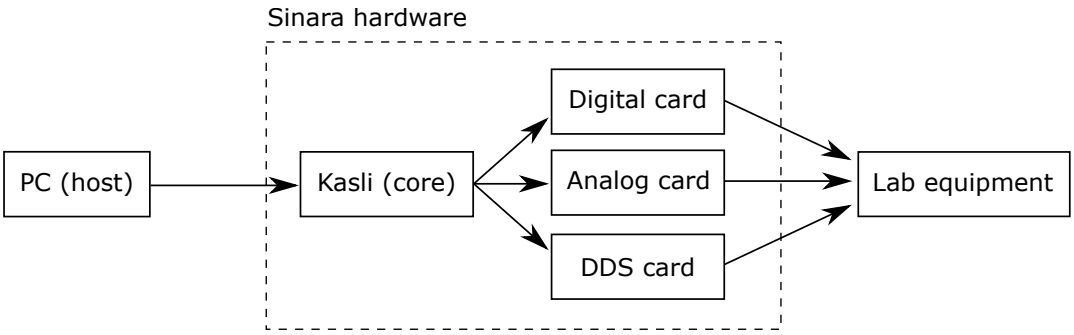

Figure 5.5: Schematic drawing of experimental control

5.6 Our setup

In our setup control over experiment is implemented according to the scheme shown in figure 5.5. Experimental sequence is loaded from the host computer to Kasli, the processor of Sinara hardware, which is commonly referred to as core device. Kasli then controls digital, analog and DDS cards that generate corresponding signals that act as drives for acousto-optic modulators (AOMs), references for frequency offset generation chains, controls for analog switches, magnetic field offsets and triggers for cameras. There might be finite latency between the generation of a control signal and the actual effect taking place. However, since the delay is deterministic it is always possible to compensate for that. Data acquisition and analysis is done separately from the Quantrol system. Quantrol is only used to trigger the acquisition.

In our lab we are using Kasli as a versatile FPGA based core device that serves as a CPU of the Sinara archtecture. Under the Kasli operation we have the capability to have 16 digital outputs or inputs, 16 analog outputs or inputs, and 12 DDS outputs.

Figure 5.6: Image of the Sinara hardware.

CHAPTER 6

Experimental sequence

6.1 Overview

Experiment starts at the ^{87}Rb source. In this source, atoms are laser cooled transversely in a 2 dimensional magneto optical trap (2D MOT) to form a cigar shaped atomic cloud. Then the atomic cloud is pushed forward through a pinhole with a push beam into the main chamber. There the atoms are trapped in a 3D MOT formed by three orthogonal pairs of counter-propagating laser beams and a magnetic field gradient generated by MOT coils. After that, atoms are cooled inside a far detuned MOT and optical molasses. After molasses cooling atoms at few μK will be transferred to the Dipole trap of the cavity.

After cooling and trapping the atoms, we state prepare them all in $|\downarrow\rangle$ state and start experimental sequence shown in the figure 6.1. It starts with applying an RF $\pi/2$ pulse to bring atoms in a equal superposition of $|\downarrow\rangle$ and $|\uparrow\rangle$ states. At this point the spin presqueezing

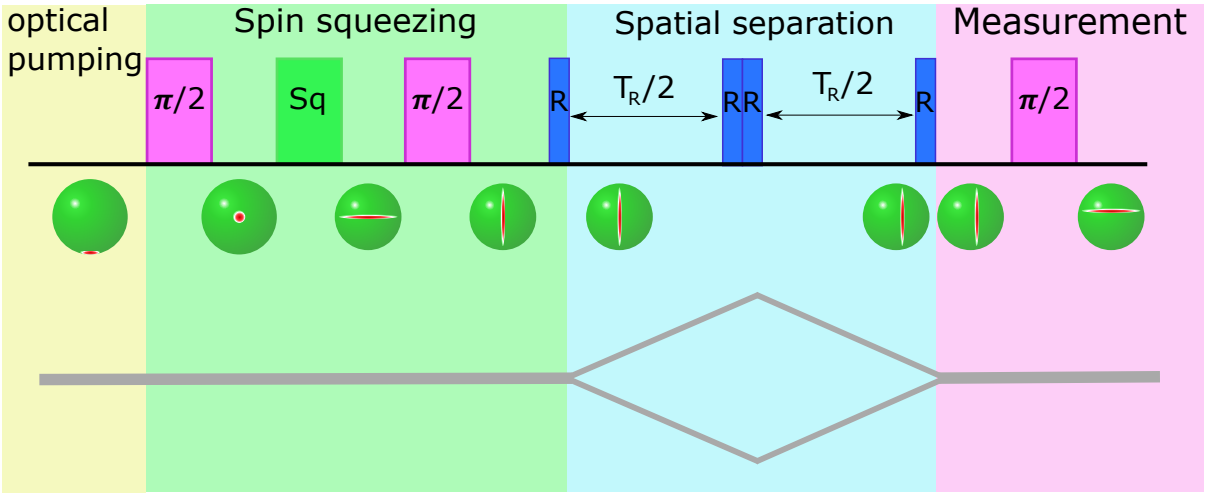

Figure 6.1: Proposed experimental sequence for quantum entanglement enhanced atom interferometer. The colored rectangles represent different experimental procedures and corresponding collective spin states before and after of each procedure are shown below on the Bloch sphere. The pink rectangles are RF $\pi/2$ pulses, green rectangle is a spin squeezing procedure and blue rectangles are Raman pulses. Lastly, the dark grey line pictorially represents the spatial confinement of the atomic could in time.

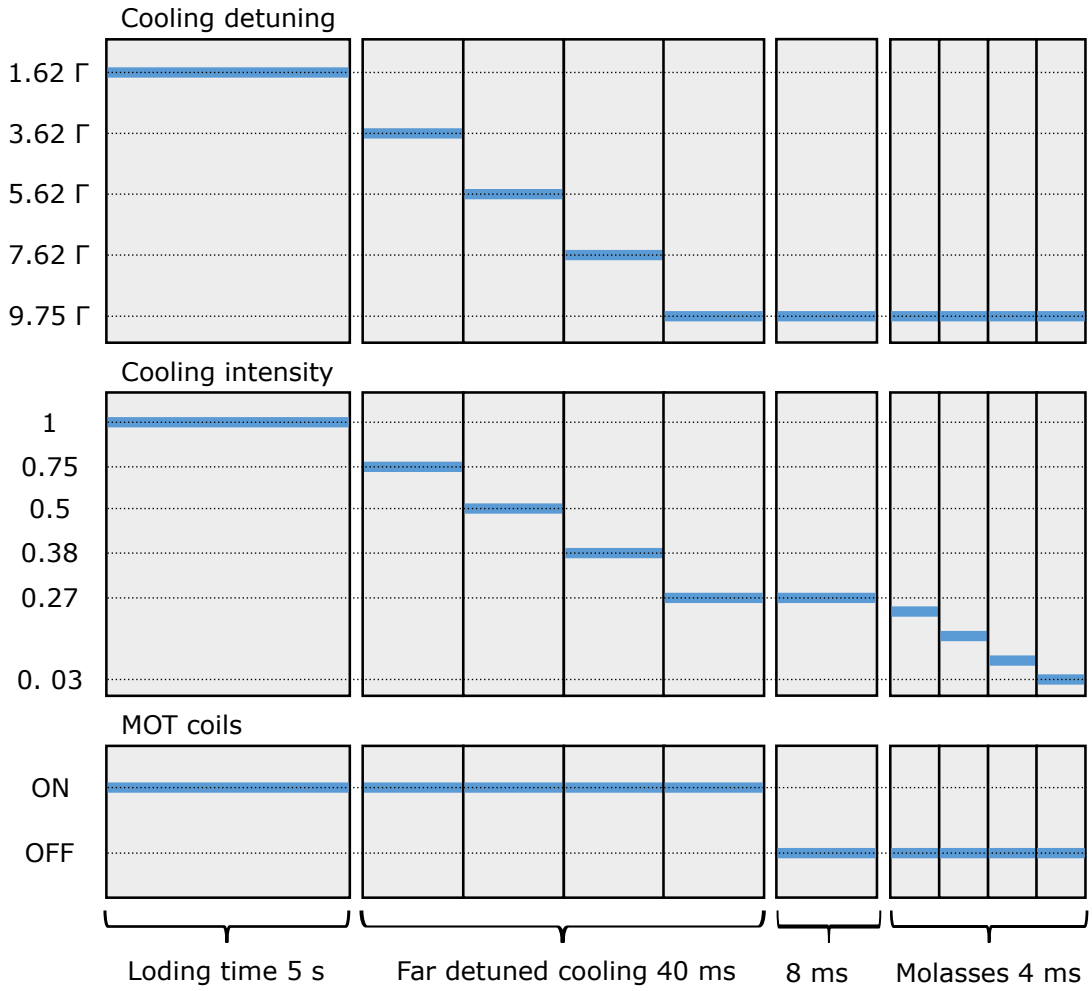

Figure 6.2: Schematic of the cooling sequence. Duration of each part is not drawn to scale. Cooling intensity is shown in terms of a fraction of full power of $32.8\,\mathrm{mW/cm^2}$, for better readability.

and squeezing with positioning the state at the equator with least noisy projection along J_z projection is performed. After that another RF $\pi/2$ pulse is applied to orient the state in the phase sensitive position. Once the squeezed state of the internal degree of freedom is prepared it will be mapped into momentum space via state dependent kick induced by Raman pulses. After $T_R/2$ two more Raman pulses will be applied, first to stop and second to redirect atomic clouds towards each other. After another $T_R/2$ the two clouds are recombined by applying another Raman pulse. Finally, the RF $\pi/2$ pulse will rotate the state with least noisy projection along J_z and then the measurement of population difference will finalize proposed experimental sequence. The experimental sequence will be repeated multiple times to acquire sufficient statistics to infer the mean and variance of the phase measurements.

In the following sections I will describe different stages of experiment by providing more detailed explanations and system characterizations.

6.2 3D MOT loading and cooling

As was mentioned previously, the atom source was customized for our vacuum chamber parameters that resulted in a reduced loading rates. Therefore we are currently working with

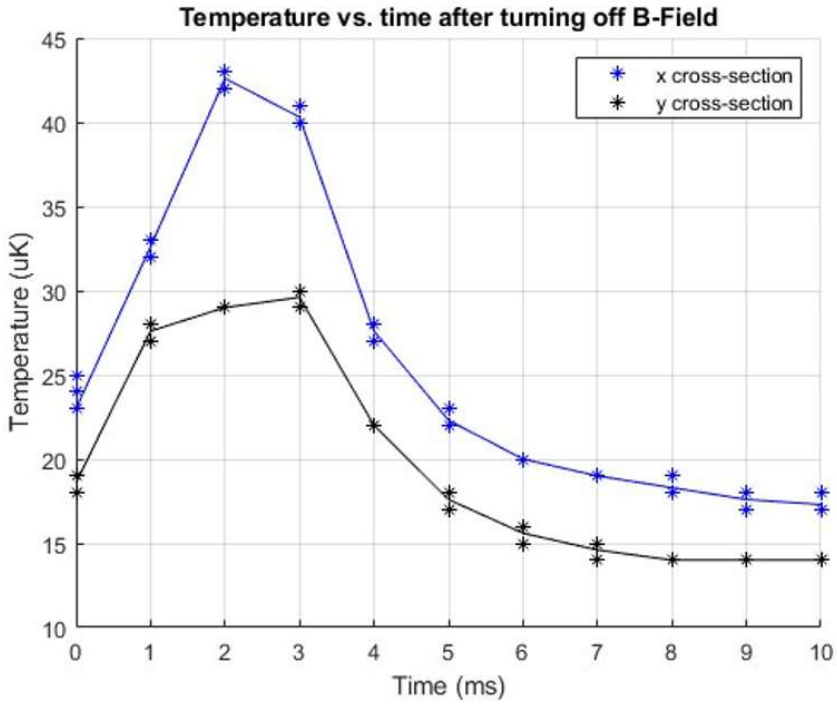

Figure 6.3: Cloud temperature as a function of the relaxation time after turning off the MOT coils at the end of the far detuned cooling. The heating effect is believed to be due to the Eddy currents that shift the energy levels and cause heating as cooling laser might address heating transitions.

relatively long loading times. The loading starts with 3D MOT beams and MOT coils on. To start loading we turn on the 2D MOT cooling and push beams for 5 seconds. The resulting cloud trapped in the 3D MOT consists of about 6 million atoms with a lifetime of $16\,$s and temperature of about $250\,\mu$K. The final temperature as well as the cloud size depends on the alignment. The value presented here is the value for the latest rather small cloud aligned with zero of the magnetic field mainly generated by MOT coils. Standard deviation of a short term atom number fluctuations when loading for $5\,$s are about $1.5\,\%$.

To further cool the atoms we implemented a $40\,$ms far detuned cooling procedure. It is used within the 3D MOT by increasing the detuning of cooling lasers and decreasing their intensities in four steps shown in figure 6.2. After far detuned cooling we analyzed the temperature evolution as we turned off the MOT coils to infer the amount of time before the Eddy currents decay to the levels that will not affect further cooling. From the figure 6.3 we observed a temporary temperature increase, most probably due to the magnetic field fluctuations. Therefore, we decided to wait $8\,$ms before performing molasses cooling. Technically that waiting time is also a molasses cooling as the cloud is exposed to optical molasses. However, we call the molasses cooling only in case we are decreasing the light power further during that step.

Molasses cooling is a $4\,$ms long procedure consisting of four $1\,$ms steps. All steps during far detuned cooling and molasses cooling were performed in a linear steps in time. In order to improve the molasses cooling we used microwave spectroscopy to zero magnetic field. However, it resulted only in minor improvements. Most probaly due to the fact that the magnetic field oscillations was not over. We zeroed the magnetic field at the center of the molasses cooling sequence.

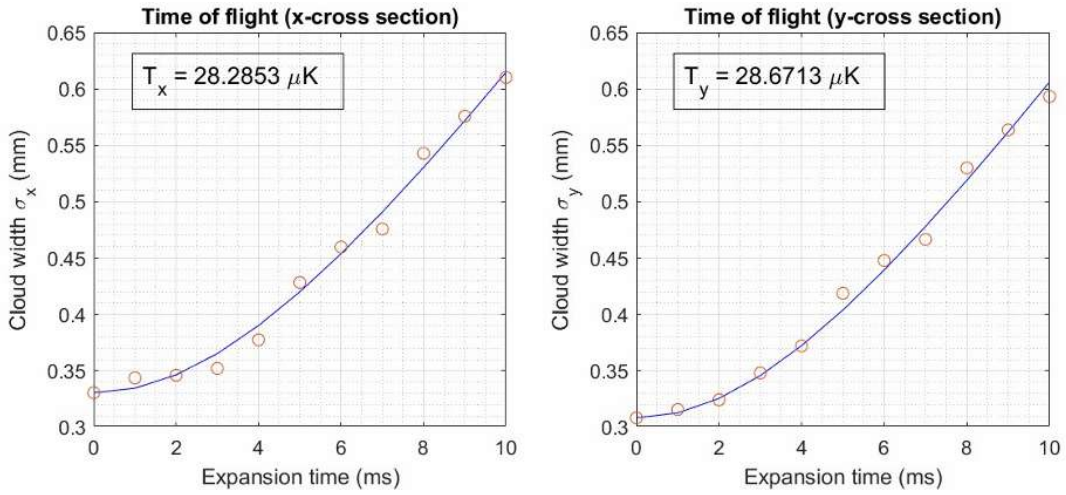

Figure 6.4: Time of flight fits for x and y crossections to measure the temperature after the far detuned cooling. Both temperatures show about $28\,\mu$K.

It is worth noting that the longer waiting times especially in molasses result in loss of atoms. Therefore one could look into optimizing the cooling procedures. For example, just quick trial of using steps, approximately exponential in time during the far detuned cooling, improved the atom number by about $10\,\%$. Also waiting longer times after turning off MOT coils might have resulted in better cooling and zeroing of the magnetic field. However, for now we decided to proceed without such complications. We also see a possibility of using reinforcement learning to further improve the atom number loss.

The temperature of the cloud after far detuned (FD) cooling was characterized to be around $28\,\mu$K. The results of time of flight measurements in figure 6.4. The loss of the atoms at this point in cooling was about $30\,\%$. We are going to try to transfer the atoms at that temperature directly into the dipole trap in order to preserve the atom number. The rule of a thumb is to cool the atoms sufficiently for the effective transfer of the atom into the dipole trap.

The exact values used to perform cooling from Quantrol are shown in table 6.1.

Stage	Duration	Offset	Detuning	Cooling intensity		2D MOT	MOT coils
Units	ms	MHz	XΓ	mW/cm^2	att	ON/OFF	ON/OFF
LOADING	5000	385.25	1.62	32.8	10	ON	ON
FD MOT 1	10	391.25	3.62	23.6	11.5	OFF	ON
FD MOT 2	10	397.5	5.62	17.3	13	OFF	ON
FD MOT 3	10	403.75	7.62	12.3	14.5	OFF	ON
FD MOT 4	10	410.0	9.75	8.85	16	OFF	ON
RELAXATION	8	410.0	9.75	8.85	16	OFF	OFF
MOLASSES 1	1	410.0	9.75	5.06	19	OFF	OFF
MOLASSES 2	1	410.0	9.75	2.78	21.6	OFF	OFF
MOLASSES 3	1	410.0	9.75	2.05	22.9	OFF	OFF
MOLASSES 4	1	410.0	9.75	1.43	24.5	OFF	OFF

Table 6.1: Table showing the parameters used during the cooling procedure. FD here means far detuned as opposed to previously mentioned frequency discriminator.

CHAPTER 7

Conclusions and future work

In this thesis, I have described our first steps towards developing the quantum entanglement enhanced atom interferometer. I have outlined the major projects that were indispensable parts of the experimental apparatus. Every small project was an important milestone in building the final setup. Although we have not yet demonstrated any scientific results, we have developed the technology along the way that has a potential to be used in different fields. We developed the frequency offset locking technique that is way simpler, more robust, and more stable than the previously published methods. In addition, as the popularity of the ARTIQ system grows, we are planning to make our Quantrol system easily customizable to any Sianara based control system.

While building the experimental setup we tried to improve every component we were working on beyond the standard solutions. I believe that it will eventually pay off by providing nice results of the actual quantum entanglement enhanced atom interferometer.

Given the current state of the experimental setup, the next steps should be to improve the stability of the laser-cavity locking and optimize the atom transfer to the dipole trap. Then we should establish the state preparation that will result in a sufficient number of atoms at sufficiently low temperatures. After that we would be able to optimize the squeezing sequences following the previously demonstrated work [HEKK16], and then implementing spin dependent kicks to form a spatial interferometer. Every step in the aforementioned plan might have unexpected obstacles and require creative solutions. However, I believe that the enthusiasm and competence of the group members under the supervision of Onur will be able to reach the ambitious goal and demonstrate the first quantum entanglement enhanced atom interferometer with spacial separation of the atomic cloud.

APPENDIX A

Magnetic field compensation design

As was mentioned in the main text, each projection of the magnetic field is monitored and compensated almost independently. Position and the orientation of the magnetometer was adjusted to decrease the cross-talk between all three dimensions to the insignificant levels that does not degrade the overall stability when all three locks are engaged. Schematic drawing of the analog feedback control system for one projection is shown in figure A.1. Control system can be described in three parts: error generator, feedback loop and current driver with bias coils.

Error generator part consists of the magnetometer, and analog error signal processing. In the absence of control voltage (V_{cont}) the error signal is simply the magnetometer output scaled by voltage divider

$$V_{\text{err}} = \frac{5V_{\text{mag}}}{6}$$

Since feedback loop tries to zero the error signal the set point is zero magnetic field at the position of magnetometer. By applying control voltage we can shift the error signal to be

$$V_{\text{err}} = \frac{5V_{\text{mag}}}{6} - \frac{V_{\text{cont}}}{11}$$

The feedback loop and current driver frequency responses were carefully tailored by introducing multiple zeros and poles to maximize the bandwidth. Resulting lock bandwidth is around $2\,$kHz and has a single pole integrator.

Since bias coils had slightly different geometries the closed loop gains of each control system was also different. In addition to the geometry differences, magnetic field generated by the bottom coil was enhanced due to metallic composite of the optical table it was resting on. In order to avoid designing schemes with different parameters for each control system we implemented variable gain that can be tuned by a trimpot. It allowed us to have the same design and compensate the closed loop gain differences by adjusting the trimpot while observing its frequency response. The frequency response of one of the stabilization systems is shown in figure A.2.

The current driver has two power opamps OPA549 that are used to drive the coils. The estimated current to move the atomic cloud is $2\,$A. Therefore, the design required careful

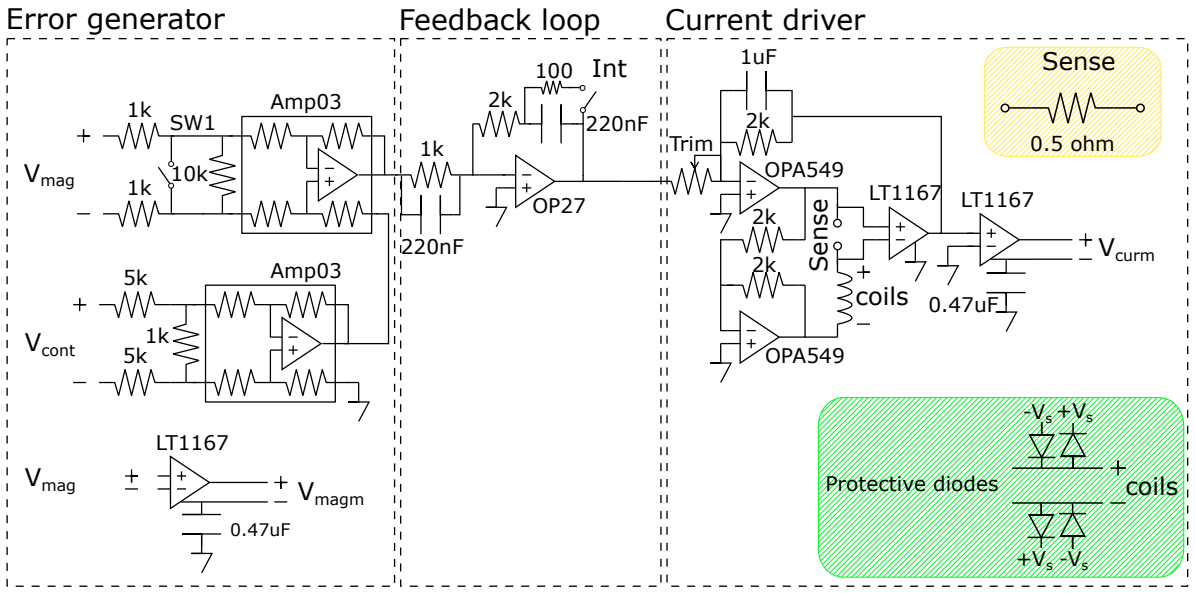

Figure A.1: Schematic drawing of analog magnetic field compensation system. V_{mag} is the magnetometer output voltage. V_{cont} is an external analog signal that can shift the set point from zero magnetic field. V_{magm} is a monitor for magnetometer output voltage. SW1 and Int are mechanical switches that connects/shorts the input from magnetometer and enables/disables integration of the feedback circuit respectively. Trim is a mechanical trimpot that is used to tune the closed loop gain. The set value of the trimpot is around $1\,\text{k}\Omega$. V_{curm} is a monitor for current driven through bias coils. Light yellow rectangle shows the sense resistor used to indirectly infer the current flowing through the MOT coils. Light green rectangle is showing the protective diodes connection to prevent the circuit from the flyback voltage.

consideration of current carrying track widths and sufficiently large capacity of the heat sink. Otherwise, there would have been a risk of burning the traces or overheating of the power op-amps that would result in instabilities.

When the inductive coils current is turned off there is a risk of fly back voltage. In order to protect the analog feedback circuitry from those voltages we implemented protective diodes that are reverse biased with ± 12 V.

Normal operation of the control system is observed from the magnetometer and current monitor outputs (V_{magm} and V_{curm}) on oscilloscope. Both monitors are buffered to avoid back action from the oscilloscope to the feedback. Current monitor was achieved by measuring the potential drop over 1 ohm current-sense resistor.

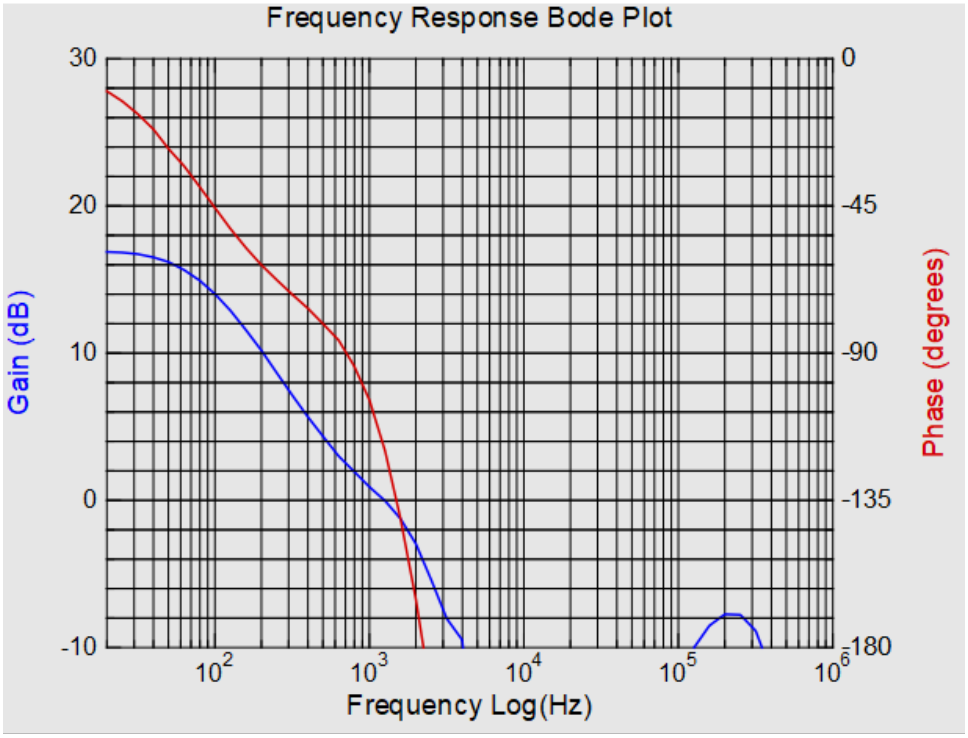

Figure A.2: Closed loop frequency response of a single projection of the magnetic field compensation control system.

Bibliography

[ACGT72] F. T. Arecchi, Eric Courtens, Robert Gilmore, and Harry Thomas. Atomic coherent states in quantum optics. *Phys. Rev. A*, 6:2211–2237, Dec 1972.

[AIF+20] F. Anders, A. Idel, P. Feldmann, D. Bondarenko, S. Loriani, K. Lange, J. Peise, M. Gersemann, B. Meyer, S. Abend, N. Gaaloul, C. Schubert, D. Schlippert, L. Santos, E. Rasel, and C. Klempt. Momentum entanglement for atom interferometry, 2020.

[AM08] Karl Johan Astrom and Richard M. Murray. *Feedback Systems: An Introduction for Scientists and Engineers*. Princeton University Press, 2008.

[AR97] C.S. Adams and E. Riis. Laser cooling and trapping of neutral atoms. *Progress in Quantum Electronics*, 21(1):1–79, 1997.

[BDB+00] F. B. J. Buchkremer, R. Dumke, Ch. Buggle, G. Birkl, and W. Ertmer. Low-cost setup for generation of 3 GHz frequency difference phase-locked laser light. *Review of Scientific Instruments*, 71(9):3306–3308, sep 2000.

[BHW+07] S. C. Bell, D. M. Heywood, J. D. White, J. D. Close, and R. E. Scholten. Laser frequency offset locking using electromagnetically induced transparency. *Applied Physics Letters*, 90(17):171120, apr 2007.

[BSD+19] J. H. Bodey, R. Stockill, E. V. Denning, D. A. Gangloff, G. Éthier-Majcher, D. M. Jackson, E. Clarke, M. Hugues, C. Le Gall, and M. Atatüre. Optical spin locking of a solid-state qubit. *npj Quantum Information*, 5(1):95, dec 2019.

[CCL+17] Wang-Yau Cheng, Ting-Ju Chen, Chia-Wei Lin, Bo-Wei Chen, Ya-Po Yang, and Hung Yi Hsu. Robust sub-millihertz-level offset locking for transferring optical frequency accuracy and for atomic two-photon spectroscopy. *Optics Express*, 25(3):2752, feb 2017.

[CdAF+05] L. Cacciapuoti, M. de Angelis, M. Fattori, G. Lamporesi, T. Petelski, M. Prevedelli, J. Stuhler, and G. M. Tino. Analog+digital phase and frequency detector for phase locking of diode lasers. *Review of Scientific Instruments*, 76(5):053111, may 2005.

[dB25] L. de Broglie. Recherches sur la theorie des quanta. *Annales de Physique*, 1925.

[DDK+20] Armin Danner, Bülent Demirel, Wenzel Kersten, Hartmut Lemmel, Richard Wagner, Stephan Sponar, and Yuji Hasegawa. Spin-rotation coupling observed in neutron interferometry. *npj Quantum Information*, 6(1):23, Feb 2020.

[DGB92] Timothy Day, E.K. Gustafson, and R.L. Byer. Sub-hertz relative frequency stabilization of two-diode laser-pumped Nd:YAG lasers locked to a Fabry-Perot interferometer. *IEEE Journal of Quantum Electronics*, 28(4):1106–1117, apr 1992.

[FIM05] Michael Fleischhauer, Atac Imamoglu, and Jonathan P. Marangos. Electromagnetically induced transparency: Optics in coherent media. *Reviews of Modern Physics*, 77(2):633–673, jul 2005.

[GAS+10] Naceur Gaaloul, H. Ahlers, T. A. Schulze, Y. Singh, S. T. Seidel, W. Herr, W. Ertmer, and E. Rasel. Quantum tests of the equivalence principle with atom interferometry. *Acta Astronautica*, 67(9):1059–1062, Nov 2010.

[GBK97] T. L. Gustavson, P. Bouyer, and M. A. Kasevich. Precision rotation measurements with an atom interferometer gyroscope. *Phys. Rev. Lett.*, 78:2046–2049, Mar 1997.

[GLWea22] Graham P Greve, Chengyi Luo, Baochen Wu, and et al. Entanglement-enhanced matter-wave interferometry in a high-finesse cavity. *Nature*, 610(7932):472–477, 2022.

[GMS+11] R. Geiger, V. Ménoret, G. Stern, N. Zahzam, P. Cheinet, B. Battelier, A. Villing, F. Moron, M. Lours, Y. Bidel, A. Bresson, A. Landragin, and P. Bouyer. Detecting inertial effects with airborne matter-wave interferometry. *Nature Communications*, 2(1):474, Sep 2011.

[HEKK16] Onur Hosten, Nils J. Engelsen, Rajiv Krishnakumar, and Mark A. Kasevich. Measurement noise 100 times lower than the quantum-projection limit using entangled atoms. *Nature*, 529(7587):505–508, Jan 2016.

[HF08] Joshua Hughes and Chad Fertig. A widely tunable laser frequency offset lock with digital counting. *Review of Scientific Instruments*, 79(10):103104, oct 2008.

[HIS+18] Yusuke Hisai, Kohei Ikeda, Haruki Sakagami, Tomoyuki Horikiri, Takumi Kobayashi, Kazumichi Yoshii, and Feng-Lei Hong. Evaluation of laser frequency offset locking using an electrical delay line. *Applied Optics*, 57(20):5628, jul 2018.

[HJH+15] P. Hamilton, M. Jaffe, P. Haslinger, Q. Simmons, H. Müller, and J. Khoury. Atom-interferometry constraints on dark energy. *Science*, 349(6250):849–851, 2015.

[Hru18] Ludwig Hruza. Temperature measurement of 24mg atoms in a mot using time of flight measurement. June 2018.

[HUH+03] Lucia Hackermüller, Stefan Uttenthaler, Klaus Hornberger, Elisabeth Reiger, Björn Brezger, Anton Zeilinger, and Markus Arndt. Wave nature of biomolecules and fluorofullerenes. *Phys. Rev. Lett.*, 91:090408, Aug 2003.

[HUV+17] Jiazhong Hu, Alban Urvoy, Zachary Vendeiro, Valentin Crépel, Wenlan Chen, and Vladan Vuletić. Creation of a Bose-condensed gas of 87 Rb by laser cooling. *Science*, 358(6366):1078–1080, nov 2017.

[JHCK10] D. M. S. Johnson, J. M. Hogan, S.-w. Chiow, and M. A. Kasevich. Broadband optical serrodyne frequency shifting. *Optics Letters*, 35(5):745, mar 2010.

[JXH+18] Matt Jaffe, Victoria Xu, Philipp Haslinger, Holger Müller, and Paul Hamilton. Efficient adiabatic spin-dependent kicks in an atom interferometer. *Phys. Rev. Lett.*, 121:040402, Jul 2018.

[KC91] Mark Kasevich and Steven Chu. Atomic interferometry using stimulated Raman transitions. *Physical Review Letters*, 67(2):181–184, jul 1991.

[KU93] Masahiro Kitagawa and Masahito Ueda. Squeezed spin states. *Phys. Rev. A*, 47:5138–5143, Jun 1993.

[LBY+15] Andrew D. Ludlow, Martin M. Boyd, Jun Ye, E. Peik, and P. O. Schmidt. Optical atomic clocks. *Reviews of Modern Physics*, 87(2):637–701, jun 2015.

[LDH22] Vyacheslav Li, Fritz Diorico, and Onur Hosten. Laser frequency-offset locking at 10-hz-level instability using hybrid electronic filters. *Phys. Rev. Appl.*, 17:054031, May 2022.

[Li80] Ming Chiang Li. Electron interference. volume 53 of *Advances in Electronics and Electron Physics*, pages 269 – 306. Academic Press, 1980.

[Man02] Ron Mancini. *Op Amps for Everyone: Design Reference*. Texas Instruments Incorporated, 2002.

[MKC08] Daniel Mccarron, S. King, and Simon Cornish. Modulation transfer spectroscopy in atomic rubidium. *Measurement Science and Technology*, 19, 05 2008.

[ML24] M-Labs. *ARTIQ Documentation*, 2024.

[MLW+23] Umang Mishra, Vyacheslav Li, Sebastian Wald, Sofia Agafonova, Fritz Diorico, and Onur Hosten. Monitoring and active stabilization of laser injection locking using beam ellipticity. *Opt. Lett.*, 48(15):3973–3976, Aug 2023.

[MvdS99] Harold J. Metcalf and Peter van der Straten. *Laser Cooling and Trapping*. Springer New York, New York, NY, 1999.

[MWMRK22] Benjamin K. Malia, Yunfan Wu, Julián Martínez-Rincón, and Mark A. Kasevich. Distributed quantum sensing with mode-entangled spin-squeezed atomic states. *Nature*, 612(7941):661–665, November 2022.

[NAZ+14] Daniele Nicolodi, Bérengère Argence, Wei Zhang, Rodolphe Le Targat, Giorgio Santarelli, and Yann Le Coq. Spectral purity transfer between optical wavelengths at the 10^{-18} level. *Nature Photonics*, 8(3):219–223, mar 2014.

[NHOW06] K. Nakayama, M. Hyodo, R. Ohmukai, and M. Watanabe. Multiple frequency stabilization of lasers using double saturation spectroscopy. *Optics Communications*, 259(1):242–250, mar 2006.

[PCC03] A Peters, KY Chung, and Steven Chu. High-precision gravity measurements using atom-interferometry. *Metrologia*, 38:25, 03 2003.

[Pue12] G. Puentes. Laser frequency offset locking scheme for high-field imaging of cold atoms. *Applied Physics B*, 107(1):11–16, apr 2012.

[RCGW04] G. Ritt, G. Cennini, C. Geckeler, and M. Weitz. Laser frequency offset locking using a side of filter technique. *Applied Physics B*, 79(3):363–365, aug 2004.

[RSC+14] G. Rosi, F. Sorrentino, L. Cacciapuoti, M. Prevedelli, and G. M. Tino. Precision measurement of the newtonian gravitational constant using cold atoms. *Nature*, 510(7506):518–521, Jun 2014.

[Rub06] Enrico Rubiola. Tutorial on the double balanced mixer. aug 2006.

[Sal11] Evan Ali Salim. *Ultracold matter systems and atomtronics instrumentation*. PhD thesis, University of Colorado, 2011. `https://jila.colorado.edu/sites/default/files/2019-04/salim-thesis_small.pdf`.

[SCLT94] G. Santarelli, A. Clairon, S.N. Lea, and G.M. Tino. Heterodyne optical phase-locking of extended-cavity semiconductor lasers at 9 GHz. *Optics Communications*, 104(4-6):339–344, jan 1994.

[SEG+99] U. Schünemann, H. Engler, R. Grimm, M. Weidemüller, and M. Zielonkowski. Simple scheme for tunable frequency offset locking of two lasers. *Review of Scientific Instruments*, 70(1):242–243, jan 1999.

[SES+07] N. Strauß, I. Ernsting, S. Schiller, A. Wicht, P. Huke, and R.-H. Rinkleff. A simple scheme for precise relative frequency stabilization of lasers. *Applied Physics B*, 88(1):21–28, jun 2007.

[SgoAD96] Pascal Szriftgiser, David guéry odelin, Markus Arndt, and Jean Dalibard. Atomic wave diffraction and interference using temporal slits. *Physical review letters*, 77:4–7, 08 1996.

[SHH21] Stuart S. Szigeti, Onur Hosten, and Simon A. Haine. Improving cold-atom sensors with quantum entanglement: Prospects and challenges. *Applied Physics Letters*, 118(14):140501, apr 2021.

[SMB+98] M. J. Snadden, J. M. McGuirk, P. Bouyer, K. G. Haritos, and M. A. Kasevich. Measurement of the earth's gravity gradient with an atom interferometer-based gravity gradiometer. *Phys. Rev. Lett.*, 81:971–974, Aug 1998.

[SSLVac10] Monika H. Schleier-Smith, Ian D. Leroux, and Vladan Vuletić. Squeezing the collective spin of a dilute atomic ensemble by cavity feedback. *Phys. Rev. A*, 81:021804, Feb 2010.

[Ste03] Daniel Steck. Rubidium 87 d line data. 01 2003.

[STN+06] Charles Santori, Philippe Tamarat, Philipp Neumann, Jörg Wrachtrup, David Fattal, Raymond G. Beausoleil, James Rabeau, Paolo Olivero, Andrew D. Greentree, Steven Prawer, Fedor Jelezko, and Philip Hemmer. Coherent Population Trapping of Single Spins in Diamond under Optical Excitation. *Physical Review Letters*, 97(24):247401, dec 2006.

[TK14] Guglielmo M Tino and Mark A Kasevich. *Atom Interferometry*, volume 188. IOS Press, 2014.

[UHH02] Th Udem, R. Holzwarth, and T. W. Hänsch. Optical frequency metrology. *Nature*, 416(6877):233–237, mar 2002.

[WPM+19] Xuejian Wu, Zachary Pagel, Bola S. Malek, Timothy H. Nguyen, Fei Zi, Daniel S. Scheirer, and Holger Müller. Gravity surveys using a mobile atom interferometer. *Science Advances*, 5(9), 2019.